PRECISELY CONTROLLED SYNTHESIS OF REDUCED GRAPHENE OXIDE SUPPORTED ELECTROCATALYSTS FOR PEM FUEL CELLS BY PULSED PHOTOCATALYTIC DEPOSITION

by
NAVID HAGHMORADI

Submitted to the Graduate School of Engineering and Natural Sciences
in partial fulfillment of
the requirements for the degree of
Doctor of Philosophy

Sabanci University
December 2021

PRECISELY CONTROLLED SYNTHESIS OF REDUCED GRAPHENE OXIDE SUPPORTED ELECTROCATALYSTS FOR PEM FUEL CELLS BY PULSED PHOTOCATALYTIC DEPOSITION

APPROVED BY:

DATE OF APPROVAL:17.12.2021

Precisely controlled synthesis of reduced graphene oxide supported electrocatalysts for PEM fuel cells by pulsed photocatalytic deposition

Navid Haghmoradi

Ph.D. Dissertation, December 2021

Supervisor: Prof. Dr. Selmiye Alkan Gürsel

Co-advisor: Dr. Begüm Yarar Kaplan

ABSTRACT

Keywords: PEM fuel cell, partially reduced graphene oxide, photocatalyst, pulsed UV, density functional theory, neural network modelling

It has almost been a decade that scientists have been trying to address the shortcomings of batteries and polymer electrolyte membrane (PEM) fuel cells in production cost. One of the most important parts of the PEM fuel cells is its catalyst layer, CL. The CL of PEM fuel cells consists of Pt-based particles deposited on a carbon support. Although carbon black (CB)/Pt shows a promising electrochemical performance for hydrogen oxidation reaction (HOR) and oxygen reduction reaction (ORR), its vulnerability to the PEM fuel cells' harsh environment has made this carbon-based electrocatalysts very sensitive to corrosion, and performance loss. One of the promising candidates to replace carbon black in CL preparation seemed to be graphene-based support. This study demonstrated the capability of a novel method in controlling the structural and electrochemical properties of electrocatalysts deposited on graphene-based supports, utilizing a pulsed-UV setup for the synthesis procedure. In the second chapter, the variation of UV_{on} and UV_{off} periods resulted in samples with a range of different structures, compositions, and activities. The results revealed a dominant growth and agglomeration phase of Pt particles, mostly with metallic states, by increasing both UV_{on} and U_{off} time spontaneously. Further chemical reduction by highly concentrated ascorbic acid was used to confirm proposed mechanisms, which lead to samples even with more metallic Pt (Pt^0) and higher electrochemical activities. The rest of the second chapter focused on utilizing a series of transition metal ions, Co^{2+}, Ni^{2+} or Fe^{2+}, to assist the deposition of Pt on PRGO planes that resulted in various types of Pt particles size, morphologies and distribution. Different interactions between hole scavengers and PRGO particles or water molecules, was the main parameter that modulated the Pt^{4+} reduction. The structural and electrochemical properties of electrocatalysts revealed that utilizing the cobalt-based hole scavenger, caused a dominant growth phase of Pt particles at preferred positions, with improved electrocatalytic activities (ECSA value of 195.91 $m^2.g^{-1}$ for Co^{2+} vs. 152.01 $m^2.g^{-1}$ for methanol). The third chapter includes the computational methods in evaluating the properties of the samples by modelling either the cyclic voltammetry data with a neural network algorithm or DFT calculation of H_2 adsorption on graphene-based electrocatalysts. The result of the neural network modelling demonstrated the potential of the proposed method in designing a highly controllable synthesis procedure by which the electrochemical properties of the electrocatalysts could be predictable before the synthesis. The DFT calculation by the Quantum-Espresso code revealed that the existence of oxygen functional groups on graphene plane not only affects the crystal structure of deposited Pt particles, but also hinders the adsorption of H_2 molecules on Pt surface.

PEM yakıt pilleri için grafen oksit destekli elektrokatalizörlerin atımlı fotokatalitik biriktirme ile kontrollü sentezi

Navid Haghmoradi
Doktora Tezi, Aralık 2021

Tez Danışmanı: Prof. Dr. Selmiye Alkan Gürsel
Tez Eş Danışmanı: Dr. Begüm Yarar Kaplan

ÖZET

Anahtar kelimeler: PEM yakıt pili, kısmen indirgenmiş grafen oksit, fotokatalizör, atımlı UV, yoğunluk fonksiyonel teoremi, nöral ağ modelleme

Son on yılda, bilim adamları özellikle bataryalar ve polimer elektrolit membran (PEM) yakıt pillerinin yüksek üretim maliyetini düşürme konusunda çalışmaktadır. PEM yakıt pillerinin en önemli bileşenlerinden biri katalizör tabakasıdır (CL). PEM yakıt pillerinde CL, karbon destek malzeme üzerinde Pt esaslı parçacıkları içermektedir. Karbon siyahı (CB)/Pt, hidrojen yükseltgenme reaksiyonu (HOR) ve oksijen indirgeme reaksiyonu (ORR) için umut verici bir elektrokimyasal performans gösterse de, PEM yakıt pillerinin zorlu çalışma ortamında bu karbon bazlı elektrokatalizörler korozyona eğilim göstermektedir ve bu da performans kaybına sebep olmaktadır. CL hazırlamada karbon siyahının yerini alacak umut vadeden alternatiflerden biri, grafen esaslı desteklerdir. Bu tez çalışmasının ilk bölümünde, grafen esaslı destekler üzerinde biriken Pt elektrokatalizörlerin sentezi için atımlı UV düzeneği kullanılmıştır ve elelektrokimyasal özelliklerini kontrol etmede yeni bir yaklaşım sunulmuştur. İkinci kısımda, UV_{on} ve UV_{off} periyotlarının değişimi ile bir dizi farklı yapı, bileşim ve aktiviteye sahip elektrokatalizörler elde edilmiştir. Sonuçlar, çoğunlukla metalik halde olan Pt parçacıklarının baskın bir büyüme ve çökme fazının hem UV_{on} hem de UV_{off} zamanının artırılarak elde edilebileceğini ortaya çıkarmıştır. Ek olarak elde edilen elektrokatalizörler yüksek derişimli askorbik asit ile indirgenerek daha fazla metalik Pt (Pt^0) ve daha yüksek elektrokimyasal aktivitelere sahip katalizörler elde edilerek önerilen mekanizmalar doğrulanmaya çalışılmıştır. İkinci bölümün geri kalanında, çeşitli tipte Pt partikül boyutu, morfolojisi ve dağılımı ile sonuçlanan kısmen indirgenmiş grafen oksit (PRGO) üzerinde Pt birikmesine yardımcı olmak için bir dizi geçiş metal iyonu, Co^{+2}, Ni^{+2} veya Fe^{+2} kullanımına odaklanılmıştır. Delik süpürücüler ile PRGO parçacıkları veya su molekülleri arasındaki farklı etkileşimler, Pt^{+4} indirgenmesine etki eden ana parametredir. Elektrokatalizörlerin yapısal ve elektrokimyasal özellikleri incelendiğinde kobalt esaslı delik süpürücünün kullanılması ile tercih edilen pozisyonlarda Pt büyüme fazının baskın olduğu ve böylelikle daha iyi elektrokimyasal aktivite elde edilidiği görülmüştür (ECSA değeri Co^{+2} için 195.91 $m^2.g^{-1}$, metanol için 152.01 $m^2\ g^{-1}$). Üçüncü bölüm, hazırlanan elektrokatalizörlerin özelliklerinin değerlendirilmesi için hesaplamalı yöntemlerden; sinir ağı algoritması ile döngüsel voltametri verileri ya da grafen esaslı elektrokatalizörlerde H_2 adsorpsiyonunun DFT hesaplaması modellemesi kullanılmıştır. Sinir ağı modellemesi sonuçları önerilen oldukça kontrol edilebilir bir yöntem ile sentezlenen elektrokatalizörlerin elektrokimyasal özelliklerinin sentezden önce tahmin edilebilirliğini göstermiştir. Quantum-Espresso kodlaması ile yapılan DFT hesaplaması, grafen düzleminde oksijen fonksiyonel gruplarının varlığının yalnızca biriken Pt parçacıklarının kristal yapısını etkilemediğini, aynı zamanda Pt yüzeyinde H_2 moleküllerinin adsorpsiyonunu da engellediğini ortaya koymuştur.

To my lovely wife:
my success means nothing without you in my life.

ACKNOWLEDGEMENT

Foremost, I would like to express my deep gratitude to my supervisor, Prof. Dr. Selmiye Alkan Gürsel, for her continuous support, enthusiasm and encouragement throughout my Ph.D. education. I extend my gratefulness to my co-advisor, Dr. Begüm Yarar Kaplan, and Assoc. Prof. Alp Yürüm for their guidance and constructive criticism at any time of my research. I would like to thank my committee members, Prof. Dr. Burç Mısırlıoğlu, Prof. Dr. Alimet Sema Özen, Dr. Öğr. Üyesi Burcu Dedeoğlu for their valuable time, interest, and constructive suggestions.

I must thank the faculty members of department of Materials Science and Nanoengineering for their valuable and educative lectures throughout my Ph.D. which helps me shape my profession in materials science.

In addition, my sincere thanks go to Dr. Adnan Tasdemir, Dr. Buse Bulut Köpüklü, Dr. Aysu Yurduşen Öztürk and Dr. Mohammed Zabara.

I am also grateful to my colleagues and collaborators Zahide Tuğba Sarı, Dr. Sina Abdolhosseinzadeh, Naeimeh Rajabalizadeh, Vahid Charkhesht, Esaam Jamil, Ahmet Can Kırlıoğlu, Emre Burak Boz, Bilal Sayyed Said Iskandarani, Mohammad Alinezhadfar, Emre Utku Ötürk, Siddharta Peri, Hamed Salimkhani, Golnaz Nasari, Mirsajjad Mousavi for making laboratory work productive, efficient and also enjoyable. I am very happy that I have been a member of SU-ESC research group.

My wife earns the most special thanks for her endless support during my Ph.D. life. Graduate life could be a mental disaster if one does not have a unique support in their life. Pegah has been playing the most critical and important role, especially, during my Ph.D. study. She was always there when I was desperate in everything. I hope I have been supporting her in her difficult and challenging academic life too. Thank you, my love, my life.

I will never forget the joyful memories from my friends: Arash Ebrahimi, Naeimeh rajabalizadeh, Meysam Rafiei, Mahsa Nourani, Faraz Tehranizadeh, Nasim Barzegar, Ali Asgharpour, Ali Barzegar, Amin Ahmadi, Sirous Khabbaz, Mehri Ahmadian, Ali Azizi, Araz Sheibani, Sina Rastani, Deniz Mortazavi, Ehsan Khoshniat, Negar Farhadi, Pozhhan Mokhtari, Zoher Aliabadi, Mohammad Dabbagh, Kaveh Rahimzadeh, Amin Bagherzadeh, Yasaman Karimian, Saeedeh Ahmadi, Madine Rastgoo, Sara Barakat, Elif Çelik, Cevriye Pamukçu, Ertunga Eyupoğlu, Ayhan Parlar, Didem Özkazan, Mert kaya Aras, Başak Ozata, Asal Ghaffari and Lolai Ikromzodah. I am grateful to them for all joyful memories they made for me.

Last but not least, I would like to thank my family and all their support they gave me. My parents, lovely sister, and kind brother. Getting old knowing there are lovely people out there who are always hope your success gives you an endless motivation.

I would like to show my appreciation for all the support received from Sabanci University Nanotechnology Research and Application Center (SUNUM) and Faculty of Engineering and Natural Science in Sabanci University, especially the NS team.

The numerical calculations reported in this paper were partially performed at TUBITAK ULAKBIM, High Performance and Grid Computing Center (TRUBA resources).

ABBREVIATIONS

ANN	Artificial Neural Network
CB	Carbon Black
CNT	Carbon Nanotube
CV	Cyclic Voltammograms
DFT	Density Functional Theory
EV	Electric Vehicles
FESEM	Field Emission Scanning Electron Microscopy
GO	Graphene Oxide
HS	Hole Scavenger
PRGO	Partially Reduced Graphene Oxide
ORR	Oxygen Reduction Reaction
PV	Photovoltaic
rGO	reduced GO
TEM	Transmission Electron Spectroscopy
UV	Ultraviolet
XPS	X-Ray Photoelectron Spectrometer
XRD	X-Ray Diffraction

TABLE OF CONTENT

LIST OF FIGURES

LIST OF TABLES

CHAPTER 1. INTRODUCTION

1.1. The motivations of this thesis

The main goal this dissertation is to develop electrocatalyst materials for polymer electrolyte fuel cells (PEMFCs). With the help the handmade setup, we could manipulate the structural and electrochemical performance of Pt particles on graphene-based supports. The setup design provided a series of pulsed-UV illumination such as UV-on and UV-off duration based on which the morphology, composition and finally the performance of the Pt/graphene electrocatalyst (Chapter 3). The behavior of transition metal ions, Co^{2+}, Ni^{2+} and Fe^{2+}, in a graphene oxide containing solution was the main parameters based on which we could even increase the performance of the previously best electrocatalysts. In the chapter 3 we concluded that the highest UV-on and UV-off could result in samples with more metallic Pt and better performance. In Chapter 4, we used one of the mentioned three transition metal ions as an additive to assist the deposition of Pt on favorable spots to increase the final product electrochemical performance. The result shows that the oxidation of Co^{2+} could act as the hole scavenging process (in the absence of methanol as the previous procedure hole scavenger) and facilitate the deposition of highly active Pt. The 5th chapter focuses on the computational modelling of the photocatalytically prepared Pt/rGO with machine learning method (artificial neural network, ANN, algorithm) and density functional theory, DFT, calculation (using the Quantum-Espresso code). The result of the ANN modelling demonstrated the high potential of the proposed synthesized method in highly controlling the properties of the final product. The algorithm performed well in predicting the cyclic voltammetry outputs of unknow samples, with being trained by know samples. The DFT calculation were used to demonstrate the effect of oxygen functional group on the structural change of graphene layers, the equilibrium shape of Pt crystal on graphene or graphene oxide layer and the adsorption of H_2 ions on the Pt surface.

1.2. Polymer electrolyte fuel cells, PEMFCs, and their challenges

High surge for the demand of advanced and developed energy storage systems or conversion facilities such as batteries and fuel cells have resulted from the fundamental environmental issues such as fossil fuel crisis, population growth, and finding more

sustainable energy resources. Among the existing fuel cell technologies, polymer electrolyte fuel cells also known as proton exchange membrane fuel cells (PEMFCs) are quite promising, but its commercialization is hindered because of hydrogen/oxygen-to-electricity conversion alongside the usage of narrow range of expensive metals i.e. Pt or Pt alloys, as catalysts.

In a PEMFC, the electrochemical reactions, oxidation or reduction of the hydrogen or oxygen gases, take place on the anode or cathode, respectively. The oxygen reduction reaction (ORR) in PEMFCs is based on the Equation 1. The sluggish kinetics of the ORR and its high overpotential necessitates the usage of high loading of expensive Pt-based catalysts, a bottleneck to commercialization targets [1]. Different research works have been conducted to find alternative catalyst materials or to decrease the amount of platinum loading. Some success stories have proven the high energy efficiency and power density of PEMFCs and its high applicability potential in an electric vehicle production [2][3][4][5][6].

$$2O + 4H + + 4e - \rightarrow H_2O \qquad 1.1$$

These oxidation and reduction reactions contain a series of charge and mass transfer in a humid environment at an elevated temperature. Therefore, employing a conductive and corrosion resistant support with a high surface area is desirable [7][8][9]. Carbon black, in this regard, is generally considered as an accepted support material [10][11]. However, its low corrosion resistance is a major hindrance in the fuel cells' long-term performance. The mechanism of the carbon corrosion at thermodynamically low potential is shown in equation 2 [12].

$$C + 2H_2O \rightarrow CO_2 + 4H^+ + 4e^- \quad E^o = 0.207 \text{ V/SHE} \qquad 1.2$$

To further enhance the electrocatalytic activity and stability of carbon based-support/Pt composites, it is crucial to increase the interaction between the matrix (support) and the dispersive phase (Pt) [13][14]. Yet, the vulnerability of carbon black to harsh environments increases the chance of detachment and agglomeration of platinum as a result of corrosion [15][12]. Consequently, utilizing an alternative support to carbon black is desirable, a support material which would be highly stable and conductive [16][17].

1.3. Graphene: as a catalyst support

Graphene refers to a flat single atomic layer of carbon atoms bonded to each other through covalent bonds [18]. During the last decade the application of graphene, with its sp^2 C-C bond structure, has been the subject of many research activities. There are various protocols and synthesis methods through which the final product benefits from graphene or graphene-based derivatives' mechanical, electrical, thermal, chemical or optical properties [19][20]. For example, developing electric circuits [21], water purification and filtration [22], sensing [23], photovoltaic [24], and especially with regards to this research work, energy storage and conversion [25][26] are among some application domains of graphene.

To produce graphene from the commercially available graphite sources, exfoliating the graphite into the graphene layers through oxidation process has been developed. The most efficient and high-yield technique for graphene production is the modified-Hummer method [27][28] which is based on the earlier Hummer method [29]. This method includes the oxidation of graphite particles causing the formation of defects and oxygen functional groups over the edges and the basal planes of graphene layers and further exfoliating this graphite oxide results in separated graphene oxide (GO) layers (Figure 1). The oxidation process is a diffusion-controlled process [30] and the resultant GO is electrically an insulator [31].

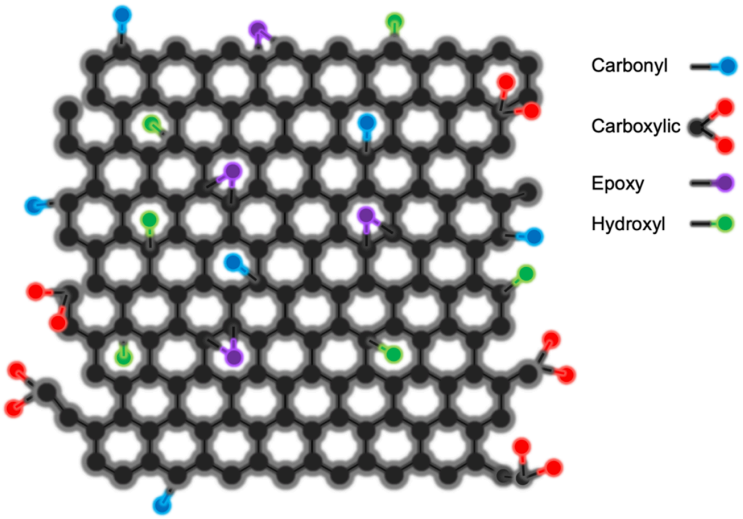

Figure 1.1. Graphene oxide layers and its functional groups

Dreyer et al. studied the effect of oxygen functional groups and their type on the electronic structure of the graphene and its conductivity [32]. Four different oxygen functional groups exist on the graphene oxide plane: epoxy and hydroxyl formed on the basal plane; and carboxyl and carbonyl formed on the edges. The functional groups disrupt the sp^2 base and establish sp^3 zones [32]. It is the mixture of sp^2 and sp^3 hybridizations responsible for graphene oxide's heterogenous electrical properties [27]. Electrochemical characterization of graphene-based materials such as electrochemical impedance spectroscopy and cyclic voltammetry revealed that in graphene oxide with different levels of oxygen functional groups i.e. C/O ratio, the charge transfer to the electrolyte was more difficult when the amount of oxygen increased [33]. It is important to note that using different oxidizing agents leads to different ratio of the four functional groups, and hence variance in GO structure observed [33].

In a study conducted by Jeong et al. [34], the authors studied the increasing trend of GO's band gap with increasing the oxidation level. The band gap of graphene oxide was reported to be in the range of 1.7 to 4.3 eV, which covered the energy range of the visible light i.e. 1.9-2.6 eV. Different methods have been reported to tune the band gap of GO including step wise reduction of GO with gas-base hydrazine at room temperature [35], [19], hydrazine monohydrate [36] and sodium borohydride [37]. Considering toxic and difficult-to-handle chemicals in these methods, one would prefer to use more environmentally friendly chemicals such as glucose, fructose, sucrose [38] and ascorbic acid [35],[39],[19]. In two of our recent studies, we investigated the effect of highly concentrated sodium hydroxide on the band gap modulation of graphene oxide [40] [41]. In the last decade, due to the tunable electronic band gap structure, the application of GO in photocatalytic applications [42][28] or as an electron acceptor in solar cells have been proposed [27].

The utilization of graphene layer as a new generation of a matrix for catalyst materials has opened up a new avenue in catalyst materials development [2,4,17,40,41]. But, there are two major challenges that hinder the application of graphene in catalyst production: a solution processable graphene layer; and stable catalyst particles attached on the graphene layer [43].

1.4. Nucleation and growth of particles

To better understand the Pt particles formation and growth and discuss the effect of different parameters on the electrocatalytic activity of the support/catalyst particles, a brief review of the nucleation and growth of particles from solution or liquid phase is helpful. The mechanism of nucleation and growth of particles from a liquid phase and the affecting parameters should be considered here. Two forms of particle nucleation take place, homogenous and heterogenous, respectively. The former occurs when the nuclei are uniformly formed from the main phase and the latter occurs due to inhomogeneities of the main phase [44]. In the homogenous nucleation and growth, the surface of a stable nucleus is considered to be the template for the crystal growth. However, in the heterogeneous nucleation, the surface of a second phase facilitates the nucleation and growth process. Thermodynamics of homogenous nuclei formation considers the total free energy of the particle as a summation of the surface free energy and the bulk free energy (Equation 3) [45],[44].

$$\Delta G = 4\pi r^2\gamma + 4/3\ \pi r^3\ \Delta G_v \qquad 1.3$$

Here, r is the spherical radius, γ is the surface energy and ΔGv is the bulk free energy. The surface free energy is positive and is a barrier in the growth process. However, the bulk free energy is negative and favorably decreases the total free energy as the particle size increases. The bulk free energy depends on the temperature, Boltzmann constant (KB), the supersaturation of the solution and its molar volume (v) (equation 4).

$$\Delta G_v = -\frac{k_B T Ln(S)}{v} \qquad 1.4$$

Considering Equations 3 and 4, and the resultant graph (Figure 1.2) lead one to find the critical radius and free energy. When r = rc, the particle has a stable size more than which the free energy is decreases by further growth i.e. the total free energy is at its extremum value. In this study, our final goal is the nucleation and growth of platinum particles on graphene-base material. In this regard, existence of graphene sheets in a suspension is the inhomogeneity, on top of which the nucleation begins (Figure 1.3).

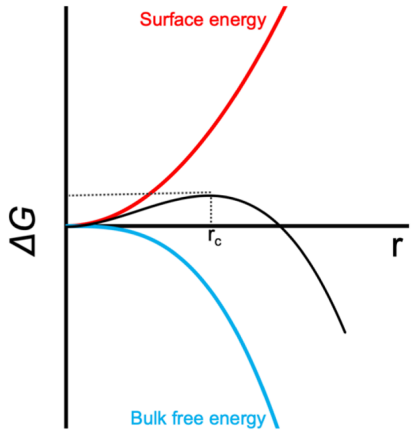

Figure 1.2. Critical radius for nucleation and growth

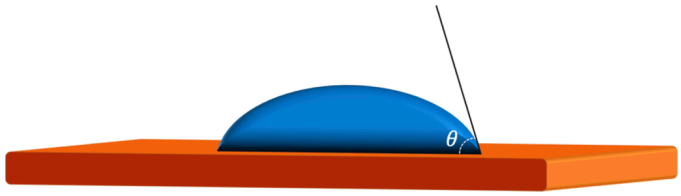

Figure 1.3. Contact angle (θ) for heterogenous nucleation.

If θ < π, the nuclei and the surface have high affinity and cause the surface term to decrease. In this case, the critical free energy is lower than the one in homogenous nucleation by the factor of ϕ (Equations 5 and 6) [44].

$$\Delta G_{vcrit}^{hetero} = \phi \Delta G_{vcrit}^{homo} \quad 1.5$$

$$\phi = \frac{(2 + cos\theta)(1 - cos\theta)^2}{4} \quad 1.6$$

1.5. Photocatalytic synthesis of metal/metal oxide nanoparticles

Electronic structure of semiconductors makes them an attractive substrate for nucleation and growth of metal/metal-oxide particles by means of photocatalytic deposition [46][47][48]. The desire to use the photon energy for catalyst materials synthesis or more directly to perform a catalytic process is because of the abundance of solar energy that may provide a cheap, continuous and reliable source of energy for chemical synthesis and

catalytic reactions [45][28]. There are various applications in which a well-chosen composite catalyst, including a semiconductor with an attached metal/metal-oxide particle, determines the efficiency and cost of the application. Composites such as Ag/TiO_2 [49][50] Pt/TiO_2 [51] and Cu/ZnO [52] are examples of metals and semiconductors being employed. Water splitting and hydrogen production [53][54], dye degradation, organic materials oxidation [51], removing water contamination [55], ozonation of pesticides [56], conversion of CO_2 to organic fuels like methanol [57][54] and bacterial disinfection [58] are examples of the applications in which the photon energy is either used for the catalyst synthesis or is used to benefit from the final application of the catalyst.

1.6. Fundamental concepts

1.6.1. Light-matter interaction

Based on the phase of the matter and its nature light can be absorbed, reflected, or transmitted. Short distance in liquid electrolyte is necessary to avoid energy loss as a result of light absorbance. Because in liquid electrolyte some portion of the light is absorbed while the rest is being transmitted. The second fact about the liquid electrolyte is the reflection on the interface. To avoid losing some wavelength by reflection one could benefits from antireflective coatings.

When the photon reached the matter, if its energy is higher than the band gap, it is going to be absorbed. This energy is causing the electron excitement. The depth by which the photon penetrates into the matter depends on the matter and the wavelength. It is defined as the depth until which 37% percent (1/e) of the photons are absorbed. For example, this depth is 2 um for Si by using a light with 555 nm wavelength [59].

1.6.2. Electron excitation

In semiconductor materials electrons form valance and conduction band indicating their level of energy, E_v and $E_{c,}$ respectively. Any energy level between these tw levels of energy (the band gap region) is forbidden for electron to have, at that semiconductor. If the photon energy is larger than the band gap, the electron will be excited to the conduction band and leave the hole in the valance band. The excess of the photon energy is given to the atoms next to the excited electron, causing vibration and temperature increase [59].

Nature of some semiconductor materials in crystal of which there is a doped element categorize them under the n- or p-type semiconductors. The dopant could be an acceptor of free electron or giver of free electron. In these cases, the dominance of the charge career (the electron when the dopant is giver and the hole when the dopant acceptor) determines the type of semiconductor. If the Fermi level is close to the valance band the main charge careers are hole the semiconductor is considered to be p-type and when the Fermi level is close to the conduction band and the major charge career is the electron, the type is n-type [59].

1.6.3. Charge scavenging (the desired process)

High recombination rate of the excited electron and the formed hole is not desirable for photocatalytic reactions. In this regard, one should efficiently separate the charge careers and use them for the redox reactions. One way is junction of the semiconductor with a second metal, electrolyte, semiconductor, or ion. In this case there would be an electric field in the interface. In this electric field, the negative and positive charge careers would be separated. This junction and immigration of charge careers (for example in p-n junction) causes the fermi level change. Figure 1.4 demonstrates the immigration of the electron to the surface and the holes deep into the bulk. Also, the charge immigration is governed by the charge mobility and concentration. The charge mobility depends on the structure and defects of the semiconductor [59].

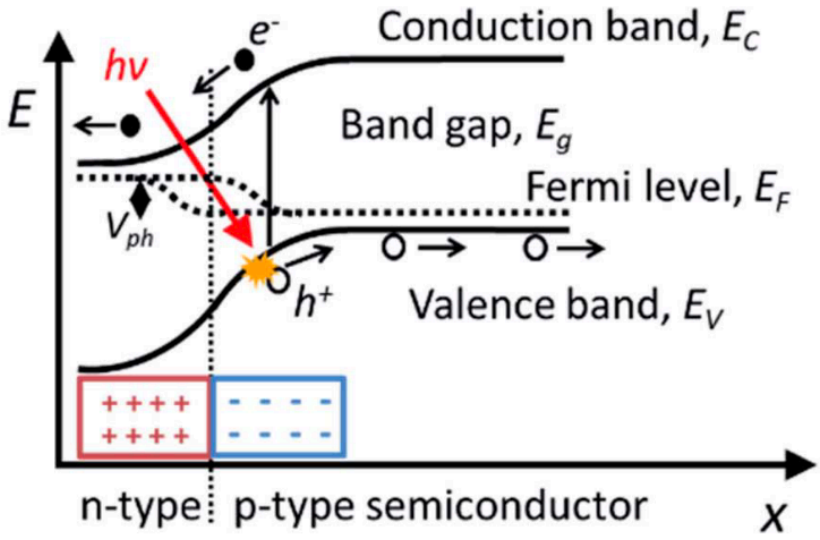

Figure 1.4. Energy diagram of p-n junction under illumination and migration of electrons and holes [59]

1.7. Semiconductor materials and relative redox potentials of metals

The mechanism of the photocatalytic deposition is illustrated in Figure 1.5 Illumination of the semiconductor by a light source with the proper wavelength and energy causes the excitation of electron from the valence band (VB) to the conduction band (CB), and separation of charge carriers (electron, e^- and holes, +). Harvesting the produced electron or hole and using them as a source to reduce or oxidize metallic ions, respectively, is the principle of the photocatalytic procedure [47][60][61]. If the redox potential of the in-contact species is more positive than the electron's potential in CB, the reduction will take place. And if the redox potential of the reaction is more negative than the hole's potential in VB, then oxidation will occur [54]. In a photocatalytic reduction, the hole in VB could be consumed to oxidize additive chemicals known as hole scavengers [61], so the CB electron would be responsible for the reduction of metal ions on the surface [28,48,52].

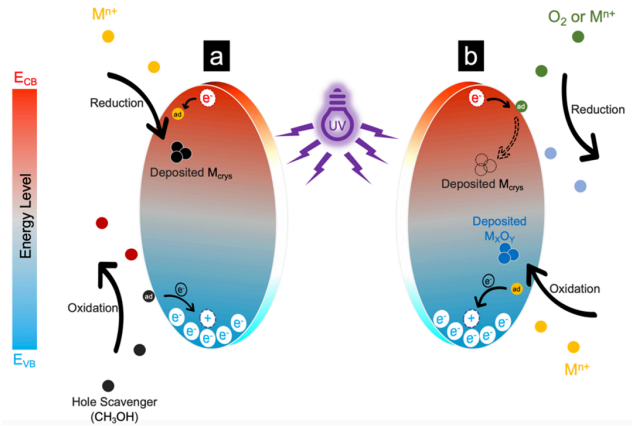

Figure 1.5. Mechanism of the photocatalytic deposition.

Based on the band structure of different semiconductor materials two general equations could represent the photoreduction and photooxidation process of metal ions.

$$M^{n+}(aq) + ne^- \rightarrow M(s) \qquad 1.7$$

$$M^{n+}(aq) + nh^+ + nH_2O \rightarrow MO_n(s) + 2nH^+ \qquad 1.8$$

As it was discussed above, the redox potential of metal species must be at a favorable position with regard to the band structure of the semiconductors. The conduction band must have much negative potential with respect to the reduction potential of metals, and the potential of the valance band must be much positive with regards to the redox potential of the species to be oxidized, that could be water oxidation, metal ions

oxidation or a hole scavenger oxidation. Figure 1.6 shows the band structure of some semiconductors and the position of the redox potential of some reactions with respect to them. Figure 1.7 is also demonstrating the redox potential of the different metal ions. To choose the proper semiconductor, these two types of figure must be considered [62].

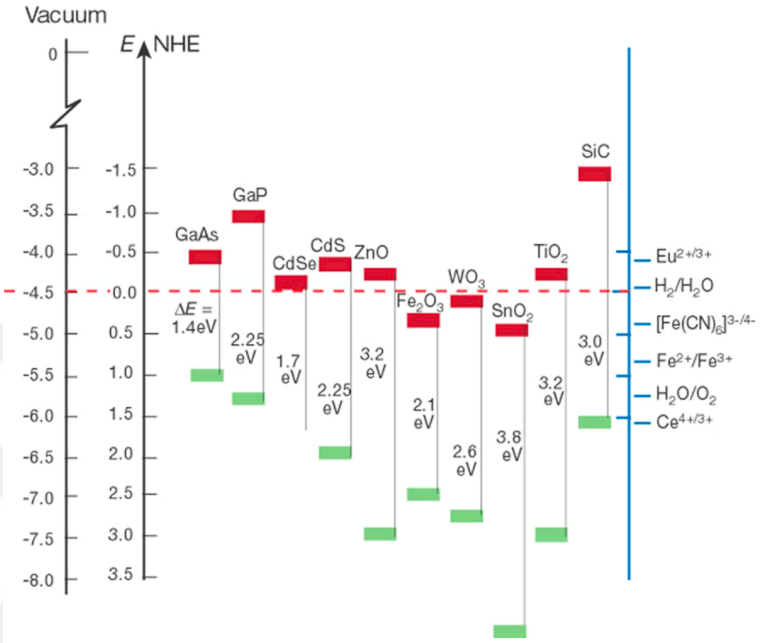

Figure 1.6. The redox potential of some semiconductor materials and the position of the redox potential of some electrochemical reactions with respect to them [62].

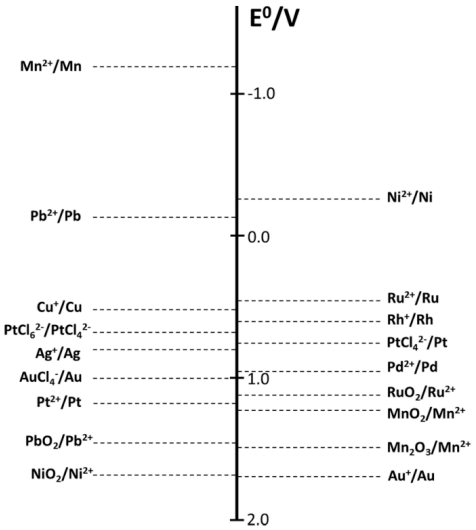

Figure 1.7. Redox potential of different metals [62]

1.8. Some semicoductros and desposited particles

Deposition of metal or metal ions on a semiconductor material could find different applications. Also, the photocatalytic reaction could be the direct application of semiconductor materials. Because of that, there must be a distinguished approach while dealing with photocatalytic reactions. In this regard, metal/metal oxide nanoparticles could develop the photocatalytic properties of the semiconductor support. The area in which the photodeposited metal(oxide) could be utilized could be solar fuel synthesis, water treatment or air purification [62].

1.8.1. Photodeposition of Pt on TiO_2 and affecting parameters

Different types of metals have been photodeposited on TiO_2 so far. Particles such as, Pt, Ag, Pd and Au are among them. Not just metal particles but also metal oxides like PbO_2 and RuO_2 and another types of semiconductors such as CdS have been deposited on TiO_2 [62]. Several different parameters could affect the deposition of metal ions on TiO_2. One of the significant parameters affecting Pt deposition on TiO_2 supports is the hole-scavenger or the sacrificial agent. It was found that higher concentration of hole-scavengers resulted in higher rate of hole filling and increased the concentration of Pt^0 with respect to other oxidation state of Pt (Pt^{2+} and Pt^{4+}). It was also suggested that the photocatalytic oxidation of methanol is an effective way to reduce Pt^{4+} into metallic Pt. Methanol could also form a radical agent that helped the reduction of Pt. However, high concentration of Methanol could increase the size of deposited Pt on TiO_2 [62].

The second parameter which could also affect the morphology and composition of Pt particles is the solution pH. In the absence of hole scavengers, neutral pH caused the deposition of $Pt(OH)_2$ but in higher pH, PtO_2 is favorable to deposit on TiO_2. At lower pH, deposition of Pt is more difficult especially when there are Cl^- ions in the systems. This trend of Pt deposition with respect to pH value (higher at higher pH and not efficient at lower pH) could be reversed when a hole scavenger is added to the system. Also, the oxidation state of Pt could be manipulated at different pH with addition of hole scavengers and changing its concentration [62].

Rather than the type of the Pt precursor and also the temperature, the third parameter is the competing electron savaging process such as oxygen reduction reaction. In this regard, higher concentration of oxygen in the suspension could have a very profound negative effect on the efficiency of the Pt photodeposition [62].

1.8.2. Photodeposition of Pt on WO_3

Photodeposition of Pt on WO_3 could significantly improve the photocatalytic oxidation of air or water pollution. For example, uncovered WO_3 does have some performance in oxidation of acetaldehyde but it is not able to decompose of acetic acid and isopropyl alcohol. One of the reasons for this positive impact is the nature of the reduction of the oxygen. WO_3 itself could not provide the enough energy for the electron in the conduction band to reduce oxygen. However, reduction of the oxygen could follow different chemical path in which electrons could be provided with less energy, from the surface of the deposited Pt, and finalize the reduction of oxygen [62].

1.8.3. Photodeposition of Pt on CdS

This system has been studied more than other Pt deposition on semiconductor materials. Different types of hole scavengers, and organic and aqueous environments have been used in the literatures. Even different sources of Pt salt have been utilized for this purpose. Different precursors of Pt produce different Pt ion complex with negative or positive charge. It this regard, substrates with local negative charge, could not attract, for example negatively charged $[PtCl_6]^{-2}$ that is from H_2PtCl_6 [62].

Studied has showed that increasing the illumination time could increase the size of Pt particle. Also, higher illumination could increase there ate of deposition but until a limited amount, as the charge production reaches its saturation limit. Some studies have shown that replacing hole scavengers with a primary or secondary amines could block the active sites of CdS and ban the Pt deposition [62].

Photodeposition of Pt on CdS, in acidic environment with the $H_2\ PtCl_6.xH_2O$ and N_2 purging, involves the formation of PtS on CdS, as CdS is mildly dissolved in water. This compound (CdS/PtS) had a very low activity but after calcination and turning the Pt compound into Pt^0, the activity increases. However, when the medium is basic the Pt is deposited in oxide form ($Pt(OH)_2$ or PtO_2). Figure 1.8 demonstrates the parameters used in studying the photodeposition of Pt on CdS [62].

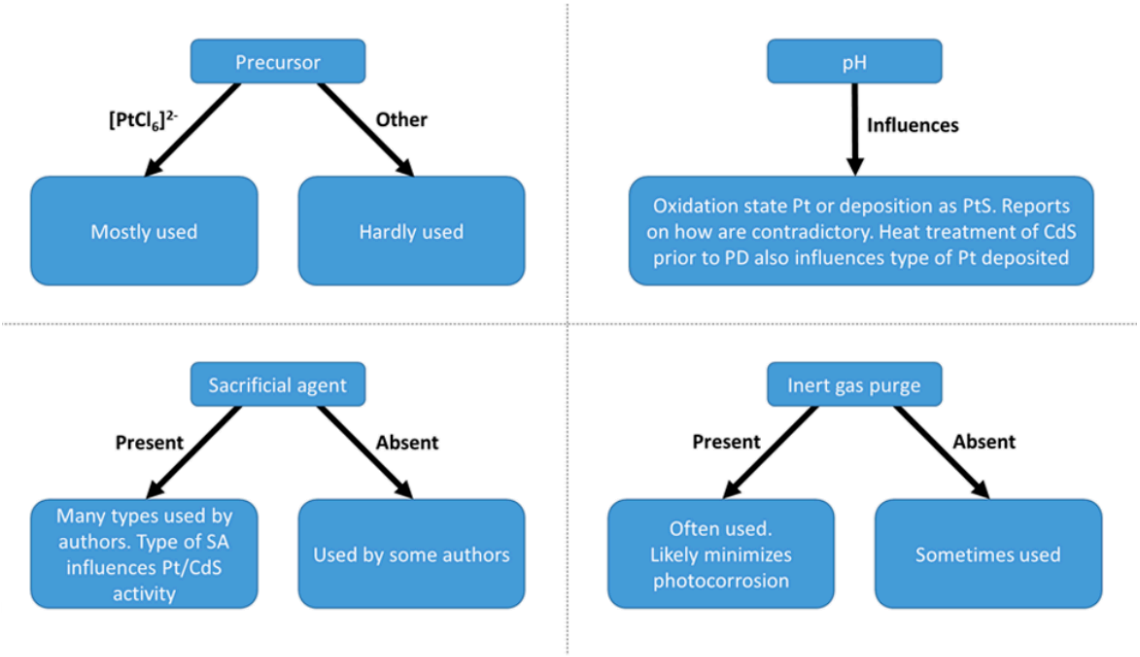

Figure 1.8. Studying scheme of Pt photodeposition on CdS [62]

Based on the main focus of the present study, the mechanism of platinum photocatalytic deposition on semiconductor materials could be described as follows [63]:

- First, the Pt containing complex should be adsorbed on the surface of the semiconductor.
- Then, separation between the electron and holes of the semiconductor occur due to the energy of the photon.
- Further, stepwise reduction of the platinum complex into the elemental form occurs.
- Formation of Pt crystallites takes place by two possible routes:
    - Either agglomeration of individual Pt atoms.
    - Or reduction of the complexes at the metallic nuclei's surface.

In a study conducted by Wenderich et al. [47] the effect of the Pt complex adsorption and deposition was discussed from the kinetic points of view. When the adsorption and photocatalytic deposition of $[PtCl_6]^{2-}$ is kinetically fast, the resultant particle were more in metallic form while slow deposition of Pt resulted in smaller Pt particles mostly in oxidized states [47]. Another important fact about the photocatalytic deposition of metal particles on semiconductor materials is the light-controlled metal formation [46], which will be discussed along the following passages.

1.9. Graphene oxide: a photocatalyst

Graphene oxide has a tunable electronic band gap and therefore, demonstrates photocatalytic properties [42][28][40,41] that can also be used as an electron acceptor for solar cells [58]. Using graphene oxide as a photocatalyst is linked to a study conducted on water splitting [42] in which an aqueous suspension of graphene oxide mixed with methanol was employed for hydrogen production by using UV light illumination. In that study, the photocatalytic process itself was the ultimate application of the graphene oxide. However, there are reports that graphene oxide has been used as a support for catalysts, for instance, gold [64] and copper [65], for dye-degradation.

1.9.1. Band gap modulation of graphene-oxide

Functional group-covered graphene layers could be an ideal support as the photocatalysts to deposit metal particles on its specific spots. In fact, the covalent band and disturbance caused by these covalent band of functional groups open the band gap of graphene. By illuminating the functionally decorated graphene layers with a proper wavelength UV-light, electrons are excited and could be used for the photocatalytic reactions. The oxidation of graphite is the necessary step in exfoliating its layer. The result of the oxidation and exfoliation is heavily oxidized graphene layers with a wide band gap. The size of this band gap depends on the level of the oxidation. By adjusting the oxidation time or partially reducing the graphene oxide layers the band gap modulation could be achieved [66].

Band gap modulation of graphene oxide must result in a stable form of partially reduced graphene oxide. Otherwise, over the time the instability of the layers causes the continuous oxygen level change and band instability. This is because of the different oxidation time or the type of the oxidant that causes different functional groups that are not stable equally. Some oxygen functional groups such as hydroxyl and epoxide could be easily detached but other types like carbonyl and carboxyl are hard to be detached. As a result, GO itself is not a suitable- and stable-band gap semiconductor. One should reduce it partially to have more stable functional groups remained on its surface and hence a stable band gap. For this reason, reduction of GO with a mild reducing agent has been proposed [66].

Figure 1.9, shows the band energy level of partially reduced graphene oxide (PRGO) and the redox potential of different electrochemical reaction. The band structure of graphene is associated to the excitation of electrons from π to π^* band. However, in the

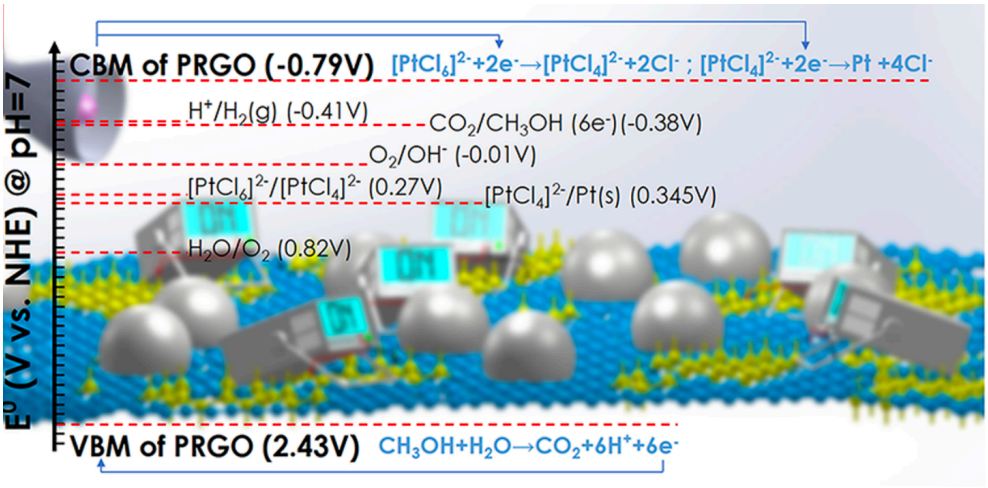

Figure 1.9. Energy band diagram of PRGO with the electrochemical reactions with respect to it [66]

case of oxygen functional group the valance band changes to the 2p orbital of oxygen. In this regard different concertation of oxygen functional groups changes the maximum energy of valance band. However, the conduction band is not being changed as it is π* bond . Figure 1.9 shows the energy level of the electrochemical reactions happening in an aqueous solution of photocatalytic deposition of Pt on PRGO semiconductors. As it can be seen oxygen reduction is in competence with the reduction of platinum. As a result, deoxygenation of the suspension with an inert gas is essential.

1.10. Scavenging the hole

There are chemicals which could be used to scavenge the hole in VB by their oxidation preference [61], so the electron in CB would be responsible for the reduction of metal ions [28][48][52]. A study conducted by Wenderich et al. [47] demonstrated that existence of hole scavengers could change the phase and composition of the deposited metal particles. They showed a very high dependence of $[PtCl6]^{2-}$ adsorption and Pt photodeposition on the duration of illumination and steps, and that both of the adsorption and deposition depends on the existence of methanol as the hole scavenger. Without using the hole scavenger the Pt particles were mostly in small size with oxidized states while using methanol resulted in kinetically faster disposition of clustered metallic Pt particles [47].

1.11. Computational materials science

1.11.1. Machine learning

One of the main challenges in using machine learning methods in materials science and engineering is the selection of the meaningful input and outputs. In this section, the basic terminology and concept of machine learning and neural network algorithm is being explained [67].

1.11.1.1. Terminology

Labels

Labels are the properties that we are predicting. In this study we are trying to predict the **cyclic voltammetry** of the photocatalytic prepared samples with input data of the synthesis procedure. So, the labels (output) will be a matrix of the entire current density points or selection of current density points from the CV graph.

Features

Features are the input values (here, synthesis parameters such as UV-on and UV-off) to give to the algorithm. Each sample in the first section of the study was synthesized with a series of setup parameters which could be considered as the input matrix with four elements. The input matrix consists of the UV pulse parameters, including UV on- and off-time, total synthesis time, and the duty cycle.

1.11.1.2. Training the model

Some portion of the samples (both the input and output data) is used to train the algorithm. In this case both the input matrix and the current density points from CV graph are given to the algorithm, and by some iteration, the algorithm adopt itself to predict the output (the CV) of an unknown matrix of input variables.

1.11.1.3. Linear regression

To explain the learning procedure that happens in machine learning, we can give an example in which an output, such as the price of air conditioners, could have a relationship with the weather temperatures. If we draw a graph that shows the point each of which

demonstrating the price in a week with an average temperature during that week, we could have some figure like figure 1.10 (y= the price and X_1= is the parameter affecting y). As we can see in this hypothetical situation the price is linearly increasing as the temperature increases. Drawing a straight line through points could show the linear relationship. The equation of the linear line is:

$$y = mx + b \quad (1.9)$$

- y is the price—the value we're trying to predict.
- m is the slope of the line.
- x is the temperature—the value of our input feature.
- b is the y-intercept.

In machine learning the equation could be little different:

$$y' = b + w_1 x_1 \quad (1.10)$$

- y' is the predicted label (a desired output).
- b is the bias (the y-intercept), sometimes referred to as w_0.
- w_1 is the weight of feature 1. Weight is the same concept as the "slope" m in the traditional equation of a line.
- x_1 is a feature (a known input).

So, if we have found the values for w_1 and b, for any unknown value of temperature we could predict the price of air-conditioned. For more complicated situation, the price value could depend on different types of parameters rather than just one input:

$$y' = b + w_1 x_1 + w_2 x_2 + w_3 x_3 \quad (1.11)$$

The job of training the model is to find the best value for weights and bias from known outputs and old inputs to put it in the equation and predict the unknown outputs from new inputs.

1.11.1.4.Loss

The term “loss” demonstrates the different value between the predicted output and the real output. If during the training process, the difference between all the price and the predicted value that the model has found is zero the model is perfect. The main goal of training is to find the lowest value of loss.

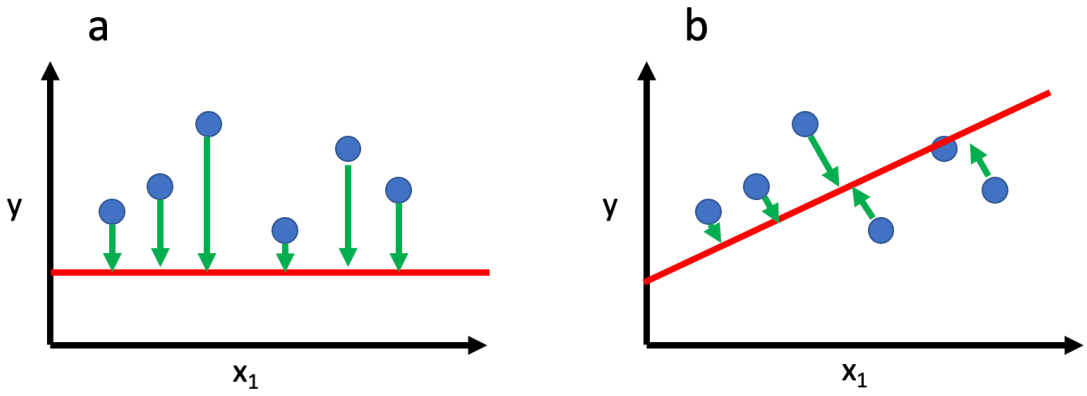

Figure 1.10. graphical representation of loss values for two different linear problem, for similar features. a) high loss and b) low loss

In figure 1.10 the loss in the left graph is higher than the right graph. In other word the right model is more successful in predicting the output values.

If we want to put the loss value into mathematical equation to find its minimum value, one of the easiest methods is defining the loss function as squared loss function, or as:

= the square of the difference between the label and the prediction

= (observation - prediction(x))^2

= (y - y')^2

The term "observation" means the real value, and "prediction" shows the value that the model is giving to us. The above equation is for one sample, or one point in the graph. To calculate the loss function over the entire data set, with the defined number of samples, we will use mean square error, is the average squared loss per example over the whole dataset. For this, we write the summation of all the squared losses of individual samples and divide the value to the number of samples.

$$MSE = \frac{1}{N}\sum_{(x,y)\in D}\big(y - prediction(x)\big)^2 \qquad 1.12$$

- (x,y) is a sample:
  - x is the set of features, or the input let's say, that the model uses to make predictions.
  - y is the example's label, the real price, here.
- prediction(x) is a function of the weights and bias in combination with the set of features x.
- D is a data set containing many labeled samples, which are (x,y) pairs.
- N is the number of samples in D.

1.11.1.5. Iterative trial-and-error process to train the model

Figure 1.11 demonstrates the iterative process based on which the algorithm uses to reduce the loss or in other word train itself:

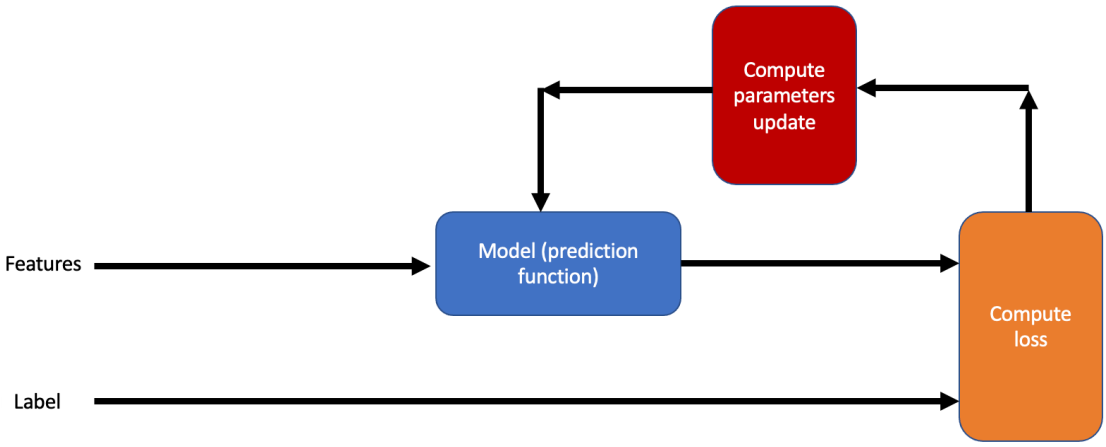

Figure 1.11. Workflow of iterative trial-and-error process for training

The procedure is as follows: the algorithm picks random value for weights and the bias and finds a predicted value for the input of "x" (if we have one input but for several inputs also the model does the same).

$$y' = b + w_1 x_1 \qquad 1.13$$

- y': The model's prediction for features x
- y: The correct label corresponding to features x.

in the next step the model calculates the loss function and by a method suggest or produce new weights and bias. The process based on which the model produces new weights and the bias after calculating the loss function will be discussed later. Let's assume that the new parameters are produced, and then new loss function is calculated by them. This loop continues until the model finds the lowest value for the loss function. Usually, the iteration continues until the loss function does not change or changes very slowly. When that happens, you can say your model is converged.

1.11.1.6. Gradient Descent

Figure 1.12 demonstrates the value of loss for the entire value of weights (for one sample with one input). For multiparameter samples, the graph would be multidimensional. As

you can see, there is minimum value for the loss function that comes from specific amount of weight coefficients.

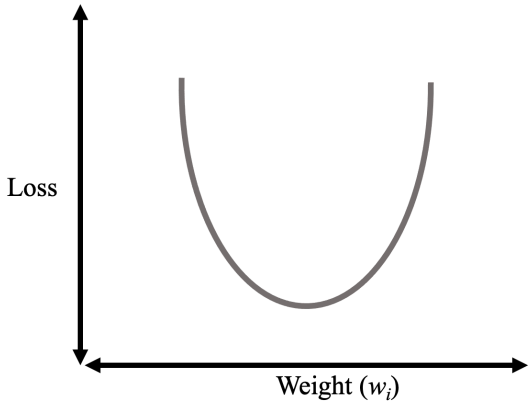

Figure 1.12. Convex loss vs. weight plot

If our random chosen values for w is shown in the following graph, Figure 1.13, we could use a method named gradient descendent to find the minimum value.

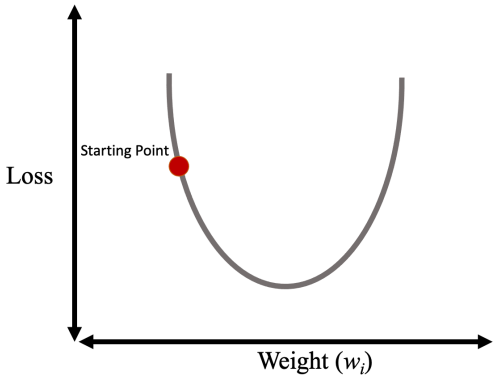

Figure 1.13. A random value in the loss-weight plot

By calculating the gradient of the point at the loss curve function, we could see that the slop of the tangent line is also the direction of the gradient. For multivariable prediction function, the gradient could be calculated by partial derivatives over weights. As it was mentioned, the gradient has value and direction. The gradient direction is always toward increasing the loss function. In this example the gradient direction is toward left. However, the gradient descendent algorithm always takes the negative of the direction to find the minimum value, in this example toward the right. To find the next point, or the next value for the weight, the algorithm add some fraction of the gradient magnitude to the previous weight and find the next point(Figure 1.14).

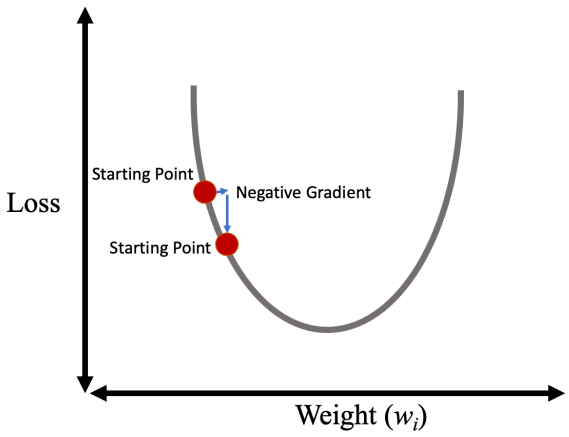

Figure 1.14. Gradient step toward the next point

This process continues until the algorithm finds the minimum value for ws.

1.11.1.7. Learning rate

It was mentioned that gradient descendent has direction and magnitude. The algorithm will multiply the gradient by a scalar number, i.e., learning rate, and add the result to the previous w to find the new w. If this multiplying coefficient is too small, the difference between the two consecutive weights are too small and the speed toward finding the minimum of the loss function will be slow (Figure 1.15). However, if the multiply coefficient, the learning rate, is too large, the step would be too large and even pass the minimum point. At this situation, more iteration will just result in the fluctuation of the loss value and not converging, even could result in an increase in the loss function (Figure 1.16).

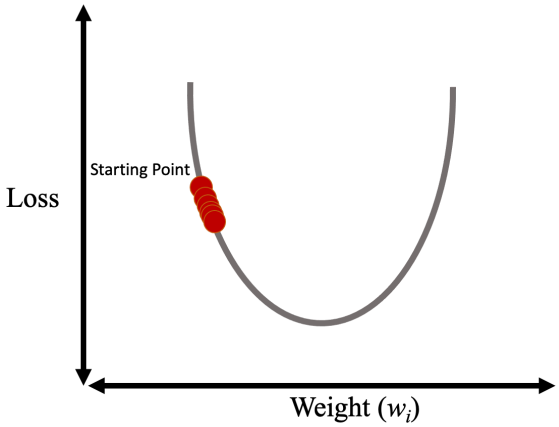

Figure 1.15. Small learning rate

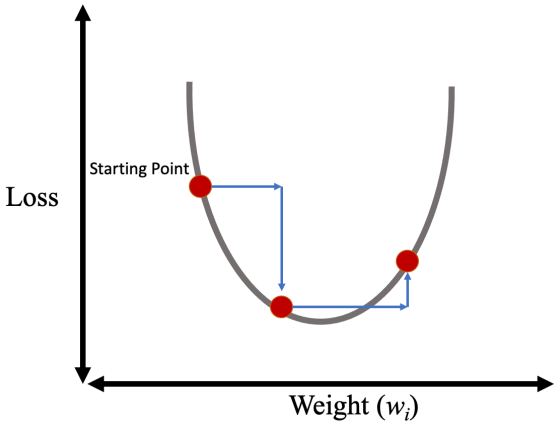

Figure 1.16. Large learning rate

1.11.1.8.Over fitting

When finding the proper weights and the bias to have the minimum loss, there is a chance that the algorithm ends up in the overfitting trap. Overfitting means: the algorithm is doing well in finding the relation between the inputs and outputs for the known-given data but doing poorly in predicting the new set of outputs from new inputs. To avoid this, not all the samples' data is given to the algorithm. Instead, some portion of the samples is used to validate the model. It means than, from some portion of the samples' just the input values, the features, are given to the algorithm and the result will be compared with the real outputs. If it has predicted well, it means it is not overfitted. To increase the accuracy of model one could even divide the dataset into three categories: Training set, Validation set and Test set (Figure 1.17).

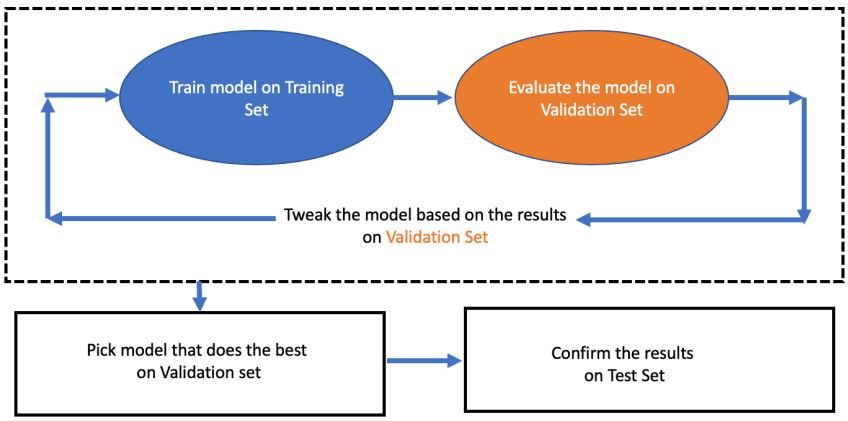

Figure 1.17. a better workflow for training and finding the meaningful weights

1.11.1.9.Feature engineering

The process of creating a vector or matrix consisting of a meaningful number which represents the raw input data is called feature engineering. It is because the raw input value never comes in a vector, categorized and normalized form. This especially when the input is not a number and is a string value, such as a name of chemical. To find a proper numerical value which represents the input parameters, we need to engineer the inputs. Most of the time in machine learning modelling is spent on feature engineering.

Scaling feature values

Scaling the feature values means converting the numbers from their natural range (for example from 200 to 1200) into the standard range (0 to 1 or -1 to +1). This is very beneficial when there are multiple features with different range of values. The benefits come from:

- faster conversion
- avoiding the NaN trap (happens when the floating number exceeds in some ways)
- preventing the algorithm to put more weight values on the data with wider range.

Mean normalization:

It is the subtraction of the average value of a specific feature from a sample.

By combining the scaling and the mean normalization we could have:

$$x_i := \frac{x_i - \mu_i}{s_i} \qquad 1.14$$

Where μi is the **average** of all the values for feature (i) and si is the range of values (max - min), or si is the standard deviation.

1.11.1.10. Feature crosses

Sometimes, the output value does not only depend on each feature individually, but also on a complex form of them, such as the multiplication of x1 and x2 or division of them. This is the properties of nonlinear problem. In figure 1.18, we cannot draw a straight line and separate the dots with different colors. It this case, introducing a third feature of x3 =

x1*x2 makes the algorithm nonlinear and the model treat this third feature as another feature with its specific weight.

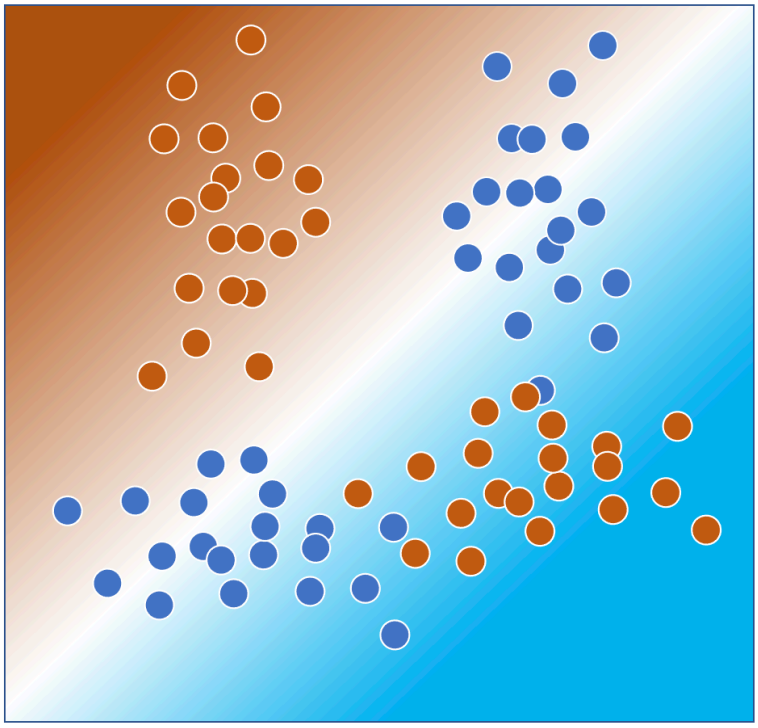

Figure 1.18. A nonlinear classification problem

1.11.1.11. Classification: Prediction bias

Figure 1.19 is showing the case in which the predicted result is in good consistency with the real outputs of a dataset.

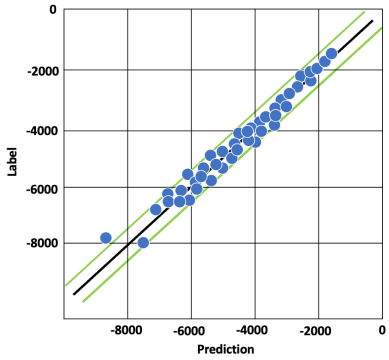

Figure 1.19. Predication bias curve

1.11.1.12. Neural Networks

Recall the nonlinear problem above. We mentioned that in some regression problems, linear combination of input (features) with their weight and the bias could not predict the correct output (labels). For these types of problems, we introduce a nonlinear combination of inputs (multiplication or division) to be able to model the problem. However, if the problem is more complicated, what would be the solution (Figure 1.20)?

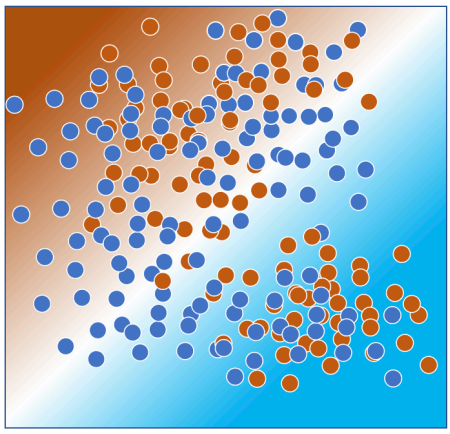

Figure 1.20. A more complex nonlinear classification problem

In highly complicated problems we can use a nonlinear function between the inputs and outputs that is named activation function. In the Figure 1.21, addition of hidden layers to add combination of input data does not change the linearity of the model, until we add the layer of activation function to it (Figure 1.22) [67].

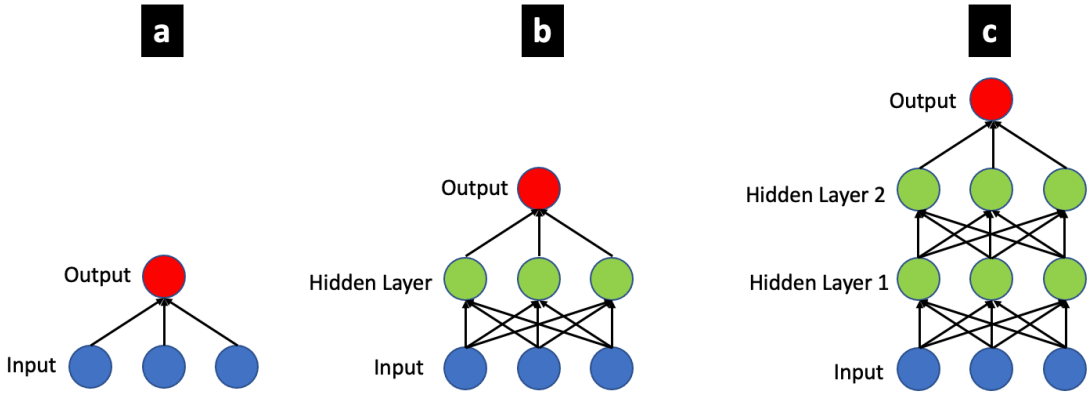

Figure 1.21. a) linear model as a graph, b) graph of two-layer model, and c) graph of three layer model

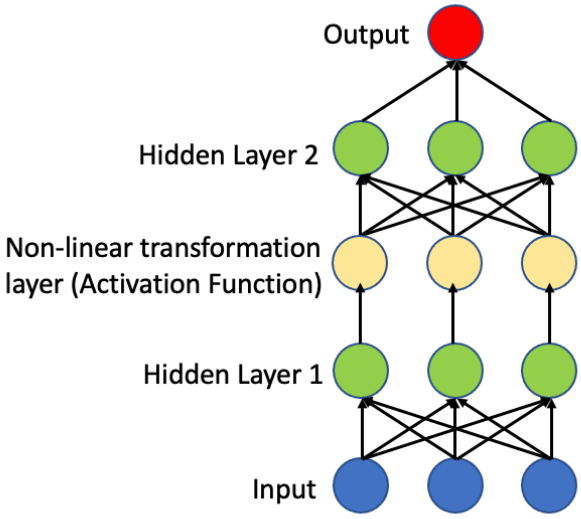

Figure 1.22. Adding the non-linear transformation layer (activation function) to change the modelling from linear to non-linear one

There are different types of activation functions. For example, the Sigmoid function is one of them (Equation 1.13 and Figure. 1.23).

$$F(x) = \frac{1}{1 + e^{-x}} \tag{1.15}$$

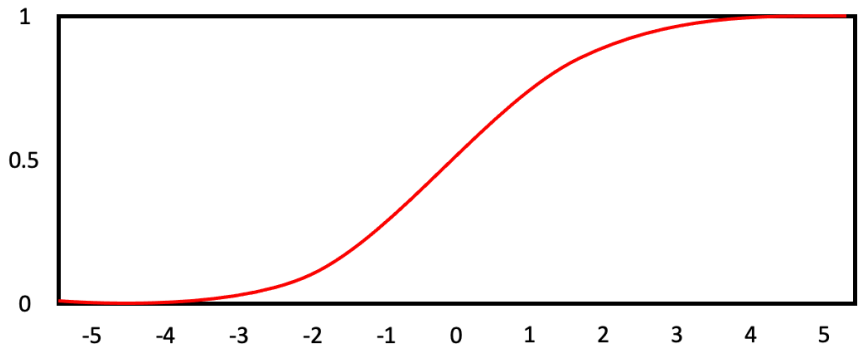

Figure 1.23. Sigmoid activation function

The action of activation function σ of a node could be represented by:

$$\sigma(w.x + b) \tag{1.16}$$

1.11.2. Density Functional Theory

1.11.2.1.First Principles or *ab initio* model

Excluding any type of experimental data in predicting the properties of materials and using just the fundamental characteristics and theory of materials plus mathematical equation means first principles or ab initio modeling.

Quantum Mechanics is the fundamental theory of materials, elements, and chemicals. Quantum physics provides you with numbers and equations that you may use to write down reality and display it using mathematical expressions.

The issue is the equations' complexity, which necessitates the use of supercomputers to solve them. The complex Schrödinger equation is the source of these equations. When we hear the phrases "supercomputers and calculations," we should remember that materials modeling is a multidisciplinary area that includes materials science, physics, chemistry, mathematics, numerics, and software engineering. Why are we interested in simulating the real world? Allow things to be as they are. The forecast is the answer. Many scientists desire to know ahead of time what their experimental outcomes will be or what their material attributes will be. As a result, materials modeling becomes critical. You may not have access to a certain chemical, or the synthesis conditions are difficult to manage, or you are unsure of the qualities of the end product.

1.11.2.2.Density Functional Theory (DFT)

DFT is a computation method that approximates the solution to the Schrödinger equation. It was founded on the premise that electrons in materials behave like an inhomogeneous gas. DFT provides contemporary technologies with the capacity to simulate materials. In terms of accuracy and computation time, DFT is still being refined.

We might use the catalyst design for hydrogen evolution process as an example of a modeling application in novel material design (HER). To be a good contender to replace pricey platinum catalysts, the Gibbs energy for hydrogen adsorption on the catalyst should be about zero in this case. DFT may be used to compute the G of hydrogen adsorption by estimating the total energy of the system before and after chemically adsorption of H^+. The associated Gibbs energy shift due to deterioration may also be used to determine the stability of the hypothetical catalyst.

1.11.2.3.Schrödinger equation

- **Particles Interactions**

In all materials, there are only electrons and nuclei. We need to figure out how they interact, and then we need to figure out how much energy is in the bundle as a whole. Electrons and nuclei repel one other, whereas electrons and nuclei attract one another. Internal energy is generated by these repulsions and attractions (Coulomb Interactions). The energies are as follows if "d" is the distance between the particles:

$$E_{ee} = \frac{e * e}{4\pi\epsilon_0 d_1} \quad 1.17$$

$$E_{nn} = \frac{Ze * Ze}{4\pi\epsilon_0 d_2} \quad 1.18$$

$$E_{ne} = -\frac{Ze * Ze}{4\pi\epsilon_0 d_3} \quad 1.19$$

The negative sign in the Equation 1.17 shows the attraction.

1.11.2.4.Many body Schrödinger equation

Determining the wavefunction of a quantum particle in any area or point of interest is necessary for describing quantum particle behavior (the main goal is to find the behavior of particles: any kind of behavior like electronic structure). To put it another way, the particles have distinct behaviors at different places in space, r, and we must compute the wave function at that point to find out what they are. [68].

1.11.2.5.Wave Function

Wave function, Ψ(r), It is a positional function. It also shows (from a viewpoint) how likely it is to discover the electron at location (r) (Figure 1.24). If the wave function at a given location is 0, the electron is not there.

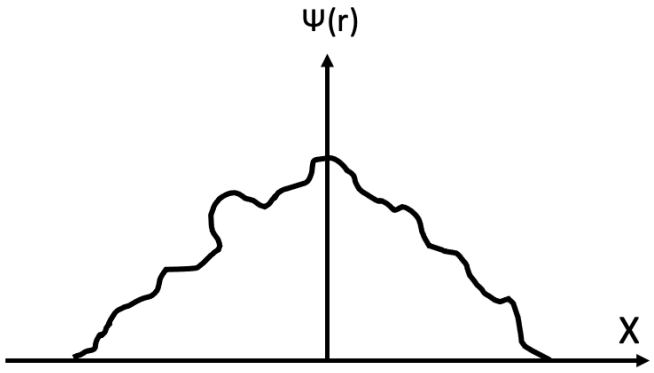

Figure 1.24. Representation of wave function as a function position.

By solving the Schrödinger equation, we may determine the wave function. The time-independent Schrödinger equation may be applied to the investigation of stationary electron-ic characteristics of materials.

$$(\text{Kinetic energy, Potential Energy})\Psi = E\Psi \qquad 1.20$$

E is the stationary state's energy eigenvalue, and $|\Psi|^2$ is the probability of locating the appropriate particle at point r.

1.11.2.6.Schrödinger equation for a single electron

If we only imagine an electron in a box with a V(r) potential surrounding it, we may write:

$$\left[\frac{p^2}{2m_e} + V(r)\right]\Psi(r) = E\Psi(r) \qquad 1.21$$

m_e is the electron mass and ρ is the momentum**.**

$$p = -i\,\hbar\nabla \qquad 1.22$$

$$\nabla = u_x\frac{\delta}{\delta x} + u_y\frac{\delta}{\delta y} + u_z\frac{\delta}{\delta z}$$

$\hbar$ is the reduced Planck constant.

If we calculate the Equation 1.19 and find the ψ_0 as the answer for the lowest energy of a single electron system then the electron distribution at position (r) can be given by: $|\psi_o(r)|^2$

1.11.2.7.Schrödinger equation for many electrons and nuclei

However, linearly adding singular contributions from particles is not correct for systems with numerous nuclei and electrons. We'll need the many-body wave function in this case Ψ. If r is the position of electrons and R is the positions of nuclei, we can write:

$\Psi = \Psi (r_1, r_{2,\ldots,} r_N; R_1, R_2, \ldots, R_M)$

It was mentioned that $|\psi_o(r)|^2$ is the probability of finding the corresponding particle at the position r. The probability of the existence of the 1st electron at r_1 and 2nd electron at r_2 and so forth we can write: $|\Psi (r_1, r_{2,\ldots,} r_N; R_1, R_2, \ldots, R_M)|^2$. The summation of all the probabilities for all arrangements could give the density at the position r. Here we sum these:

1. Probability of finding the electron 1 at all r, while 2 is at r_2, 3 is in r_3, and...
2. Probability of finding the electron 2 at all r, while 1 is at r_1, 3 is in r_3, and...
3. Probability of finding the electron 3 at all r, while 1 is at r1, 2 is at r2, and...

The first one is:

$$\rho (r_1 = r) = \int |\Psi (r_1, r_{2,\ldots,} r_N; R_1, R_2, \ldots, R_M)|^2 dr_2 dr_3 \ldots dR_1 dR_2 \ldots dR_M \qquad 1.23$$

1.11.2.8.Electron or charge density in the material

The density of electrons at point r (finding any electron at r) equals

$$n(r) = \rho (r_1 = r) + \rho (r_2 = r) + \rho (r_3 = r) + \ldots + \rho (r_N = r) \qquad 1.24$$

Because electrons are not particles that can be labeled or distinguished from one another, all the ρs are similar and may be written as n = N*ρ.

N = electron numbers, so

$$n(r) = N \int |\Psi (r_1, r_{2,\ldots,} r_N; R_1, R_2, \ldots, R_M)|^2 dr_2 dr_3 \ldots dR_1 dR_2 \ldots dR_M \qquad 1.25$$

Integration n (charge density) all over the materials gives the number of electrons.

$$\int n(r) dr = N \qquad 1.26$$

In a nutshell, charge density is the density of the charge dispersion in a substance. The greater the amount of n, the more likely we are to discover the electron in position r, the denser the charge distribution. The number of electrons is calculated by adding the charge density across the materials (integration). The wavefunction integration is normalized to one throughout the content.

1.11.2.9.Finally, the equation

Now we can write the many-body equation.

$$\text{(Kinetic energy + Potential Energy)}\Psi = E_{tot}\Psi \quad 1.27$$

The total kinetic energy of all electrons and nuclei is called kinetic energy. The combined attraction and repulsion energies between electrons and nuclei are referred to as potential energy.

$$[-\sum_i \frac{\hbar^2}{2m_e} \nabla_i^2 - \sum_I \frac{\hbar^2}{2M_i} \nabla_I^2 \quad 1.28$$

is the kinetic energy of both types of particles

$$+\frac{1}{2}\sum_{i\neq j} \frac{e^2}{4\pi\epsilon_0} \frac{1}{|r_i - r_j|} \quad 1.29$$

is potential btw electrons

$$+\frac{1}{2}\sum_{I\neq J} \frac{e^2}{4\pi\epsilon_0} \frac{Z_I - Z_J}{|R_I - R_J|} \quad 1.30$$

is potential btw protons

$$-\sum_{i,I} \frac{e^2}{4\pi\epsilon_0} \frac{Z_I}{|r_i - R_I|}]\Psi \quad 1.31$$

potential btw electron and protons

$= E_{tot}\Psi$

This is the most generic equation. Without the external field, the materials are stable and do not change over time.

The system's lowest energy, E, might be driven by solving this equation. We might then deduce all of the material's characteristics, such as elastic behavior and formation enthalpy, from this energy. However, it is almost always difficult to solve.

1.11.2.10. Simplifying the equation appearance

The form of the equation would be easier if we divided all components of the preceding equation by the Hartree energy. (In the hydrogen atom, the Hartree energy is the lowest potential energy between electron and proton.)

$$E_{Ha} = e^2/(4\pi\epsilon_0 a_0) \quad 1.32$$

$$-\sum_i \frac{1}{2} a_0^2 \nabla_i^2 - \sum_I \frac{1}{2\left(\frac{M_I}{m_e}\right)} a_0^2 \nabla_I^2 + \frac{1}{2}\sum_{i\neq j} \frac{a_0}{|r_i - r_j|} + \frac{1}{2}\sum_{I\neq J} Z_I Z_J \frac{a_0}{|R_I - R_J|}] \Psi = \frac{E_{tot}}{E_{Ha}} \Psi \quad 1.33$$

The equation gets easier if we treat the Hartree energy as one unit, the a_0 as one bohr, and m_e as one a.u.

$$-\sum_i \frac{1}{2} \nabla_i^2 - \sum_I \frac{1}{2(M_I)} \nabla_I^2 - \sum_{i,J} \frac{Z_I}{|r_i - R_J|} + \frac{1}{2}\sum_{i\neq j} \frac{1}{|r_i - r_j|} + \frac{1}{2}\sum_{I\neq J} \frac{Z_I Z_J}{|R_I - R_J|}] \Psi = E_{tot} \Psi \quad 1.34$$

Only the atomic mass and atomic numbers are required in this case..

Approximations:

- Because nuclei do not move in solids or molecules, we may ignore their kinetic energy and instead add the potential energy between nuclei to the right-hand side of the equation as a constant value..
- The potential that the proton imposes on the electrons is also the 2nd term from the left. This will be known as V. (r)

$$[-\sum_i \frac{1}{2} \nabla_i^2 - \sum_i V_n(r_i) + \frac{1}{2}\sum_{i\neq j} \frac{1}{|r_i - r_j|}] \Psi = E\Psi \quad 1.35$$

$$\hat{H}\Psi = E\Psi \quad 1.36$$

In the equation, H is referred to as the Hamiltonian..

So far, we've just developed the right equation for modeling the materials. However, how should we approach this problem? What should we do with electron-electron interactions (the third element from the left)?

Some concepts and definitions:

1. When we change the spin or location of two electrons, the sign of their wave function changes, according to the Pauli exclusion principle.
2. The interaction of electrons has a significant impact, which we cannot overlook.
3. The potential is created by the clouds of electrons in the materials, and this potential impacts electrons. The "Hartree Potential" of an electron in this field of potential exists (VH).

1.11.2.11. More simplification of the equation:

We may suppose that the electrons do not interact with each other initially, omitting the third element and just applying the Hartree potential to them. In this case, the single-electron equation changes to:

$$\left[-\frac{\nabla^2}{2} + V_n(r) + V_H(r)\right]\phi_i(r) = \epsilon_i\phi_i(r) \quad 1.37$$

The wave function of one electron is ϕ obtained by solving this equation, and the charge density is written as:

$$n(r) = \sum_i |\phi_i(r)|^2 \quad 1.38$$

This equation is also satisfied by the Hartree potential:

$$\nabla^2 V_H(r) = -4\pi n(r) \quad 1.39$$

Mean-field approximation is the name for this method. In this case, electrons do not interact with one another and behave as classical particles..

1.11.2.12. Step by step adding the other potentials to the equation

Equation 1.37 is derived from classical quantum mechanics, as we already said. Let's add the potentials that matter here one by one to get to quantum realm.

One of the potentials that should be introduced is one that prevents two electrons from occupying the same state at the same time (Pauli exclusion principle). We call it V_x. The repulsion between the electrons gives rise to another potential. This potential reduces the chances of discovering an electron in close proximity to another electron. It means that the closer you get to the second e, the less likely you are to find it. This potential is referred to as the correlation potential, and it is shown by V_c. Note that: The nature of these two potentials is still unknown, but they exist.

$$[-\nabla^2/2 + V_n(r) + V_H(r) + V_x(r) + V_c(r)]\phi_i(r) = \epsilon_i\phi_i(r) \quad 1.40$$

In a solid, this is the equation for solitary electrons. Equation 1.36 may be used to obtain the total electron density by solving this. Until now, we've been using the many-body equation to represent the potentials imposed on single electrons in a solid by combining single-electron equations. The next step is to locate these potentials in ground states (DFT)..

1.11.2.13. And again: Density Functional Theory (DFT)

Before using the preceding equations, consider the following assertion (by Hohenberg and Kohn):

The functional of the electron density is the ground state energy (the lowest level of energy) of materials.: E = F[n]

The functionals of the many-body wave function of that state are the functionals of other levels of energy (excited states).:

- If E = ground state energy ≫ E = F[n(r)]
- If E = the excited state energy ≫ E = F[$\Psi(r_1, \ldots, r_N)$]

We mentioned above that the Hamiltonian could be written as:

$$\widehat{H}(r_1, \ldots, r_N) = -\sum_i \frac{1}{2}\nabla_i^2 + \sum_i V_n(r_i) + \frac{1}{2}\sum_{i \neq j} \frac{1}{|r_i - r_j|} \quad 1.41$$

The Energy is written in this form (an experimental):

$$E = <\Psi|\widehat{H}|\Psi> = \int dr_1 \ldots dr_N \Psi^*(r_1, \ldots, r_N)\widehat{H}\Psi(r_1, \ldots, r_N) \quad 1.42$$

So:

$$E\widehat{T} = -\sum_i \frac{1}{2}\nabla_i^2,\ \widehat{W} = \frac{1}{2}\sum_{i \neq j} \frac{1}{|r_i - r_j|} \quad 1.43$$

$$E = <\Psi|\Sigma_i V_n(r)|\Psi> + <\Psi|\widehat{T} + \widehat{W}|\Psi> \quad 1.44$$

$$E = \int dr.n(r)V_n(r) + <\Psi|\widehat{T} + \widehat{W}|\Psi> \quad 1.45$$

The energy that originates from the nucleus is the first term in the energy equation, and it is dependent on the electron density, as indicated.

The influence of the second component (kinetic and coulomb energy) on electron density is less evident.

The 2nd term of the energy equation may now be changed to the sum of the energies of the independent electrons (kinetic and coulomb) plus unknown portions..

$$E = F[n] \quad 1.46$$

$$= \int dr.n(r)V_n(r) \sum_i \int dr\, \phi_i^*(r)\frac{\nabla^2}{2}\phi_i(r) + \frac{1}{2}\int\int drdr' \frac{n(r)n(r')}{|r - r'|} + E_{xc}[n]$$

$$E = F[n]$$

$$= \overbrace{\underbrace{\int d\mathbf{r}\, n(\mathbf{r}) V_{\mathrm{n}}(\mathbf{r})}_{\text{External potential}} - \underbrace{\sum_i \int d\mathbf{r}\, \phi_i^*(\mathbf{r}) \frac{\nabla^2}{2} \phi_i(\mathbf{r})}_{\text{Kinetic energy}} + \underbrace{\frac{1}{2} \iint d\mathbf{r}\, d\mathbf{r}'\, \frac{n(\mathbf{r}) n(\mathbf{r}')}{|\mathbf{r} - \mathbf{r}'|}}_{\text{Hartree energy}}}^{\text{Total energy in the independent electrons approximation}} + \underbrace{E_{xc}[n]}_{\text{XC energy}}.$$

E_{xc} is an unknown component of the energy that is likewise a functional of electron density, and it should be estimated as follows:

The electron density (the ground-state electron density) minimizes the energy at the ground state (at ground state the energy is the functional of the electron density). This derivative might be referred to as a variational principle equation.:

$$\frac{\delta F[n]}{\delta n} \; at \; n_0 \; = 0 \qquad 1.47$$

Mathematical equations result in:

$$[-\nabla^2/2 + V_n(r) + V_H(r) + V_{xc}(r)]\phi_i(r) = \epsilon_i \phi_i(r) \qquad 1.48$$

This is the Kohn-Sham equation, which is comparable to the equation for a single electron in a many-body system. The point is this::

$$V_{xc}(r) = \frac{\delta E_{xc}[n]}{\delta n} \; at \; n_0 \qquad 1.49$$

So, there is a functional, $E_{xc}[n]$ that leads to the total energy. This functional is unknown and is related to the *exchange and correlation* potential.

1.11.2.14. Approximation of exchange correlation functional (One example for the approximation):

The Local Density Approximation (LDA)

The electrons are treated as particles in a homogeneous gas in this manner. A gas in a box containing nuclei. In a homogeneous gas model, we may compute the exchange and correlation energies as a function of electron density, as well as consider particle repulsion.

In reality, we take the actual material to be a sum of infinitesimal-width local regions with homogeneous gas behavior (Figure 1.25).

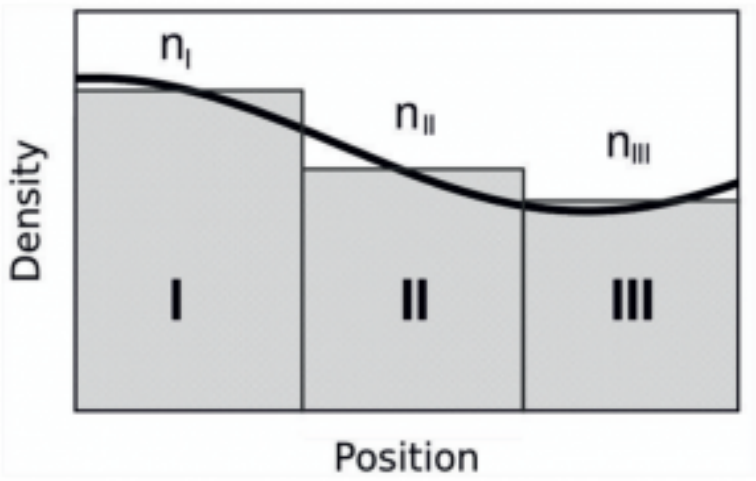

Figure 1.25. Approximation of the electron density with the homogenous gas in small areas of the sample.

$$dE_{xc} = \frac{E_{xc}^{HEG}[n(r)]}{V} dr \qquad 1.50$$

(E_{xc}^{HEG} is well defined and calculated in [1])

We can compute the exchange and correlation potential (by derivation over density) and determine the Kohn Sham equation using the exchange and correlation energy..

1.11.2.15. Self-consistent calculations (SCF)

The Kohn-Sham equation is not as simple to solve as one may think.:

$$[-\nabla^2/2 + V_{tot}(r)]\phi_i(r) = \epsilon_i\phi_i(r) \qquad 1.51$$

$$V_{tot}(r) = V_n(r) + V_H(r) + V_{xc}(r)$$

$$V_n(r) = -\sum_I \frac{Z_I}{|r_i - R_I|}$$

$$\nabla^2 V_H(r) = -4\pi n(r)$$

$$V_{xc}(r) = \frac{\delta E_{xc}[n]}{\delta n}(r)$$

$$n(r) = \Sigma_i|\phi_i(r)|^2$$

- The electron density is required to determine the ground state energy.
- We must solve the equation and determine the wave function in order to determine the electron density
- We need the total potentials to find the wave function.

- We also need the electron density to find the potentials

So, as we see we are trapped in a loop that to find one thing we need another thing. But:

- We start by putting the atom locations and a random approximation for the electron density because the atoms aren't interacting with each other.
- Then, based on the electron density, determine the potentials.
- Then look for the wave function.
- Calculate the new electron density using this wave function.
- If the new electron density is identical to the prior one, we preserve it and compute the energy.
- If not, move to the second step and utilize the new electron density.

Finally, by having the ground state energy of the sample the software or the code package could calculate its other properties.

1.12. The aim of the study

There are several reports on the positive impact of graphene based supports used as a potential anchoring for electrocatalysts in PEMFC catalyst layer (CL) [2,4,17], [40]. Also, the H_2 up-taking ability of graphene has been reported as an another positive factor in CL [69]. By employing a proper method such as photo-deposition, a stronger interaction between the Pt particles and the graphitic domains of carbon-based support

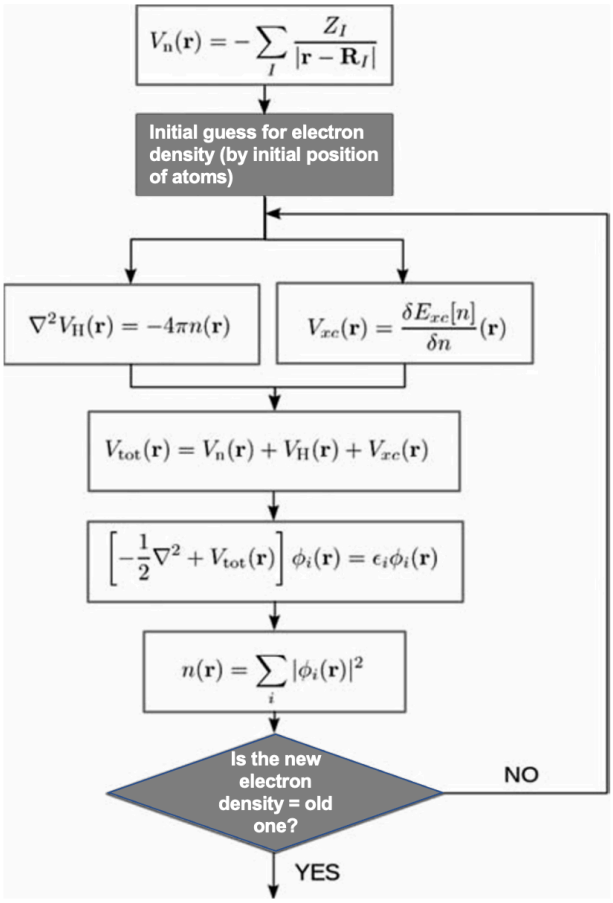

has been reported which could play a crucial role in the catalytic performance of the composite [14].

In this study, the utilization of a hand-made UV-assisted photocatalytic deposition setup provided a light-controlled system based on which the illumination period (on and off time) was well-controlled and the resulted catalyst materials were studied. The novelty of the current study is summarized as follows:

1. Application of PRGO as the main semiconductor and reducing agent, and not using other semiconductors such as TiO_2 [70][43][12] for electron generation and Pt deposition.
2. Utilization of a scalable, well controlled, hand-made UV reactor, by which controlling the irradiation time and duration is precisely controlled.
3. A simple aqueous solution-based process in which no specific chemicals for the reaction are required.
4. Non-toxic and green chemical modification of PRGO/Pt composites with highly concentrated ascorbic acid, as a necessary post treatment, to enhance the catalytic activity.

In the second part of the experimental section of this dissertation, two different types of chemicals, organic and inorganic (methanol and transition metal ions Co^{+2}, Ni^{2+} and Fe^{2+}) have been used as the hole scavengers and the morphology, chemical composition catalytic activity of the synthesized products were compared. The novelty of this study could be summarized as follows:

To gain a deeper knowledge about the electrocatalytic performance of Pt/Graphene-based electrocatalysts two different computational method were utilized. At first, the first part of the third chapter, one of the machine learning algorithms, artificial neural network (ANN) from MATLAB software [71] were used to model the cyclic voltammetry of the samples synthesized with pulsed UV photocatalytic deposition. The result of this part could prove the potential of this synthesis method in autonomous materials synthesis procedure if paralleled with a fast and in-situ characterization techniques. The second part of the computational chapter includes the detailed procedure of DFT modelling of H_2 adsorption of Pt/Graphene and Pt/Graphene oxide samples. The aim of this part is studying the effect of oxygen functional groups, located in the graphene plane, on the H_2 adsorption on Pt crystals, as the first step in H_2 oxidation in PEM fuel cells is the molecule adsorption and atomization on Pt particles. Also, this section could give the idea about the stable crystallin shape of Pt on graphene plane, with/without functional groups. The Quantum-Espresso package [72][73] were utilized for this purpose.

CHAPTER 2. Photocatalytic Synthesis of Pt/Graphene: The Effect of Pulsed- UV illumination, and the Addition of Transition Metal Ions (Co^{2+}, Ni^{2+} or Fe^{2+}) on the Structural and Electrochemical Properties of the Electrocatalysts

2.1. Introduction

This chapter covers the experimental part of the current dissertation. Two types of parameters were chosen to optimize the photocatalytic deposition of highly active Pt particles on graphene-based supports. In both categories of samples, a final chemical reduction with a highly concentrated ascorbic acid solution is needed to activate the samples. Sample preparation and structural and compositional analysis were similar for both studies. The first part of this chapter focuses on the experiential procedures for the electrocatalysts synthesis and manipulating the setup parameters, pulsed-UV parameters such as UV-on and UV-off duration, effect on the metallic state of the deposited Pt^{X+} particles and hence its electrocatalytic activities. The second part of this chapter (starting from section 2.4.) explain the results coming from the optimization of the chemical parameters, the type of hole scavenger, in synthesis of Pt/rGO electrocatalysts.

2.2. Materials and methods

2.2.1. GO synthesis

Graphene oxide samples were prepared by using the modified Hummers method[15] with few modifications. The detailed procedure used for GO synthesis and reactor design was proposed in Reference 21 and the video article was provided in Reference 22. Two grams of graphite powder (>99%, Sigma-Aldrich) were added to 100 mL of sulfuric acid (H_2SO_4, 98%, Sigma-Aldrich) and the mixture was placed in an ice-water bath. The temperature of the mixture was brought near to 0°C. Then, over the course of 30 minutes, 12 g of potassium permanganate ($KMnO_4$, >99%, Merck) was gradually added to the mixture to ensure that the exothermic reaction was not suddenly causing an increase in temperature. To complete the oxidation process, the stirring was continued for 6 more hours at room temperature and then 500 mL of deionized (DI) water was poured into the reaction bath. This was followed by the gradual addition of 30 mL hydrogen peroxide (H_2O_2, 30%, Sigma-Aldrich) to the mixture to hinder the reaction. The resulting oxidized graphite was then washed and centrifuged repeatedly with DI water, 1 M hydrochloric

acid (HCl, 37%, Sigma-Aldrich) and again washed by using DI water. The suspension was then sonicated to exfoliate the GO layers. The unoxidized or unexfoliated particles were removed through precipitation resulting from centrifugation. The concentration of the suspension was adjusted to 0.2 g L^{-1} by adding the proper amount of DI water to the suspension for the following steps.

2.2.2. PRGO synthesis

To further modify the band structure of GO sheets, the suspension was added to the same volume of 4 M sodium hydroxide (NaOH, >98%, Sigma-Aldrich) solution and stir-refluxed at 90°C for 8 hours. The product was repeatedly washed and centrifuged by adding DI water. At this stage, the GO sheets were converted into PRGO which had stable band structures in the range of semiconductor materials, suitable for photocatalytic deposition of Pt as described earlier.

2.2.3. Photocatalytic deposition of Pt

To ensure that UV light penetrates the suspension which passes through the setup's central quartz tube (Figure 2.1), further diluted PRGO suspension (50 mg L^{-1}) was prepared. Pt^{+4} ions were added to the suspension (20 wt% with respect to initial GO) by adding hexachloroplatinic acid (H_2PtCl_6, 8 wt% solution in water, Sigma-Aldrich). Methanol (10 vol% with respect to each batch volume) was chosen to act as the hole scavenger. The suspension was stirred for 30 minutes alongside N_2 gas purging to flush out dissolved oxygen. Although we tried to seal the circulation path of the suspension, to exert a positive pressure of N_2 gas inside the circulation path, and also to remove the produced gas resulting from reactions, the N_2 purging was continued during the whole process. Figure 2.1 also shows the graphical presentation of the reactor and parameters used to adjust it. The characteristics of the designed setup and parameters arising from the type of quartz tubes (50 cm [L] × 0.5 cm [Ø]) inside the core part of the reactor, and reservoir size and the pump type enabled us to plan a series of synthesis procedures to verify whether the proposed method was suitable for PEMFC catalyst preparation or not. Two types of quartz tubes were used (Figure 2.1); 100-UV tube for uncovered or bare quartz tube and 20-UV tube which was 80% covered with an aluminum tape in a repeated manner to provide a pulsed illumination inside the reactor.

While the suspension passes through the opaque pipe connections, reservoir, and aluminum-covered parts of the quartz tube, the electron cannot be excited into the

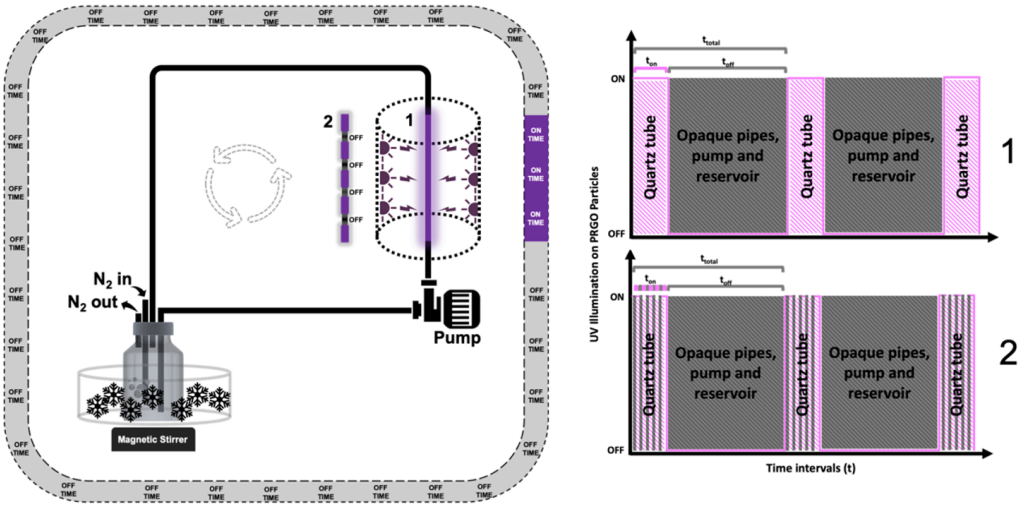

Figure 2.1. The pulsed-UV photocatalytic deposition reactor with its two types of quarts tubes: 1) periodically covered and 2) bare tube with their produced UV pulse forms on the right.

conduction band of PRGO and, consequently, cannot reduce the metal ions. We call this time interval off-time (t_{off}). However, whenever it passes through the naked parts of the quartz tube, the UV light can excite the electron of the PRGO sheets from the valence band to the conduction band, this time interval is called on-time (t_{on}). These two parameters define the duty cycle (Equation 2.1):

$$\Theta\% = \frac{t_{on}}{t_{off} + t_{on}} \qquad 2.1$$

This equation shows the ratio of on-time over the total circulation time. Figure 2.1 schematically represents the mentioned time intervals and graphs which model the UV illumination vs the time. One of the advantages of the setup is its capability to operate with a wide range of suspension volumes, from milliliters to liters. The size of the reservoir and the extent of the aluminum coverage around the quartz tube determines the shape of the graphs (in Figure 2.1) which resemble a pulsed wave. Four different pulsed waves were designed by 100-UV and 20-UV tubes in addition to 270, 540, 750, and 1500 mL reservoirs.

One of the intentions in this study was to evaluate the possibility of metal photocatalytic deposition on PRGO by deposition of the oxide form of another metal as a hole scavenger. To pursue this goal, two different amounts of cobalt chloride salt ($CoCl_2.6H_2O$, > 98%, Sigma-Aldrich) were added to 1500 mL of the PRGO suspension (80 mg and 40 mg,

named as high concentration and low concentration of Co^{2+}, respectively). In addition to cobalt, two more samples with the addition of Ni^{2+} ions or Fe^{+2} ions were prepared. For the comparison methanol (10 vol. % with respect to the volume of one suspension, without cobalt precursors addition) was chosen to act as the organic whole scavenger, that was one of the samples in the previous section (studying the effect of pulsed-UV parameters).

2.2.4. Post-treatment of electrocatalysts

To further study the effect of GO structure and the Pt oxidation states on the electrocatalytic activity of the as-synthesized electrocatalysts, two groups of samples were prepared. One was prepared with the explained previous procedures (N.R., not-reduced samples) and the second group was prepared with an additional chemical modification, using a highly concentrated ascorbic acid solution (60 g L^{-1}, $C_6H_8O_6$, 99%, Sigma-Aldrich) and stir-refluxed at 90°C for about 2.5 hours (R., reduced or post-treated samples). Then these samples were centrifuged and washed repeatedly with DI water and stored for further characterizations. As an example, table 2.1 shows the samples' names and the synthesis parameters for the study in which the pulse parameters were the subject of the research.

Table 2.1. Parameters of pulsed UV illumination

Sample	**Quartz tube (%)**	**Reservoir size (mL)**	t_{on} **(s)**	t_{off} **(s)**	**Duty cycle (%)**	t_{total} **(min)**
270 ml 20UV	20	270	0.3	12	2.4	600
540 ml 100UV	100	540	1.5	24	5.8	240
750 ml 20UV	20	750	0.3	33	0.9	1660
1500 ml 100UV	100	1500	1.5	66	2.2	660

Abbreviation: UV, Ultraviolet.

2.2.5. Structural Characterization

The X-ray diffraction analysis and the diffraction patterns of the synthesized electrocatalysts were carried out by the powder XRD using a Bruker D2 Phaser X-ray diffractometer device with 1.540 Å Cu Kα radiation source (at 2θ angles 5°-90°, the scan rate of 2.4° per minute). To investigate the graphitic structure of the samples and the structural changes of the graphite after the oxidation, reduction, and Pt deposition, Raman spectroscopy was performed, using a Renishaw1000 Raman microscope (Renishaw Instruments, England) with 532 nm argon ion laser. The Pt size, morphology, and distribution were studied by high-resolution transmission electron microscopy, HRTEM (high-resolution transmission electron microscopy; JEOL JEM-ARM200CF). Image J software analysis was applied on HRTEM images to compare the Pt particle size distribution among different samples. For studying the oxidation states of Pt particles and structural differences of graphene supports, which resulted from oxygen functional groups, a high-resolution Thermo Fisher K-Alpha X-ray photoelectron spectrometer (XPS) system by using a 400 elliptic radius spot size of Al Kα monochromatic source was adopted.

2.2.6. Electrochemical characterization

The electrocatalytic activities of synthesized materials were studied in a three-compartment electrochemical cell using a rotating disc electrode (RDE) setup (Gamry Instruments Reference 3000 Potentiostat/Galvanostat/ZRA and Pine rotating control). Pt wire was the counter electrode (CE) in the setup. Due to the previous content measurement for each batch of samples, the ink preparation was simply done by adding the proper amount of DI water to the suspensions. Then, each suspension was ultrasonically agitated for at least 1 hour to break down the PRGO particles, which might have agglomerated during the centrifuging process, to acquire homogenous inks; 16.66 µL of the resulting ink was drop casted onto a glassy carbon electrode, with a surface area of 0.19625 cm^2 and then dried in an oven at 60°C. These catalyst-covered glassy carbon electrodes were used as the working electrodes (WE). For the cyclic voltammetry (CV) tests, the electrolyte (0.1 M $HClO_4$ [Aldrich]) was purged with N_2 for 30 minutes and the WE was activated and stabilized by 50 cycles, from 0.2 to 1 V (vs Ag/AgCl) at a scan rate of 100 mV s^{-1}, to obtain a stable voltammogram. To record the hydrogen reduction and oxidation reactions data, the same potential range of 0.2 to 1 V was chosen but at the scan rate of 50 mV s^{-1}. For ORR evaluation, the electrolyte was

aerated with oxygen gas and a series of linear sweep voltammetry (LSV) tests were performed in the potential range of 0 to 1 V, at a scan rate of 10 mV s^{-1} and rotation speed of 100, 400, 900, 1600 and for some samples 2500 rpm. Although Ag/AgCl reference electrode (RE) were used in all experiments, all the calculations were performed with respect to the reversible hydrogen electrode (RHE).

2.3. Pulsed-UV Illumination on Graphene Oxide: A New Strategy in Photocatalytic Synthesis of Electrocatalysts, to Control the Structural and Electrochemical Properties

1.1.2. Introduction

In the first section of studying the photocatalytic deposition of Pt particles on PRGO particles, the focus was mainly on the effect of UV-on and UV-off duration on the structural and electrochemical performance of Pt/PRGO electrocatalysts. As it was mentioned in the materials methods section, four different samples were prepared with various forms of the pulsed illumination. We divided these four samples into categories based on long- and short-time illumination-on and -off time. The following sections will discuss the detailed explanation of the synthesized catalysts.

2.3.1. Structural and compositional properties

Figure 2.2a represents the XRD spectra of electrocatalyst samples prepared under different parameter conditions. In all samples, the (111), (200), (220), and (311) planes of the platinum FCC structure are visible at 39.8°, 46.5°, 68.7°, and 82.1°, respectively. The most remarkable fact about this technique was that different UV-illumination time intervals and duty cycles could successfully deposit Pt on PRGO with the assistance of methanol as the hole scavenger. Figure 2.2a highlights the effect of the t_{off} interval on the Pt peak intensities. One of the reasons for higher intensities in diffraction patterns could be related to the more crystalline structure of the samples. Smaller crystallites have broadened peaks and bigger ones show sharpened peaks. However, because of the amorphous structure of GO and a special graph modification to remove the background peak, interpreting the peak intensities and the relative crystallinity needs considerable caution.

The distribution of Pt particles and their morphology on PRGO supports were studied via HRTEM (Figure 2.2b-j). The deposition of Pt with different t_{off} and illumination

procedures (100UV and 20UV quartz tubes) was clear in the samples. However, a more even distribution of the particles was found from the duty cycle of 2.4% which were gained from 20UV tube (270 mL suspension in the reservoir, short t_{on}, and a periodic illumination on PRGO particles) (Figures 2.2b and c). On the other hand, longer t_{off} and 20UV tube (duty cycle of 0.9%) although could cause even distribution of Pt particles, resulted in a sample with less distribution density of the particles. This sample needed a much longer t_{total} (total time for the synthesis) of around 25 hours for equal UV illumination and consistency. That might cause the evaporation of the methanol through the N_2 exit valve, leaving a suspension with less hole scavenger.

There might be an alternative scenario based on the proposed mechanism represented in (Figure 2.3). In each one step of the process, stable deposition of Pt atoms on the graphene surface requires thermodynamically and kinetically favorable pathways and reactions. When the suspension is experiencing the t_{on} intervals, excitation of the electron to CB and consequently nucleation and growth of Pt atoms are the following events (Figure 2.3a). Pt^{4+} is probably reduced to Pt^0 in two steps: 1) Pt^{4+} to Pt^{2+}, and 2) Pt^{2+} to Pt^0 [74]. If the t_{on} is small, in the 20UV tube, the two steps might not be accomplished and the final product in each circulation would be Pt^{2+}_{ads} or Pt small nuclei (some with $r < r_c$). If the reservoir container is big (longer t_{off}), 750 mL, the resultant Pt^{2+}_{ads} or nuclei have enough time to detach or settle in energetically more stable spots on PRGOs. However, with a shorter t_{off}, i.e., 270 mL reservoir, the time might not be adequate for settlement of Pt^{2+}_{ads} or nuclei, and in the UV_{on} period more ions are attached to the latter deposited ones and make the nuclei more stable, $r > r_c$. This could lead to a less Pt^0 that affects the electrocatalytic activity.

In Figures 2.2h and i, the effect of a longer t_{on} on particles distribution can be observed. A longer t_{on} may cause more crystal growth rather than nucleation in different spots. It may also cause more electron generation from one spot and reduction of ions close to each other and consequently an area with more agglomerated particles is observed.

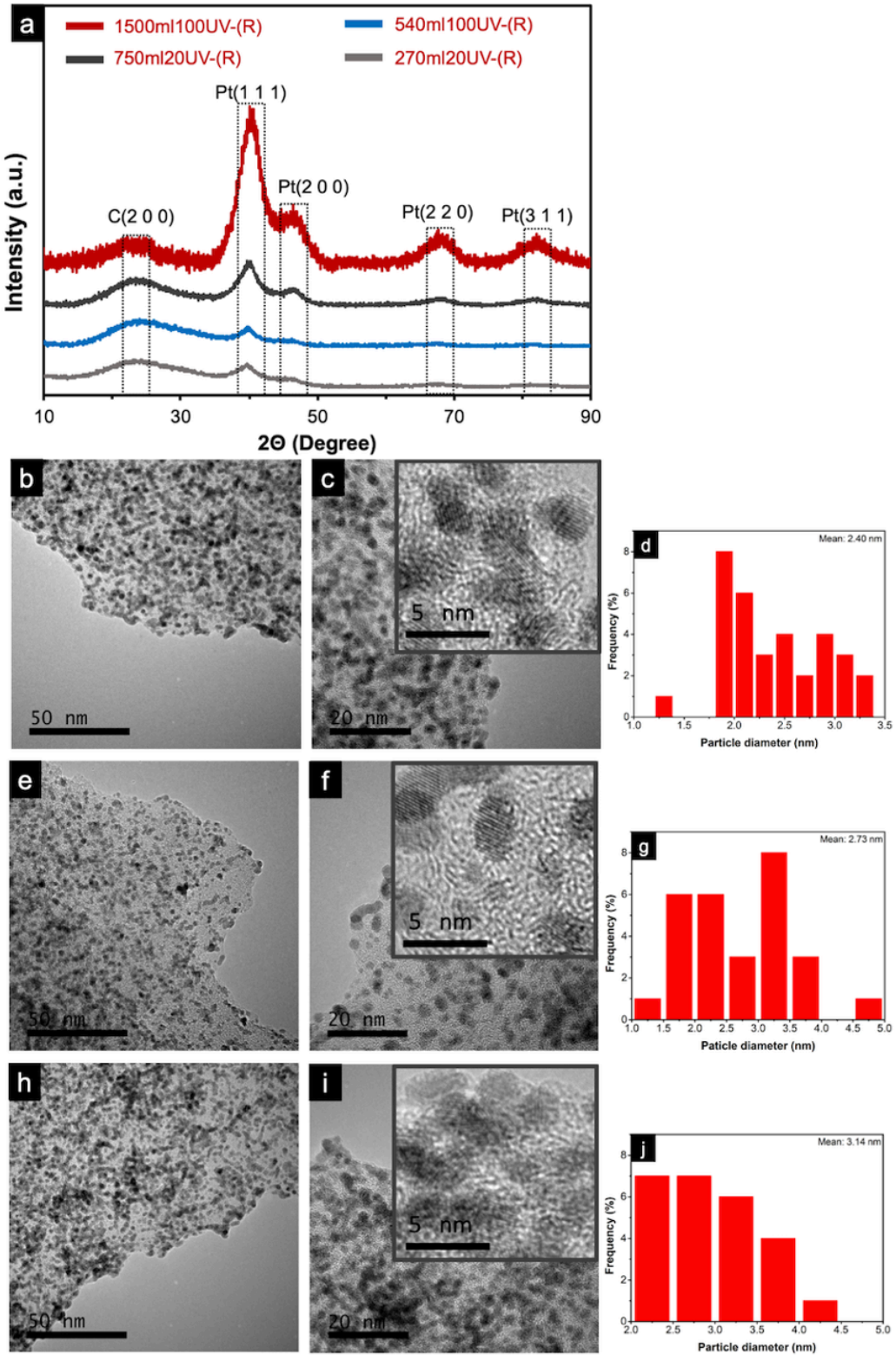

Figure 2.2. a) X-ray diffractogram of the samples prepared under different parameter conditions (R: chemically reduced by ascorbic acid solution), and TEM micrographs of Pt particles, their morphology and size distribution on PRGO support at two magnifications: b, c, and d) 270 mL solution, 20UV tube; e, f, and g) 750 mL solution,

20UV tube; h, i and j) 1500 mL solution, 100UV tube, (all the TEM results are from freshly synthesized samples without further chemical modifications).

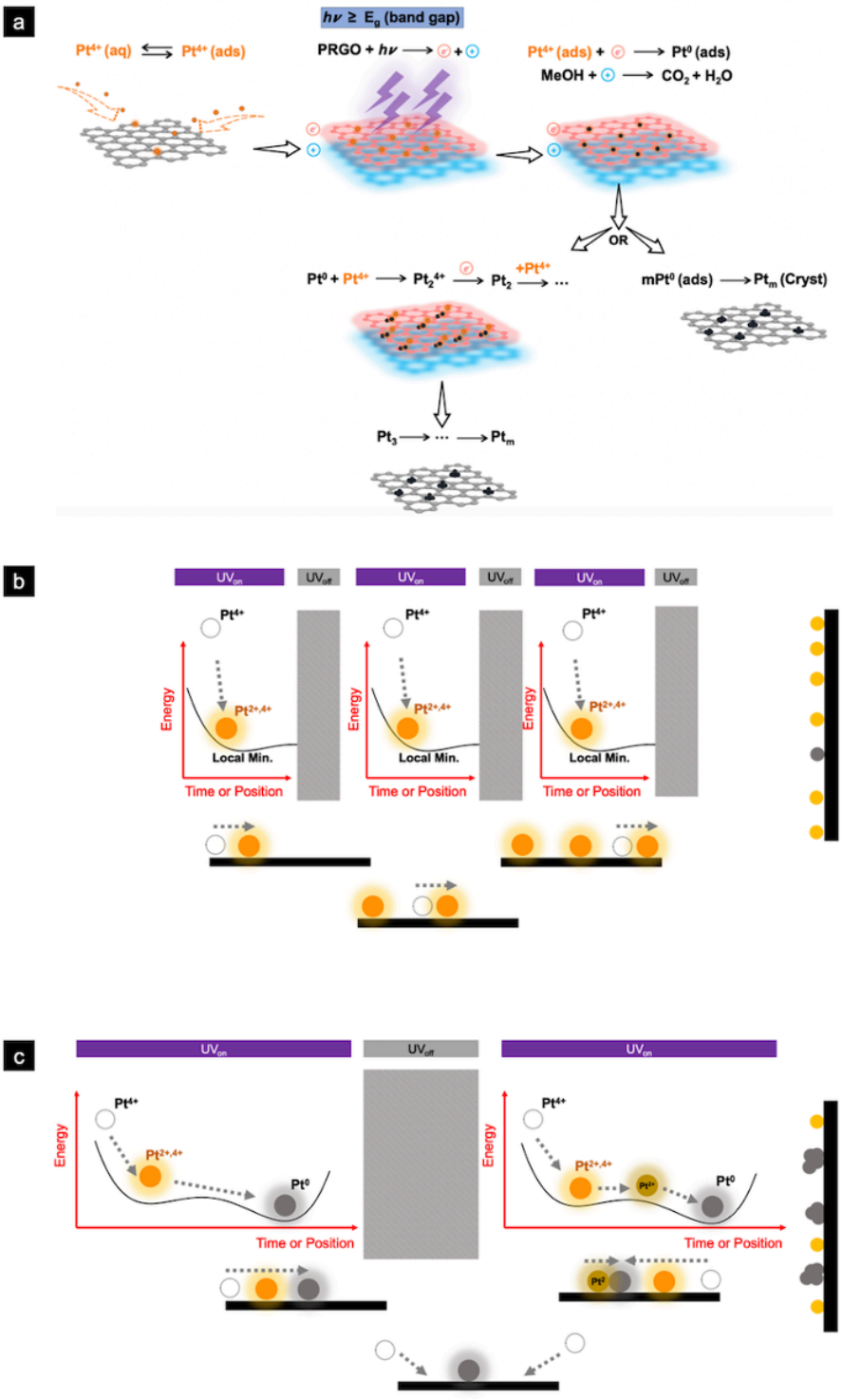

Figure 2.3. a) Alternative proposed mechanisms for Pt deposition along with oxidation of hole scavenger, and nucleation mechanism of Pt particles prepared by b) short UV on- and off-time, and c) long UV on- and off-time

To assess the effect of oxygen functional groups and Pt^{X+} particles on the G and D vibration modes of the graphene-based materials, Raman spectroscopy was conducted. To summarize, whenever carbon atoms are locked in the hexagonal structure of the perfect graphene, the breathing vibrational mode will be forbidden, and the D band is not observed. By introducing defects into the carbon lattice, some of the sp^2 carbon atoms will change to sp^3 structure and the intensity of the D band increases [75]. These defects could be vacancies, oxygen functional groups, or deposited particles. By completely oxidizing the graphene and producing graphene oxide, all carbon atoms will be sp^3 hybridized and the D band would disappear again.

There is a maximum in the D band intensity when the level of deficiencies increases. In Figure 2.4a, a higher value of I_D/I_G (= 0.95) can be seen (letter "I" represents the intensity) for partially reduced graphene oxide. In all samples, Figures 2.4b to 2.4e, further chemical modification of electrocatalysts by ascorbic acid solution resulted in a lower value of I_D/I_G. The highest I_D/I_G difference, before and after the chemical modification, belonged to the samples prepared by the lower t_{on} (20UV tube) and high t_{off} (750 mL reservoir) i.e., lowest duty cycle. These samples showed the lowest amount of Pt distribution density (Figures 2.2e and 2.2f). Among all chemically reduced samples, the highest I_D/I_G (= 0.89) value was for the samples with well Pt particles distribution (Figures 2.2b and 2.2c). This result highlights the small and well distribution of Pt particles might further distort the sp^2 structure to sp^3 structure.

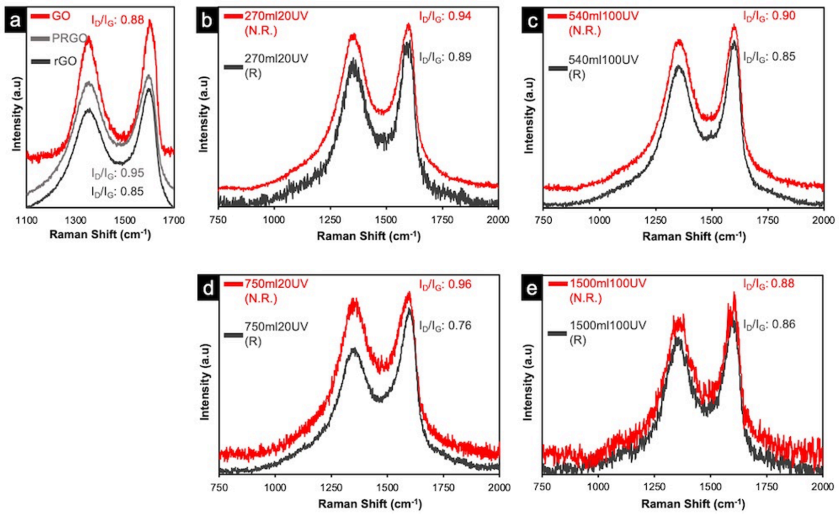

Figure 2.4. Raman spectra of GO, PRGO, and rGO at different conditions.

Chemical structure analysis of the electrocatalysts was further studied by XPS. Figure 2.5 represents the effect of synthesizing parameters and the post-treatment by highly

concentrated ascorbic acid solution on the binding energy of platinum coming from its different states, on carbon hybridization states, and oxygen functional groups. Pt 4f spectra showed mostly a doublet peak shape at 71.8 eV and 75.2 eV. It was observed that chemical modification of all samples with ascorbic acid solution caused the domination of metal Platinum (Pt^0) over Pt^{+2} and Pt^{+4} in binding energy determination (Figures $2.5a_4$, $2.5b_4$, and $2.5c_4$). Opting for a lower t_{on} i.e., the shorter period of UV irradiation in each circulation time, led to the shift in the binding energy to platinum oxide states. This could be an indication that after Pt^{+4} (aq) is adsorbed on the surface, Pt^{+4}(ads), if the provided time is sufficient, the reduction is completed step by step from Pt^{+4}(ads) to Pt^{+2} and finally to Pt^0. From Figures $2.5a_3$, $2.5b_3$, and $2.5c_3$ alongside Figures 2.3b and 2.3c it is seen that using 100UV quartz tube i.e., longer t_{on} and UV illumination, resulted in a sample with more metal Pt (Pt^0) formation as compared to the 20UV tube. Comparing XPS results with the TEM images also reveal that the early stage of Pt deposition involves a stable deposition of more Pt^{+4}. Considering Figure $2.5b_3$ (dominance of Pt^{+4} peak) and comparing it with the corresponding TEM Figures 2.2e and 2.2f (lowest disposition of Pt), suggest that the coverage of the reduced graphene oxide with Pt initially begins with the nucleation of Pt^{+4} (PtO_2) followed by the nucleation of Pt^{+2} (PtO) as is observed from Figure $2.5a_3$ (dominance of Pt^{+2} peak) and TEM Figures 2.2b and 2.2b. In other words, 20UV with periodically and short illumination time of UV light facilitated more nucleation of the Pt^{+4}. However, this nucleation could occur at any place without any position preferences on the graphene layer, especially when the t_{off} is not long enough for adsorption of the ions in a preferable place (Figure 2.3b). Increasing the t_{on} and t_{off}, could provide sufficient time for the energetically favorable adsorption of Pt^{+4}, completing the reduction process from Pt^{+4} to Pt^0 and promoting growth or Pt agglomeration rather than more nucleation at random places on the graphene surface.

Referring to the Pourbaix diagram (potential-pH) of the Pt components stability in aqueous solution [76], some important factor in the stability of platinum and platinum oxide components in water could be extracted (Figure 2.6). All Pt, $Pt(OH)_2$, PtO_2 and PtO_3 could exist in aqueous solution and cause some reactions such as hydrogen oxidation (by $Pt(OH)_2$ and turn to Pt). The stability of Pt components in Pourbaix diagram is highly dependent on the ionic complex it could form. In this study Pt-based crystals are not self-standing particles, i.e., their interaction with the graphene-based supports and also with

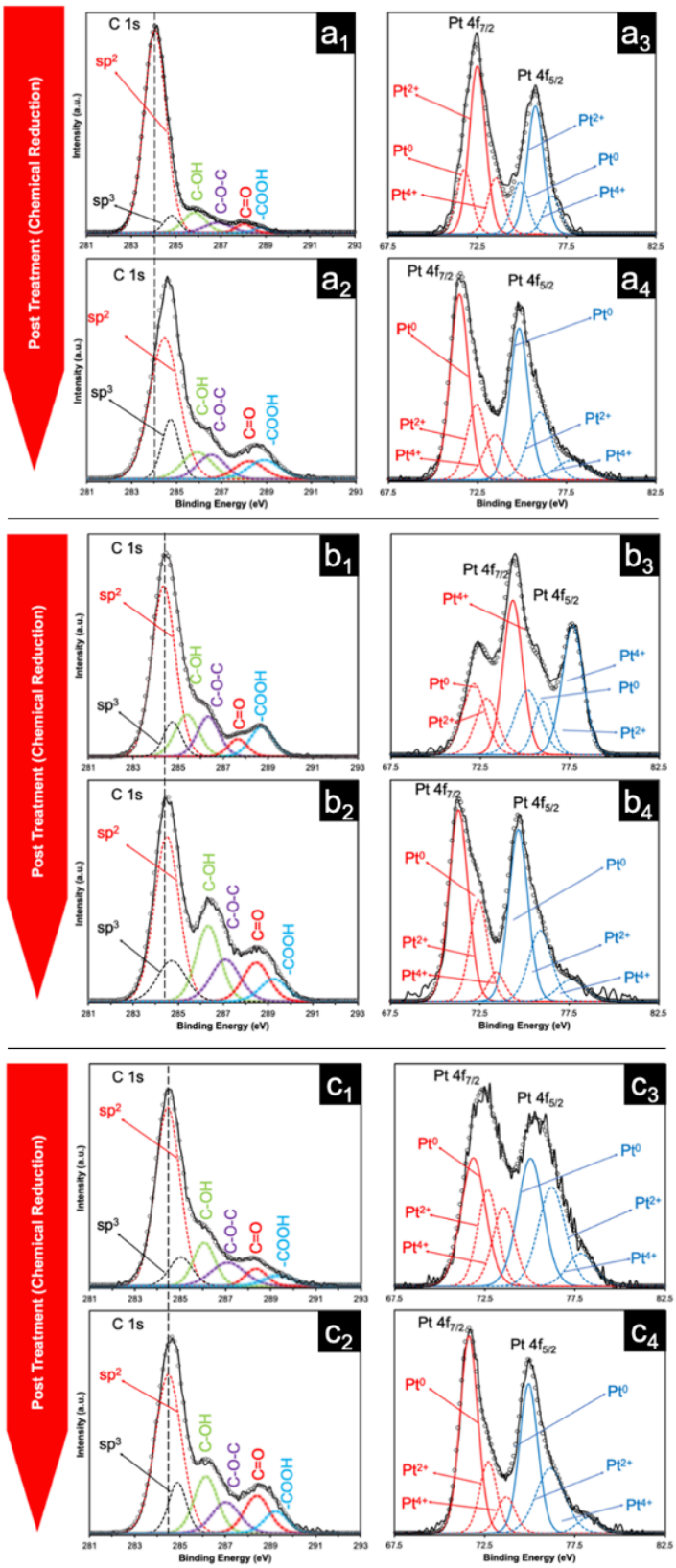

Figure 2.5. X-ray photoelectron spectroscopy (XPS) spectrum of C 1s and Pt 4f for a_x) 270 mL solution with 20-UV tube, b_x) 750 mL solution with 20-UV tube and c_x) 1500 mL solution with 100-UV tube, (x = 1, 2, 3 or 4)

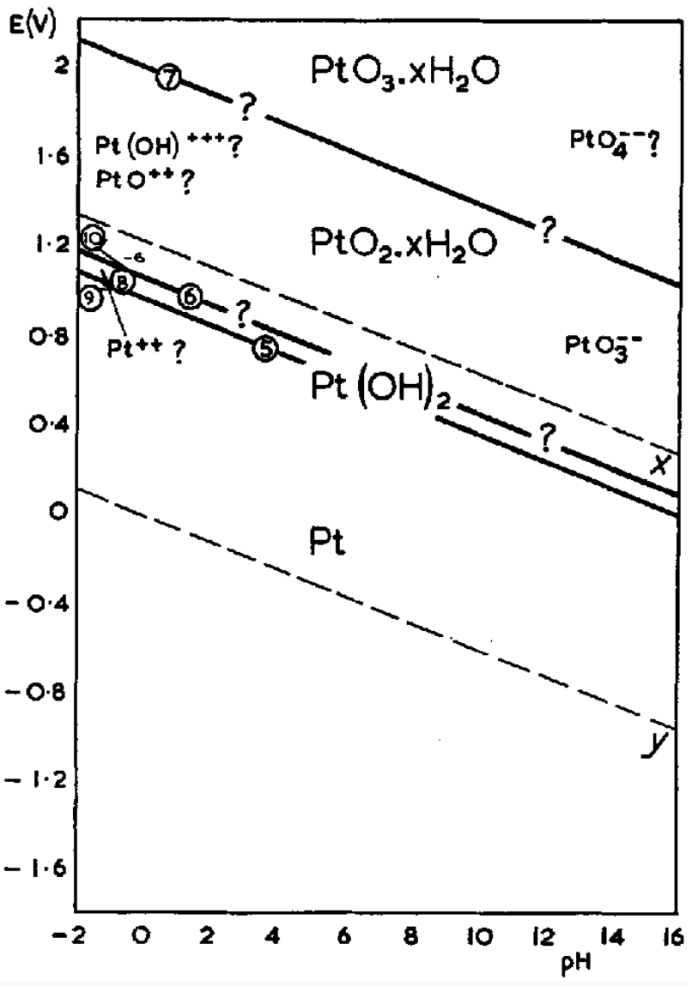

Figure 2.6. Potential-pH diagram for Pt-water system [76]

the transition metal ions (next chapter) could result in various ionic complexes that could change the stabilities of them. However, as the process of PRGO and rGO synthesis required many times washing, and reduction with highly concentrated sodium hydroxide and ascorbic acid solutions, the final aqueous solution containing the Pt/rGO had the pH value of little acidic, which could also be the reason for the negative value of the zeta potential of PRGO in various solutions, (next section of this chapter in Figure 2.12).

Deconvoluting the XPS spectra of C 1s of the graphene-based supports showed a relative increase in the binding energy of carbon by shifting toward the binding energy emerging from oxygen functional groups including hydroxides (C-OH), epoxy (C-O-C), carbonyl (-COOH), and carboxyl (C=O) after the post chemical treatment. The difference between binding energies coming from the different contributions of sp^2 and sp^3 carbon structures, before and after the ascorbic acid treatment, was quite evident. By reducing Pt^{+4} states to Pt^0, the deconvoluted peaks showed that the contribution of oxygen functional groups and the sp^3 structure increased while the sp^2 contribution decreased.

2.3.2. Electrochemical activities

To determine the number of active sites for hydrogen oxidation reaction (HOR), CV tests were performed on all synthesized samples before and after post-chemical treatment (Figure 2.6). Figure 2.6a belonged to the sample which was highlighted for the most structural change by ascorbic acid treatment and well-distributed Pt^{X+} nanoparticles. It is seen that the as-prepared sample is not showing a promising electrochemical activity with the ECSA equal to 12.36 $m^2.g^{-1}$. This low performance could be attributed to the higher nucleation rate of Pt^{2+} and less metallic Pt^0, which has a crucial effect on the electrocatalytic activity of Pt. In the previous studies, results have demonstrated a very high deposition efficiency and stability of Pt ions by this method [47,77]. Based on those results, the ECSA and ORR performance were calculated concerning 20 wt.% Pt loading which gave the minimum value of the performance and highlights the potential application of this method. As it was observed from Figures 2.6a_1, 6a_2, 6a_3, and 6a_4, through chemical reduction of Pt^{2+} to Pt^0, structural change of the carbon support and further referring to the Figure 2.6a, the resultant sample (named 270mL20UV (R)) showed higher electrocatalytic activity with the ECSA of 108.40 $m^2.g^{-1}$. Figures 2.6b and 7c belonged to the samples with the lowest electrocatalytic activity even after the chemical modification to Pt^0 state. This low activity could be a result of charge transfer barriers i.e., oxygen functional groups on the graphene sheets. As discussed earlier, longer on-time and off-time could ensure the energetically and structurally favorable placement of catalyst particles, which was not provided at the same time for these two samples. Another evidence for this hypothesis could be extracted from Figure 2.6d, which belonged to the sample with the highest activity even without the post chemical treatment. The ECSA value for this sample was equal to 101.71 $m^2.g^{-1}$ and 152.01 $m^2.g^{-1}$, for non- and modified samples, respectively. These samples had shown previously, in the Figures 2.5c_3 and 2.5c_4, Pt particles with mainly Pt^0 states, even for the as-synthesized sample, however, we could still observe binding energy change of Pt 4f and C 1s spectrums after the chemical treatment. It has been reported that the deposition of Pt on carbon support might be controlled by thermodynamic or kinetic factors, that each factor could affect the final product electrocatalytic activity. Parameters such as Pt precursors, reducing agents, additives, and reaction temperature and time could modulate the kinetic of Pt reduction from the ionic state [78].

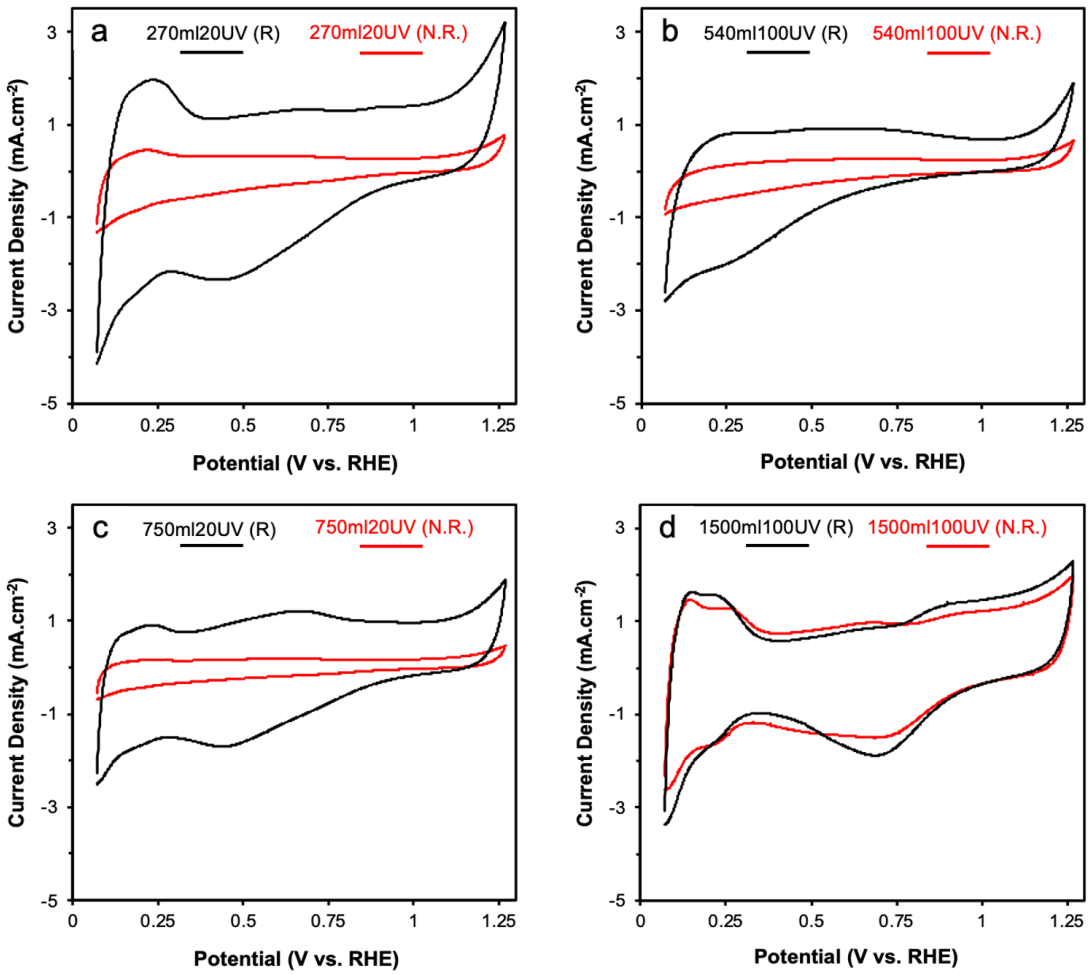

Figure 2.7. Cyclic voltammetry of a) 270 mL solution with 20UV tube, b) 540 mL solution with 100UV tube, c) 750 mL solution with 20UV tube and d) 1500 mL solution with 100UV tube (red: not-reduced with ascorbic acid, black: reduced with ascorbic acid)

To evaluate the ORR performance of the previously discussed samples, LSV tests by employing rotating disk electrode (RDE) at 100, 400, 900, and 1600 rpm, and additionally at 2500 rpm in some samples, in which the ECSA and ORR performance were among the highest values, were conducted. Like the CV results, the difference between the samples' performance was observed here (Figure 2.7). The highest difference after the final chemical treatment, among the samples, belonged to the one synthesized with 20UV tube (low t_{on}) and 270 mL reservoir (low t_{off}). Recalling the morphology of the samples, Pt^{X+} nanoparticles had been well distributed on the graphene sheets. In Figure 2.7, a mixed kinetic-diffusion-controlled region for the chemically modified sample (black curve, Figure 2.7a_x, b_x, c_x (x = 1, 2 and 3)) appears from 0.8 V to 0.95 V. Therefore, the mass activities at 0.9 V were calculated and given at table 2.2. By evaluating Figures 2.7b_1, 2.7b_2, and 2.7b_3, and Figures 2.7c_1, 2.7c_2, and 2.7c_3, the poor performance of two samples,

one with a high t_{on} (100UV tube) and low t_{off} (540 mL reservoir), and the other with a low t_{on} (20UV tube) and high t_{off} (750 mL reservoir), could be extracted. Similar to previous results, the best-chosen electrocatalyst is the one with both high values of t_{on} and t_{off} (100UV tube and 1500 mL reservoir). This variety of ECSA values is clear evidence of the strong dependence of the electrocatalytic activity on Pt oxidation states and adsorption mechanism. Samples with less metallic states and the ones without sufficient time for energetically proper adsorption (off-time) of Pt^{4+} showed the lowest ECSA value. The ORR performance of the samples with the highest ECSA value is presented in Figures $2.7d_1$, $2.7d_2$, and $2.7d_3$. Although the difference between the ORR performances of non-modified and modified types of this sample is the lowest among all other ones, based on the sensitive nature of ORR and its high dependency on the structure of the catalyst and supports (XPS and Raman results), Figure $2.7d_3$ depicts a higher performance for ORR before chemical modification with the ascorbic acid solution. The mass activity of this sample is equal to 0.083 $A.mg^{-1}$ and 0.066 $A.mg^{-1}$ for non-modified and modified ones, respectively. In previous studies in which the deposition method and/or the carbon-based materials were different the resulted mass activities have been reported to be in the range of 0.063-0.272 $A.mg^{-1}$ [79,80]. The charge transfer current coming from the kinetically controlled region, for the not-modified sample, is higher than the modified one. This could be because of graphene's different structures coming from oxygen functional groups which were shown from XPS spectra of C 1s in Figures $2.5c_1$ and $2.5c_2$. Functional groups may play as hinders in charge transfers mechanism and a higher level of oxygen (highly electronegative) functional groups might interfere with dissolved oxygen molecule adsorption and reduction. Based on a comprehensive explanation that can be found in [81], ORR involves diffusion and desorption of oxygen molecules on the surface, charge transfer from the anode to O_2 molecules, breaking the O=O bonding, and releasing the OH^- ions. The existence of oxygen functional groups with the electronegative nature of oxygen atoms could interfere with this multi-step process. Table 2.2 represents the summary of electrochemical data obtained from the samples and the affecting parameters. As a summary of the electrochemical characterizations, the inconsistency between the TEM results, and ECSA and ORR performance could just attribute to the heterogeneous charge transfer on the surface of reduced graphene oxide, and the importance of the role of Pt oxidation state on the Pt-graphene interaction and interface charge transfer.

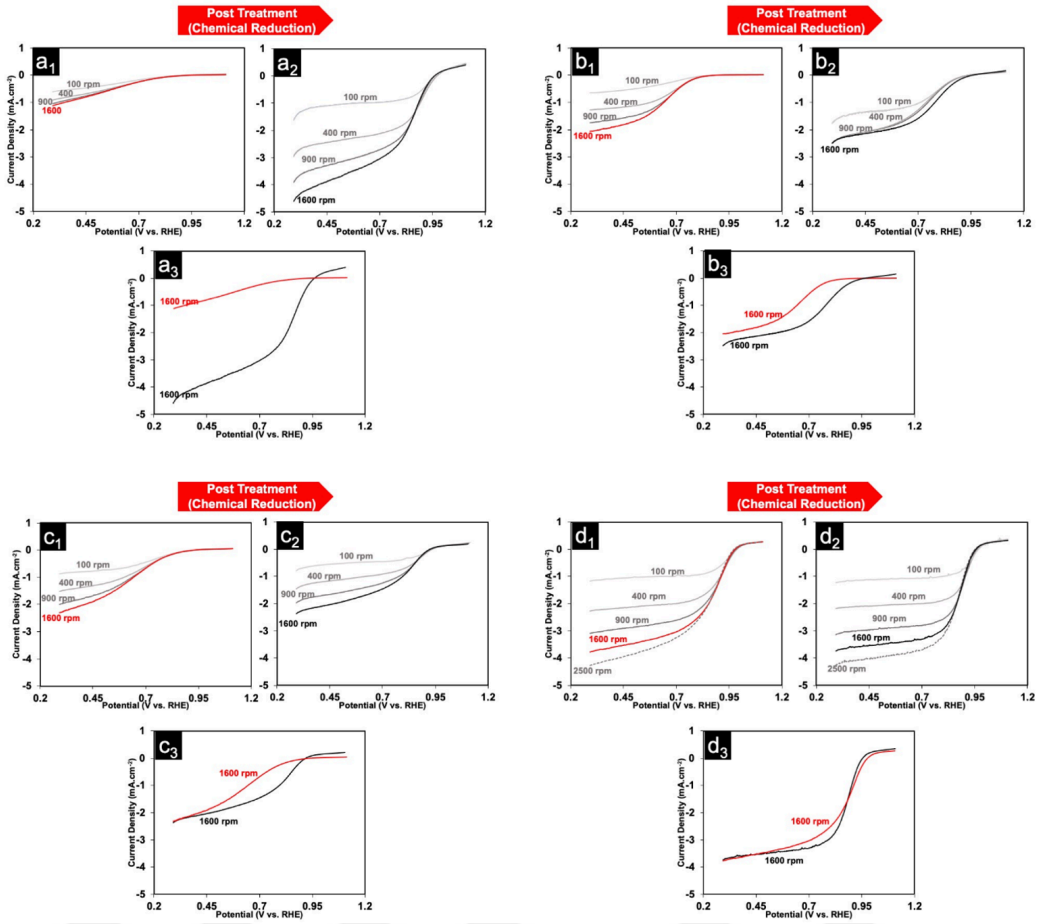

Figure 2.8. Linear sweep voltammetry of $a_{1,2,3}$) 270 mL solution with 20UV tube, $b_{1,2,3}$) 540 mL solution with 100UV tube, $c_{1,2,3}$) 750 mL solution with 20UV tube and $d_{1,2,3}$) 1500 mL solution with 100UV tube, (red: not-reduced with ascorbic acid, black: reduced with ascorbic acid)

Table 2.2. CSA and mass activity of samples synthesized with four different illumination pulses, and with (R. Sample)/without (N.R. Sample) further ascorbic acid reduction

Sample	t_{on} (s)	t_{off} (s)	t_{total} (min)	Duty Cycle (%)	ECSA (N.R. Sample) ($m^2.g^{-1}$)	ECSA (R. Sample) ($m^2.g^{-1}$)	Mass Activity (N.R. Sample) ($A.mg^{-1}$)	Mass Activity (R. Sample) ($A.mg^{-1}$)
270ml20UV	0.3	12	600	2.4	12	108	poor	0.036
540ml100UV	1.5	24	360	5.8	-	-	-	-
750ml20UV	0.3	33	1660	0.9	-	11	-	poor
1500ml100UV	1.5	66	660	2.2	102	152	0.083	0.066

2.3.3. Conclusions

This dissertation has been attributed to the new perspective on synthesis of electrocatalysts. Based on the proposed method, which uses the pulse illumination of sample suspensions with UV light, studying the photocatalytic deposition of metal/metal oxides could be achieved with precisely adjustable parameters (pulsed UV time intervals), rather than qualitative ones such as chemical types or hard-to-control ones such as temperature. Utilizing this procedure could enable one to study the different behavior of photocatalysts and metal ions, illuminated by UV or visible light, and create a database in which the best UV_{on} and UVo_{ff} for a specific performance could be selected through the trends that exist in structural and compositional properties of samples. This study has investigated the reduction and growth of Pt^{X+} on PRGO supports in an aqueous solution and their effect on the hybrid materials' electrocatalytic performance. The electronic band structure of PRGO gives it a semiconducting behavior and makes it a promising support for photocatalytic deposition of metal or metal oxide particles. Structural, morphological, and compositional characterization methods along with electrochemical evaluation were utilized to follow reduction and deposition procedures. Herein, we emphasized that uniform and even distribution of Pt nanoparticles on graphene-based materials was not the main factor in determining the catalytic performance when the kinetics and mechanism of the deposition were controlled by adsorption of Pt ions on the substrates and by the $Pt^{4+} \rightarrow Pt^{2+} \rightarrow Pt^{0}$ reduction progress. By adjusting the pulsed UV-light illumination, based on just changing the suspension volume and periodically covering the internal quartz tube, we were able to:

- control the reduction degree of Pt^{4+} to Pt^{0},
- control the nucleation and growth of Pt particles
- synthesize platinum particles with more metallic states and elevated electrocatalytic activities.

A sufficient time for Pt complex adsorption (UV_{off}) and photocatalytic reduction (UV_{on}) could result in 1) deposition of Pt ions on energetically favorable spots, and 2) synthesizing samples with dominantly Pt^{0} states and higher electrocatalytic activities, even with coarser and agglomerated structures. To further study the effect of Pt^{X+} states, and oxygen functional groups that existed on rGO's plane, a final chemical reduction with a highly concentrated ascorbic acid solution was conducted. Our results also confirmed that more metallic Pt had higher ECSA values, but the modification of rGO's functional

group could decrease the ORR performance probably due to the functional groups' effect on oxygen molecule adsorption. The future research could focus more on other types of semiconductor materials and study the deposition of oxide particles. To increase the efficiency and decrease the synthesis time, bigger setup with longer quartz tube at the heart of the reactor is necessary.

2.4. Co^{2+}, Ni^{2+}, Fe^{2+}: Promising Assistants for Photocatalytic Deposition of Highly Active Pt Electrocatalyst Particles on Graphene-based Supports

2.4.1. Introduction

The second part of the experimental section of this dissertation focused on the effect of the addition of Co^{2+}, Ni^{2+} or Fe^{2+} ions on the final properties of the Pt/PRGO electrocatalysts. The first assumption in this section was the hole scavenging characteristic that the oxidation of these ions will provide to the suspension. In this regard, no other hole scavengers were added to these suspensions. However, for the sake of control parameters, two more samples were prepared, in addition to the first three ones. The first one was the sample with as half the cobalt ions as the previously Co-assisted synthesized one, and the second one which had been synthesized before was the one synthesized with methanol as the hole scavenger (as the setup parameters were 1500mL solution, and 100 UV quartz tube).

2.4.2. Structural and compositional properties

Figure 2.8 represents the XRD spectra of electrocatalyst samples prepared under different parameter conditions. In all samples, the (111), (200), (220), and (311) planes of the platinum FCC structure are visible at 39.8°, 46.5°, 68.7°, and 82.1°, respectively. The most remarkable fact about this the effect of different metal ions on the Pt peak intensities and sharpness. One of the reasons for higher intensities in diffraction patterns could be related to the more crystalline structure of the samples. Smaller crystallites have broadened peaks and bigger ones show sharpened peaks. However, because of the amorphous structure of GO and a special graph modification to remove the background peak, interpreting the peak intensities and the relative crystallinity needs considerable caution.

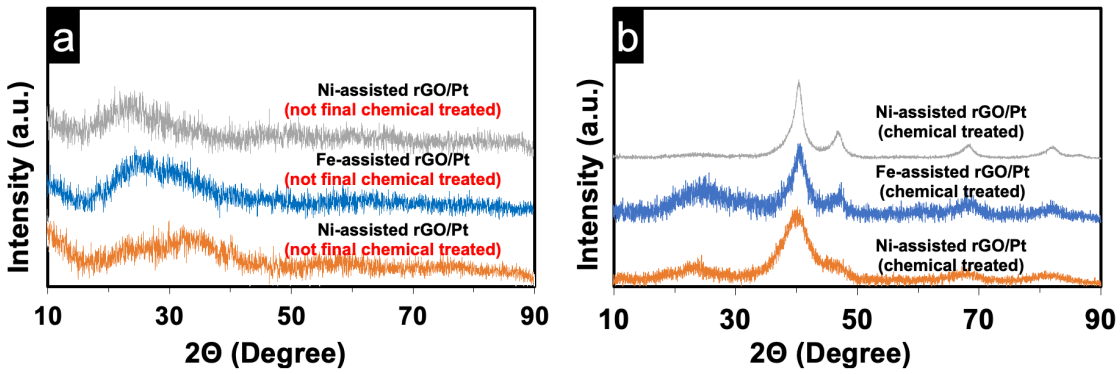

Figure 2.9. X-ray diffractogram of the samples prepared with different transition metal ions assistance, a) before, and b) after chemical treatment with ascorbic acid solution

To evaluate the particle distribution and their morphology, and elemental distribution analysis of Pt on samples, HRTEM with HAADF imaging was performed. The results are demonstrated in Figure 2.9. In the three samples deposited by the three transition metal ions

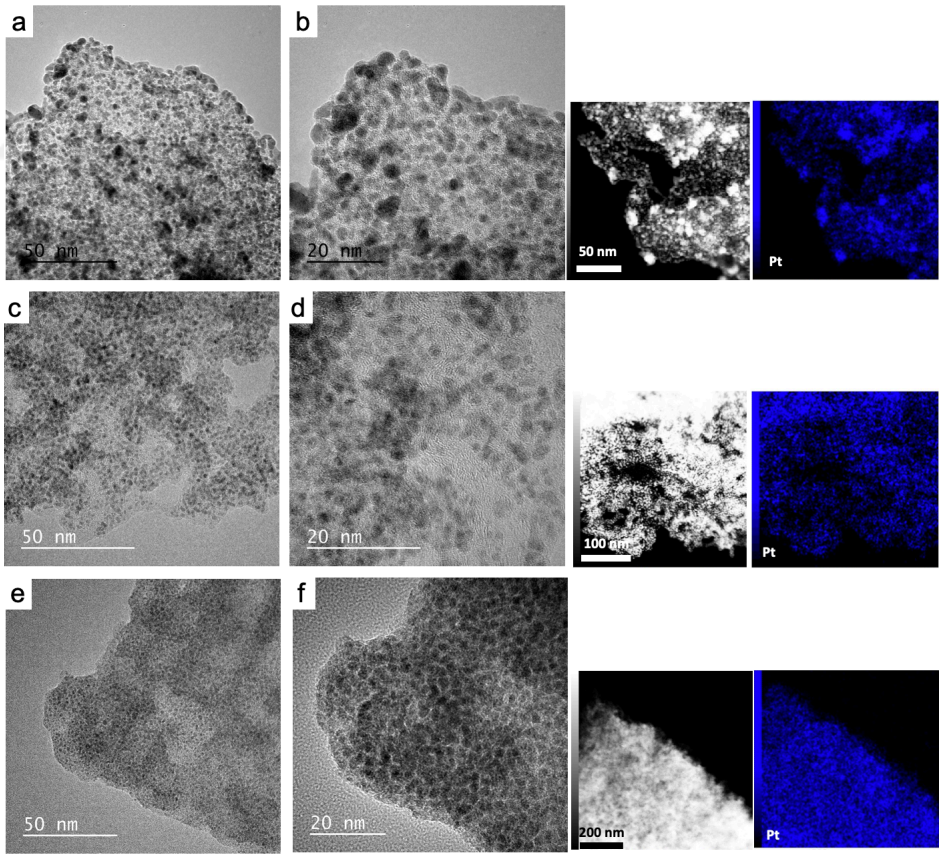

Figure 2.10. TEM micrographs of Pt particles and their morphology on PRGO supports: a and b) Pt /PRGO synthesized with Co^{2+} assistance, c,d) Pt /PRGO synthesized with Fe^{2+}

assistance, and e, f) Pt /PRGO synthesized with Ni^{2+} assistance. The elemental distribution of Pt is also displayed for each sample.

Pt particles were deposited because of photocatalytic reduction and the Co^{X+}, Ni^{X+} or Fe^{X+} might be deposited as a result of photocatalytic oxidation. Pt distributions were different in the three samples. In the case of using Co^{2+}, more agglomeration of the Pt was seen. If one put the figures in order of the highly uniform distribution of Pt to more agglomeration of Pt, the usage of Ni^{2+} as the additive or hole scavenger caused the best uniform deposition of Pt. Further modification of the samples by ascorbic acid solution causes reduction of cobalt oxide particles and elimination of them from the samples. This was also confirmed by compositional analysis which has been discussed in the following sections.

In Figure 2.10, schematic steps from Pt^{4+} adsorption to the Pt agglomeration or crystallite formation are demonstrated. In the synthesis process, t_{on} was the time interval during which the excitation of electrons to CB and consequently nucleation and growth of Pt atoms took place. It has been claimed that Pt^{4+} is reduced to Pt^0 in two steps: 1) Pt^{4+} to Pt^{2+}, and 2) Pt^{2+} to Pt^0 [58]. If the oxidation of the adjacent hole scavenging agents, methanol or Co^{2+} or other metal ions (Ni^{2+} or Fe^{2+}), is kinetically fast enough, more excited electrons will be available, and t_{on} will be more efficiently spent on accomplishing the two steps of Pt reduction and bigger particles formation. Figure 2.10 schematically demonstrates that in the case of kinetically favorable conditions such as a Co^{2+}, at each cycle of suspension circulation, t_{on} might be sufficient for settlement and growth of metallic Pt at thermodynamically favorable spots. We will see in the following sections that this difference will affect the electrocatalytic characteristics.

The oxidation rate of hole scavengers may depend on their adsorption mechanism, availability (concentration), and redox potential or kinetics [59,60]. One of the significant factors in studying GO behavior in aqueous solutions which contain metal ions or alcohol molecules is GO's interaction with its surrounding species. Based on a study conducted by Wang et al. [55], metal ions, M^+, could be attracted to negatively charged GO sheets and cause partial neutralization of GO.

$$[GO]^{-x} + xM^+ \rightarrow GOM_x \qquad 2.2$$

However, methanol and water molecule tend to form hydrogen bonds with GO functional groups. The probability of forming a hydrogen bond between water molecules and GO is

much more than forming the bond between methanol molecule and GO, especially when the GO has already been synthesized and stored in aqueous solutions and methanol is added to the suspension afterward [56], similar to the current study. As a result, cobalt ions are more accessible for oxidation on the surface of PRGO and reducing the holes.

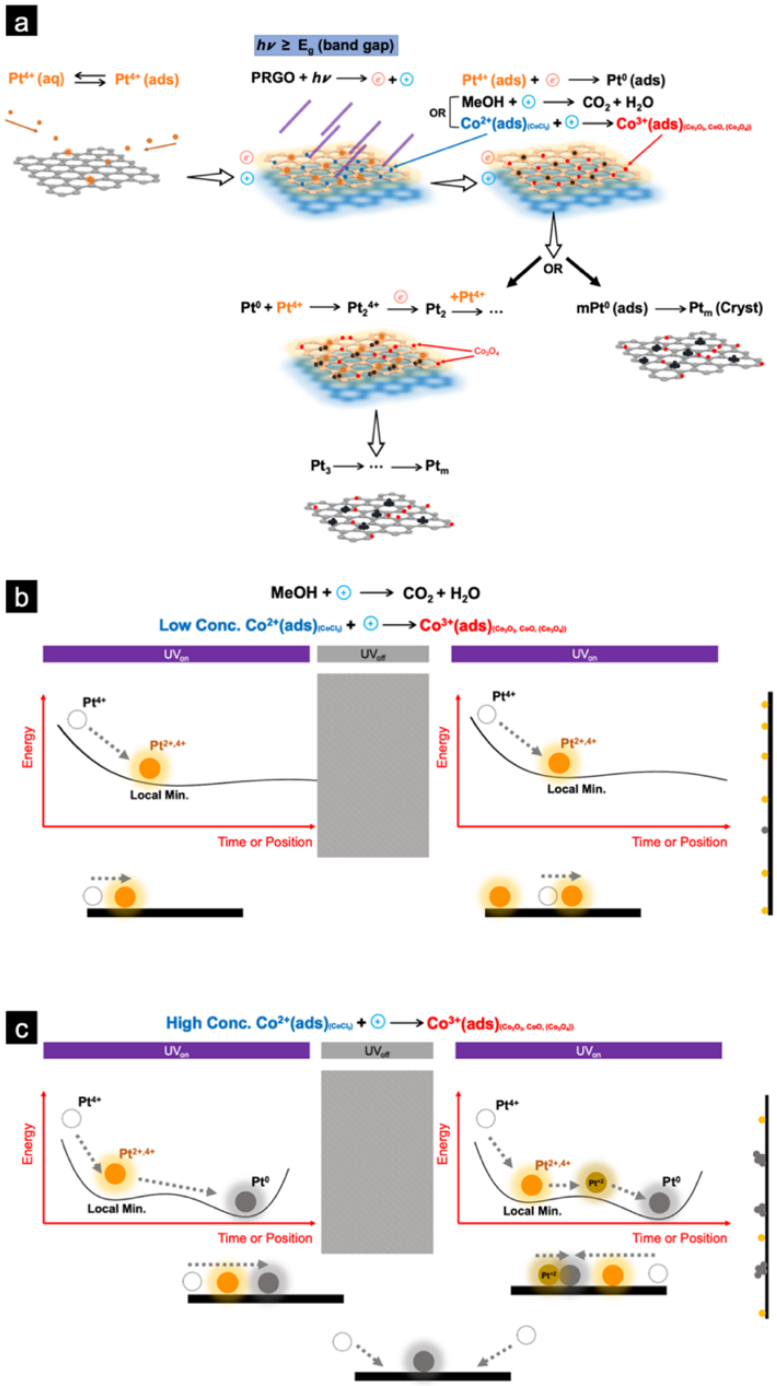

Figure 2.11. a) Alternative mechanisms for Pt deposition with oxidation of different types of hole scavengers, b, and c) nucleation mechanism of Pt particles prepared by b) methanol or low concentration of Co^{2+}, and c) high concentration of Co^{2+}, as hole scavenger(s).

more accessible for oxidation on the surface of PRGO and reducing the holes. Also, Co^{2+}s, by being attracted to specific spots on the PRGO surface (Figure 2.11), prevent the deposition of Pt particles at those spots which could affect electrons transfer pathways, later, during the electrocatalytic performance. Figure 2.11c shows the change of zeta potential value on PRGO particles in solutions with different types of hole scavengers. All these factors could have a determining effect on the oxidation kinetic of hole scavengers and hence the mechanism, position of deposition, and oxidation state of reduced Pt^{X+} particles. The cobalt ion is an example, i.e., this hypothesis could be applied for the other metal ions as well (Ni^{2+} and Fe^{2+}). The zeta potential measurement of the all samples are also given in the Figure 2.11c.

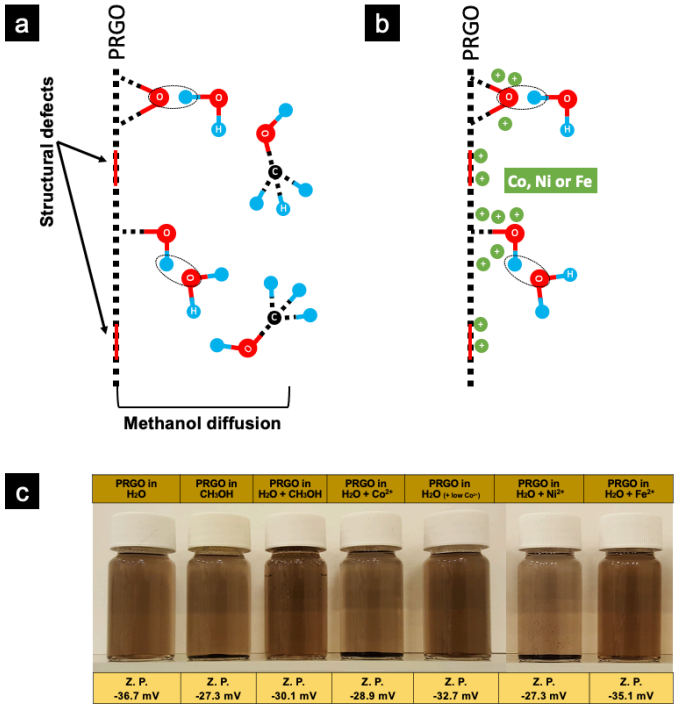

Figure 2.12. The position of hole scavengers, a) CH_3OH and b) Co^{2+}, Ni^{2+} or Fe^{2+}, in an aqueous suspension containing PRGO, and c) Zeta potential value of PRGO in aqueous and non-aqueous (methanol) suspensions with the probability of PRGO precipitation after 24 hours.

To assess the effect of transition metal oxide s possible deposition or interaction on the Pt deposition and consequently D and G vibration modes of the graphene-based materials, Raman spectroscopy was conducted (Figure 2.12). Carbon atoms are in a locked structure in the hexagonal structure of the perfect graphene. Because of this structure, the breathing

vibrational mode is forbidden, and the D band could not be seen in Raman spectra. Defects in the carbon lattice, vacancies, oxygen functional groups, or deposited particles e.g., change the sp^2 structure to sp^3, and the intensity of the D band increases [61]. In completely oxidized graphene, all carbon atoms are sp^3 hybridized and the D band disappears again. There is a maximum in the D band intensity when the level of deficiencies increases. In Figure 2.12, the highest value of I_D/I_G (= 0.89) can be seen (letter "I" represents the intensity) for rGO-Pt prepared by the Ni ions as the hole scavenger, before the chemical treatment with ascorbic acid solution (Figure 2.12 a and c vs, figure 2.12b and d). By comparing Figure 2.12 and TEM images in Figure 2.9, the highest I_D/I_G belonged to the sample with more even distribution of Pt particles with less agglomeration. This result highlights the hypothesis that small and well distribution of Pt particles might further distort the sp^2 structure to sp^3 structure.

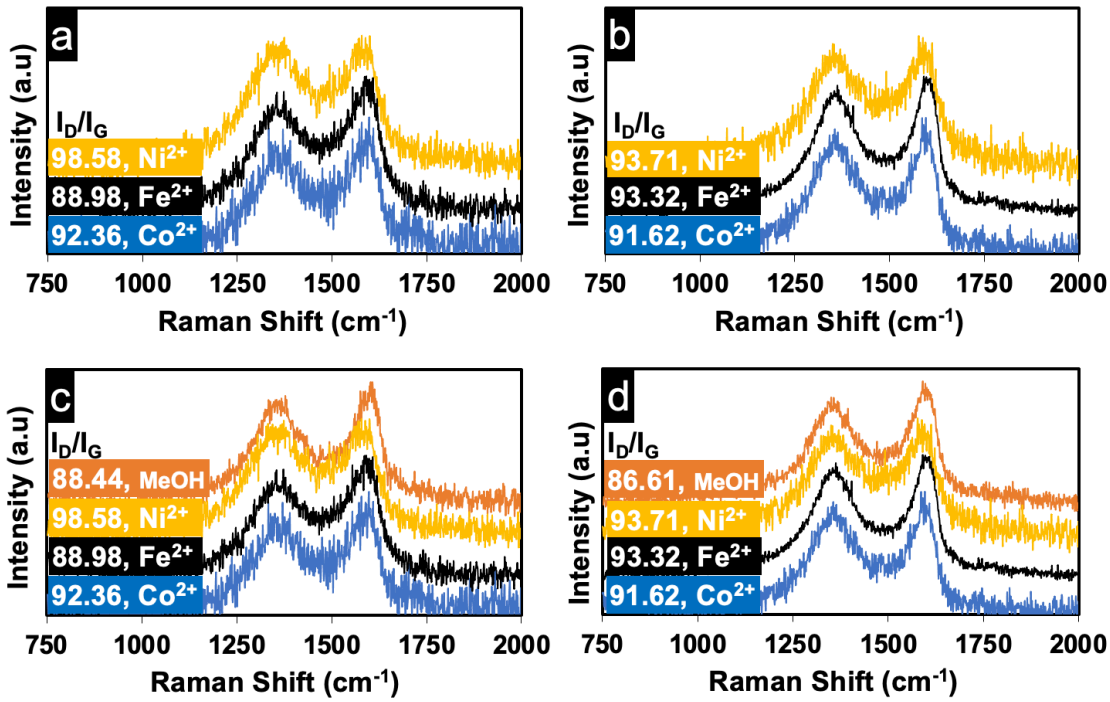

Figure 2.13. Raman spectra of rGO in different samples prepared with different types of hole scavengers. b and d are for samples with final chemical reduction with ascorbic acid solution. c and d are for comparing the samples with the control sample (methanol hole scavenger.

The XPS method was employed to gain more detailed information about the chemical structure of the electrocatalysts. Figure 2.13 illustrates the binding energy of platinum, which comes from its different oxidation states, carbon hybridization states, and oxygen

functional groups. The XPS spectra of Pt 4f demonstrated a doublet peak at 71.8 eV and 75.2 eV. Comparing Figure 2.13c to figures 2.13e and 2.13a revealed that the binding energy of Pt has shown more contribution from Pt^{2+} and Pt^{4+} states (shifting the binding energy a little to higher values).

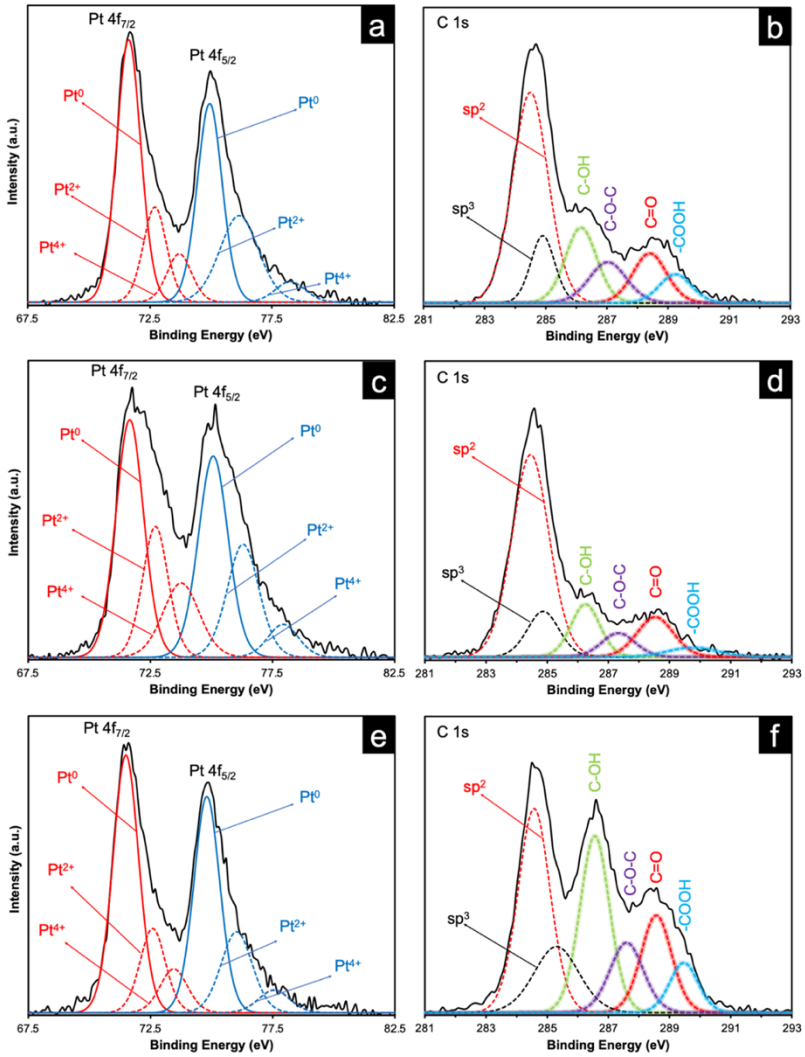

Figure 2.14. X-ray photoelectron spectroscopy (XPS) spectrum of Pt 4f and C 1s for: a and b) Pt/rGO deposited with methanol, c and d) Pt/rGO deposited with low concentration of Co^{2+}, and e and f) Pt/rGO deposited with the Co^{2+}.

Figure 2.13c was gained from the sample with the lower concentration of Co^{2+}, hence a lower rate of hole consumption and a consequently lower rate of Pt reduction. Not accomplishing the Pt^{4+} reduction to Pt^0 or a lower amount of Pt^0 nucleation and growth would lead to smaller Pt particles which could form more Pt oxide states rather than the metallic state [62]. In other words, comparing the XPS data and the TEM figures could

enable one to conclude that methanol or the high concentration of Co^{2+} caused the t_{on} in each UV pulse to be enough for Pt nucleation and growth. Figures 2.13a-f were for samples that were post-treated with the ascorbic acid solution. In Figure 2.13f and comparing it to Figures 2.13d and 2.13b, which were the deconvolution of the C 1s from the graphene-based supports, showed a relative increase in the binding energy of carbon by shifting to the right, showing a more contribution of oxygen functional groups including hydroxides (C-OH), epoxy (C-O-C) and carbonyl (-COOH), and carboxyl (C=O). Figure 2.13f and comparing it with Figure 2.14 illustrated that the chemical reduction of the cobalt oxide with ascorbic acid has left the carbon structure under a higher effect of the functional groups. In other words, by evaluating Figure 2.14, cobalt has been deposited on the samples mostly in Co_3O_4 form and the disappearance of cobalt element after the ascorbic acid reduction has shifted the binding energy of electrons of carbon atoms to higher values. (Figure 2.13f).

2.4.3. Electrocatalytic activities

CV tests were performed to determine the number of active sites for hydrogen oxidation reaction, HOR, (Figure 2.15a). In the previous studies, results have demonstrated a very high deposition efficiency and stability of Pt ions by the current method [42, 43]. Based on those results, the ECSA and ORR performance were calculated with respect to 20 wt.% Pt loading which gave the minimum value of the performance and highlight the potential application of this method. The most promising electrochemical activity was for the sample prepared with Co^{2+}, with the ECSA value of 191 $m^2.g^{-1}$. The ECSA values for the other two samples were 141 $m^2.g^{-1}$ and 127 for the ones prepared with Fe^{+2} and Ni^{+2}, respectively. The ECSA values were 152 $m^2.g^{-1}$ for the one that was prepared by methanol and 46 $m^2.g^{-1}$ for the one that was prepared by a low concentration of Co^{2+}.

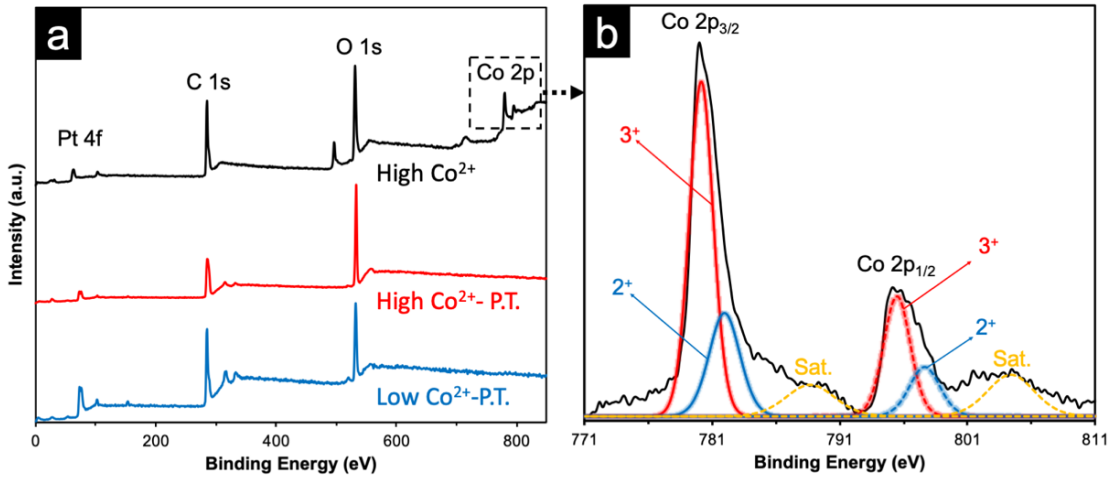

Figure 2.15. a) Survey XPS spectrum of two post-treated (P.T., chemically reduced with ascorbic acid solution) samples prepared with Co^{2+} ions and one without post-treatment, and b) XPS spectrum of Co 2p of the sample without post-treatment.

The lower electrocatalytic activity for the latter samples could be because of the existence of more oxidized states of Pt or less functional-group-caused distortion in carbon C 1s structure (Figure 2.13). The other reason for the lower electrocatalytic activity of the last two samples might be the Pt deposition spots, which were not energetically favorable. It has been reported that the Pt deposition on carbon support can be controlled by thermodynamic or kinetic factors, each of them could affect the final product electrocatalytic activity. Parameters such as Pt precursors, reducing agents, additives, and reaction temperature and time could modulate the kinetic of Pt reduction from the ionic states [63].

To evaluate the ORR performance of the synthesized samples, LSV tests by employing rotating disk electrodes (RDE) at the rotation speed of 1600 rpm were conducted. From Figure 2.16, a mixed kinetic-diffusion controlled region appeared from 0.8 V to 0.95 V.

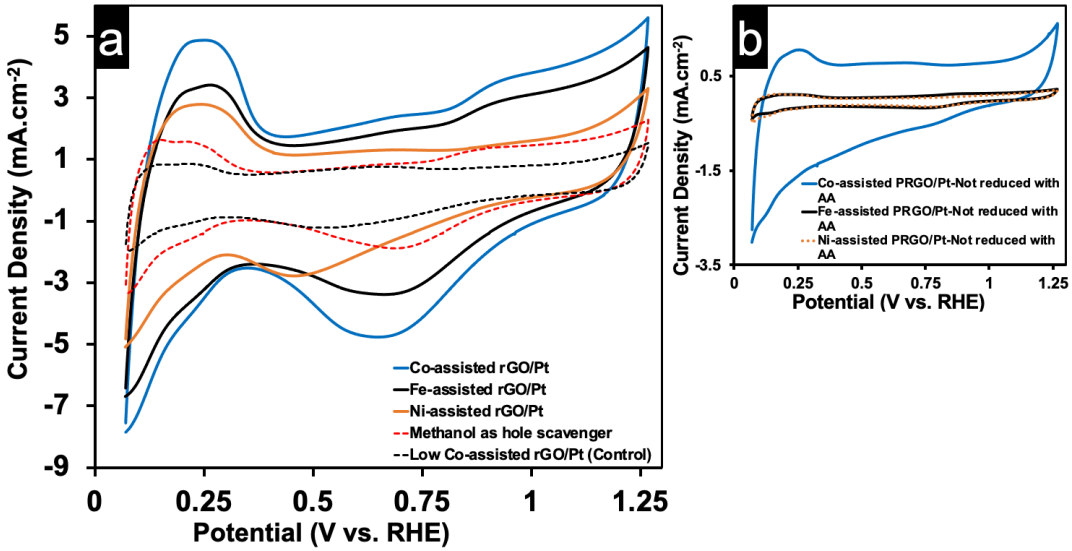

Figure 2.16. a) Cyclic voltammetry of a) rGO/Pt prepared with methanol, Fe^{2+}, Ni^{2+} and two concentration of Co^{2+}after reduction with ascorbic acid, b) rGO/Pt prepared with Fe^{2+}, Ni^{2+} and Co^{2+} before reduction with ascorbic acid

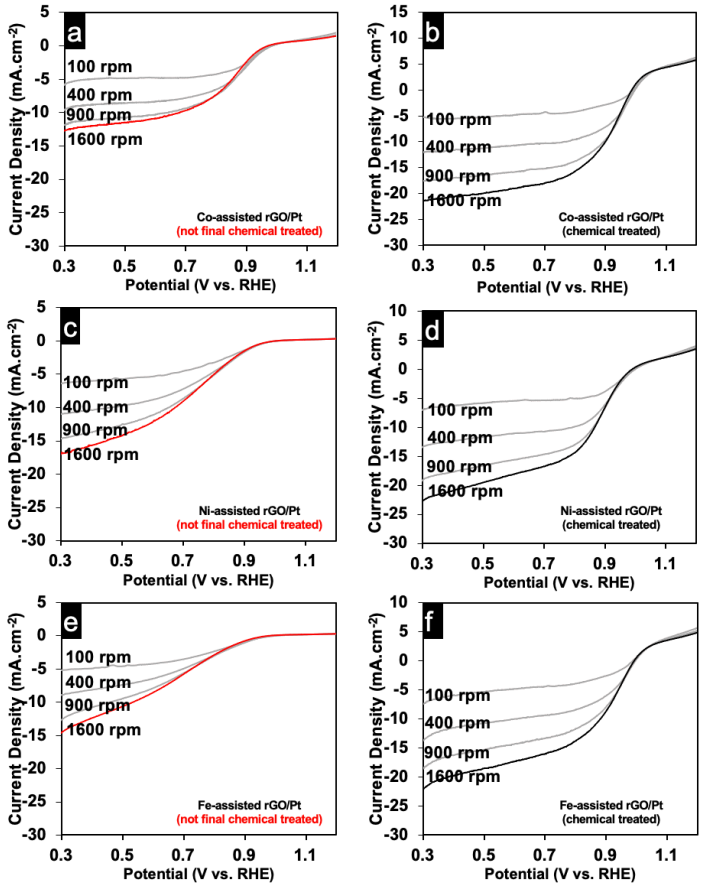

Figure 2.17. linear sweep voltammetry of the transition metal assisted synthesized rGO/Pt a,c,d) before reduction by, and b,d,f) after reduction with ascorbic acid.

Therefore, to calculate the mass activity value the potential of 0.9 V was chosen. By evaluating the three samples the poor performance of the two samples synthesized by low Co^{2+} or methanol could be observed. Based on the sensitive nature of ORR and its high dependency on the structure of the catalyst and support (see XPS and TEM results) figure 2.16 demonstrated a higher performance for ORR behavior of graphene/Pt electrocatalyst prepared with the high concentration of Co^{2+} as the hole scavenger (0.49 $A.mg^{-1}$). The summary of the electrochemical performances is presented in Table 2.3.

Table 2.3. ECSA and mass activity of Pt/rGO electrocatalysts synthesized with different hole scavenging procedures.

Synthesis procedure	ECSA ($m^2.g^{-1}_{Pt}$)	mass activity at 0.9 V ($A.mg^{-1}_{Pt}$)
Prepared with Co^{2+}	191	0.49
Prepared with Fe^{2+}	141	0.39
Prepared with Ni^{2+}	127	0.25
Prepared with a low concentration of Co^{2+}	46	0.05
Prepared with methanol (CH3OH)	152	0.08

2.4.4. Conclusions

This experimental section has investigated the photocatalytic deposition of Pt nanoparticles on PRGO supports, by using two types of hole scavengers (Transition metal ions, Co^{2+}, Ni^{2+}or Fe^{2+}, or methanol), and the effect of the hole scavenging approach on the electrocatalytic performance of the synthesized electrocatalysts was analyzed. This study has presented a novel procedure for synthesizing metal/metal oxide electrocatalysts on graphene-based supports. Here, the type of catalyst support which was different from other types of photocatalysts based on its interactions with the environment, the synthesis procedure by using a pulsed UV illumination, the focus on the type of hole scavengers

(metal ions or organic molecules) and their interactions with the support, and finally the whole procedure's effect on the deposition mechanism of Pt particles and their electrocatalytic activity may highlight the role of the chosen topic(s) in electrocatalysts synthesis. The impact of this study lies in the conclusion that uniform and even distribution of small Pt nanoparticles on graphene-based materials were not always the sign of higher electrocatalytic activities. Yet, it was the Pt complex adsorption, $Pt^{4+} \rightarrow Pt^{2+} \rightarrow Pt^{0}$ reduction progress, and Pt's final oxidation state and its deposition spot that determined the performance of Pt/graphene-based electrocatalysts. Based on the higher oxidation rate of Co^{2+} (the hole scavenger) and the additional electrostatic interaction between Co^{2+} ions and PRGO's negatively charged surface, we were able to elevate the Pt growth rate in each UV on-time period. The different rate of oxidation for different additives (hole scavengers) was not only because of their different redox potential but also because of their different interactions with, and different local concentrations near, the graphene sheets and surrounding water molecules. More reduction of Pt^{4+} to Pt^{0} during the limited UV on-time, caused a higher growth of Pt on PRGO with higher ECSA value and ORR performance, albeit with a coarser and agglomerated structure. On the other hand, oxidation of methanol or low concentration of Co^{2+} did not provide an enough Pt reduction rate in each on-time period and made the adsorbed Pt^{4+} form new nuclei which meant smaller Pt with mostly Pt^{2+} or Pt^{4+} states and lower electrochemical performance. One of the important parts of the synthesis was modifying the PRGO structure with an ascorbic acid solution which also caused the reduction and elimination of transition metal oxides and leaving the rGO/Pt samples with the mentioned properties. This final step differentiated the current study from the similar ones trying to synthesize bimetallic of PtXs as PEMFCs electrocatalysts. Here, the second metal precursor played a significant role in synthesizing procedure of highly active Pt particles, and almost didn't have a role in the final products' catalytic activity.

CHAPTER 3. Computational Methods in Studying Pt/Graphene Electrocatalysts: Artificial Neural Network Modelling and Density Functional Theory Calculation

3.1. Introduction

The third section of the thesis focuses on the computational aspects of designing graphene-Pt-based PEM fuel cell electrocatalysts prepared with the proposed photocatalytic deposition method. Here, the mechanism of deposition and also the photocatalytic reaction are not the subject of the study, yet it was the final properties of the electrocatalysts which were tried to be modelled with neural network method and DFT calculation. At the first part, the procedure to prepare the necessary samples will be discussed. One of the important steps of applying machine learning methods for modeling a data set is the size of the data set large enough to train the algorithm to be able to predict the unknown results. Because of the potential of the proposed method in synthesizing a wide range of Pt-based electrocatalysts by just manipulating the setup parameters, and not the chemicals, the idea of predicting the final electrocatalytic activities of PRGO/Pt samples with machine learning method seemed to be a promising approach in autonomous synthesis procedures. By confirming the successful modelling of the samples, this synthesis procedure could be equipped with a fast in-situ characterization technique and become a prototype of an autonomous synthesis technique which could continuously update its UV illumination parameters and produce the samples with the required properties.

The second part of this section deals with the DFT calculation and finding the equilibrium structure of Pt/graphene and Pt/Graphene-oxide composites plus some H_2 molecules in a vacuumed environment on top of them. For this purpose, the Quantum-Espresso code were utilized to perform the “relax” calculation on hypothetical designed samples to see:

1. The relax position of the Pt atoms in a Pt crystal placed on a graphene/graphene oxide plane
2. The adsorption behavior of H_2 molecules on Pt/G and Pt/GO samples (to see if the oxygen functional groups on graphene plane facilitate or impede the adsorption of hydrogen on Pt crystals)
3. The structural change of graphene plane by putting oxygen groups on its different spots (e.g., wrinkling).

3.2. Artificial Neural Network modelling of Pt/Graphenes' cyclic voltammtery

3.2.1. Sample preparation for training the NN algorithm

As it was mentioned in the previous chapter, the application of the pulsed-UV illumination could result in electrocatalysts with a range of activity and cyclic voltammetry graph. CV test is one of the electrochemical methods by which the electrocatalytic activities of samples in different environment could be measured. In this study we used an acidic environment to study the ability of the synthesized samples in oxidation and reduction of hydrogen. The medium was purged with nitrogen gas before the electrochemical tests to make sure that the dissolved oxygen does not interfere with electrochemical reactions.

3.2.2. Input values (features)

In the second chapter, four samples had been studied to measure the effect of the UV-on and -off time on the structural and electrochemical performance of the samples. To select the feature value for training the neural network algorithm we selected two more input parameter that could also have effects on the final properties (the CV graph). One of them is the total time of the synthesis, t_{tot}, which determines the total time that the suspension is purged with the N_2 that could cause the exit of the volatile hole scavenger, and the second parameter is the duty cycle, which determines the ratio of UV-on over the total time of one circle of the suspension through the setup's pipes. To have the enough number of samples for training the algorithm 39 different samples were synthesized with different values of the "time "intervals. Table 3.1, demonstrates all the samples with their specific parameters.

3.2.3. Output or target values (labels)

Figure 3.1 shows the general CV graph of Pt/PRGO electrocatalyst prepared with the pulsed-UV photocatalytic deposition. Note that none of the samples showed a high activity before the chemical treatment with ascorbic acid solution. In fact, this chapter focuses on the prediction of the CV graph of a Pt/PRGO sample produced by pulsed-UV photocatalytic deposition.

As it can be seen, figure 3.1, the CV graph has different section which relate to hydrogen redox reaction, platinum oxide redox reaction or water redox reaction. If we sketch the current densities versus time, we could have the range of the current density over one

cycle of the cyclic voltammetry test. We could take two approaches: one, select the maximum current density of each section and introduce them as the outputs, or two, take all current densities as the matrix of the outputs. To reduce the time of the calculation, we first used the first approach. The figure 3.1 demonstrates the output selection for CV graph.

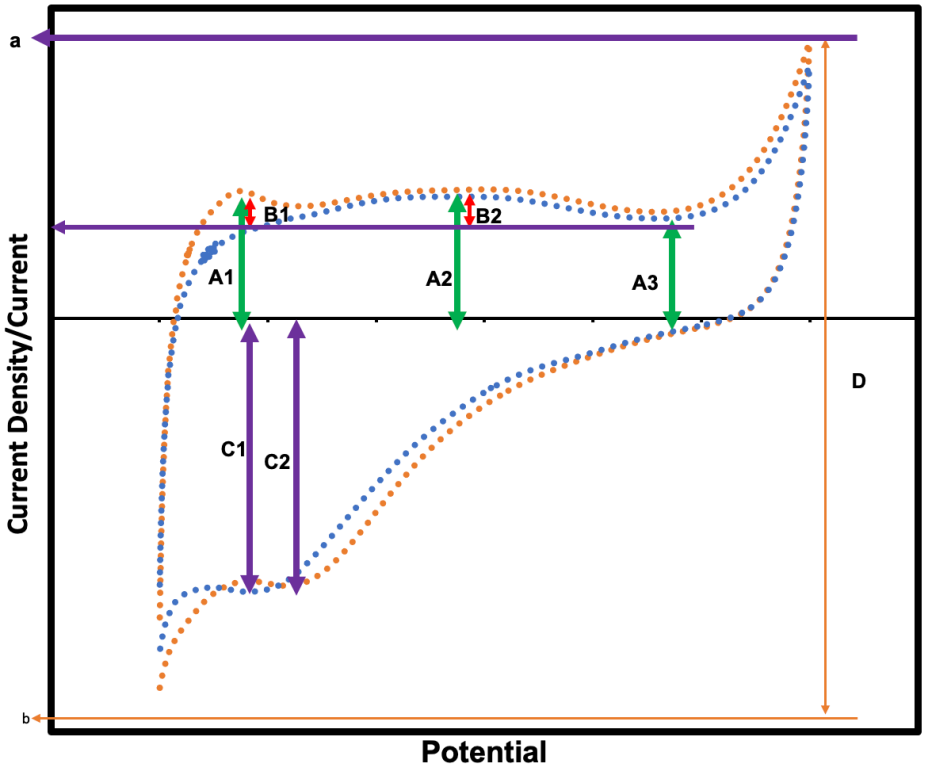

Figure 3.1. The output (label) selection form cyclic voltammetry graph.

3.2.4. Artificial Neural Network (ANN) toolbox of MATLAB

In this study the ANN toolbox of MATLAB software was utilized to create the neural network algorithm for training and modelling the CV data (Figure 3.2).

Table 3.1: Inputs (features) and outputs (labels) values for 39 synthesized samples, with different UV-on and -off time intervals.

Sample #	Sample ID	Tube	Volume (mL)	UV-On (S)	UV-Off (S)	Duty Cycle (%)	Total time (min)	A1	A2	A3	a	b	B1	B2	D
1	100uv270	100	270	1.5	12.0	11.1	120	5.11E-04	6.05E-04	5.06E-04	0.001331	-0.001639	4.90E-06	9.94E-05	0.00297
2	100uv310	100	310	1.5	13.8	9.8	138	3.96E-04	4.78E-04	3.90E-04	0.001014	-0.001342	6.10E-06	8.79E-05	0.002356
3	100uv350	100	350	1.5	15.6	8.8	156	3.58E-04	4.18E-04	3.63E-04	0.0009812	-0.001352	-4.20E-06	5.55E-05	0.0023332
4	100uv390	100	390	1.5	17.3	8.0	173	4.29E-04	4.94E-04	4.29E-04	0.001181	-0.001457	-4.00E-07	6.52E-05	0.002638
5	100uv430	100	430	1.5	19.1	7.3	191	4.54E-04	5.22E-04	4.57E-04	0.001209	-0.001485	-3.20E-06	6.46E-05	0.002694
6	100uv470	100	470	1.5	20.9	6.7	209	2.95E-04	3.48E-04	3.12E-04	0.0008611	-0.001384	-1.66E-05	3.66E-05	0.0022451
7	100uv510	100	510	1.5	22.7	6.2	227	3.53E-04	4.04E-04	3.39E-04	0.0009657	-0.001279	1.38E-05	6.50E-05	0.0022447
8	100uv550	100	550	1.5	24.4	5.8	244	5.50E-04	6.36E-04	5.22E-04	0.00141	-0.001829	2.79E-05	1.14E-04	0.003239
9	100uv590	100	590	1.5	26.2	5.4	262	4.54E-04	5.13E-04	1.17E-03	1.18E-03	-1.69E-03	-7.20E-04	-6.61E-04	0.002867
10	100uv630	100	630	1.5	28.0	5.1	280	6.83E-04	6.77E-04	1.44E-03	1.45E-03	-1.60E-03	-7.57E-04	-7.63E-04	0.00305
11	100uv670	100	670	1.5	29.8	4.8	298	3.99E-04	4.42E-04	1.11E-03	1.12E-03	-1.58E-03	-7.11E-04	-6.68E-04	0.0027
12	100uv710	100	710	1.5	31.6	4.5	316	6.04E-04	6.09E-04	5.67E-04	0.001412	-0.001766	3.76E-05	4.21E-05	0.003178
13	100uv750	100	750	1.5	33.3	4.3	333	4.28E-04	4.63E-04	1.15E-03	1.16E-03	-1.62E-03	-7.22E-04	-6.87E-04	0.00278
14	100uv790	100	790	1.5	35.1	4.1	351	3.89E-04	4.49E-04	3.93E-04	0.001026	-0.001369	-3.70E-06	5.61E-05	0.002395
15	100uv830	100	830	1.5	36.9	3.9	369	5.94E-04	6.68E-04	1.47E-03	1.48E-03	-1.71E-03	-8.76E-04	-8.02E-04	0.00319
16	100uv870	100	870	1.5	38.7	3.7	387	7.49E-04	7.22E-04	6.13E-04	0.001662	-0.002078	1.36E-04	1.09E-04	0.00374
17	100uv910	100	910	1.5	40.4	3.6	404	4.47E-04	5.14E-04	1.19E-03	1.20E-03	-1.53E-03	-7.45E-04	-6.78E-04	0.00273
18	100uv950	100	950	1.5	42.2	3.4	422	5.59E-04	5.16E-04	4.63E-04	0.001257	-0.001759	9.57E-05	5.27E-05	0.003016
19	100uv1070	100	1070	1.5	47.6	3.1	476	5.13E-04	5.91E-04	1.37E-03	1.38E-03	-1.91E-03	-8.57E-04	-7.80E-04	0.003283

20	100uv1110	100	1110	1.5	49.3	3.0	493	4.05E-04	4.50E-04	1.07E-03	1.07E-03	-1.46E-03	-6.62E-04	-6.17E-04	0.002537
21	100uv1150	100	1150	1.5	51.1	2.9	511	7.08E-04	6.53E-04	5.48E-04	0.001445	-0.001788	1.61E-04	1.06E-04	0.003233
22	100uv1270	100	1270	1.5	56.4	2.6	564	7.12E-04	6.98E-04	1.51E-03	1.52E-03	-1.92E-03	-7.98E-04	-8.12E-04	0.00344
23	100uv1350	100	1350	1.5	60.0	2.4	600	5.72E-04	5.44E-04	5.08E-04	0.001323	-0.001978	6.32E-05	3.59E-05	0.003301
24	50uv270	50	270	0.75	12.0	5.9	240	2.02E-04	2.34E-04	2.08E-04	0.0006303	-0.001261	-6.00E-06	2.65E-05	0.0018913
25	50uv290	50	290	0.75	12.9	5.5	258	1.76E-04	2.12E-04	1.84E-04	5.38E-04	-9.37E-04	-8.70E-06	2.76E-05	0.0014748
26	50uv310	50	310	0.75	13.8	5.2	276	4.74E-04	4.40E-04	3.85E-04	0.001123	-0.001883	8.90E-05	5.56E-05	0.003006
27	50uv330	50	330	0.75	14.7	4.9	293	1.24E-04	1.59E-04	1.40E-04	4.01E-04	-6.26E-04	-1.60E-05	1.93E-05	0.0010273
28	50uv350	50	350	0.75	15.6	4.6	311	2.09E-04	2.58E-04	2.20E-04	0.0006671	-0.001294	-1.10E-05	3.74E-05	0.0019611
29	50uv370	50	370	0.75	16.4	4.4	329	1.94E-04	2.37E-04	2.07E-04	6.30E-04	-1.10E-03	-1.24E-05	3.05E-05	0.0017286
30	50uv390	50	390	0.75	17.3	4.1	347	2.91E-04	3.36E-04	2.97E-04	0.000871	-0.001442	-6.10E-06	3.84E-05	0.002313
31	50uv410	50	410	0.75	18.2	4.0	364	2.30E-04	2.66E-04	2.30E-04	6.69E-04	-1.12E-03	-4.00E-07	3.58E-05	0.0017883
32	50uv430	50	430	0.75	19.1	3.8	382	3.21E-04	3.66E-04	3.24E-04	9.19E-04	-1.44E-03	-3.00E-06	4.20E-05	0.002359
33	50uv450	50	450	0.75	20.0	3.6	400	2.29E-04	2.95E-04	2.41E-04	6.86E-04	-1.19E-03	-1.20E-05	5.40E-05	0.001876
34	50uv470	50	470	0.75	20.9	3.5	418	1.40E-04	1.79E-04	1.50E-04	4.30E-04	-7.06E-04	-1.04E-05	2.88E-05	0.0011359
35	50uv490	50	490	0.75	21.8	3.3	436	3.16E-04	3.88E-04	3.16E-04	8.46E-04	-1.28E-03	0.00E+00	7.20E-05	0.002126
36	50uv510	50	510	0.75	22.7	3.2	453	2.06E-04	2.57E-04	2.30E-04	6.93E-04	-1.13E-03	-2.38E-05	2.68E-05	0.0018192
37	50uv570	50	570	0.75	25.3	2.9	507	3.62E-04	4.29E-04	3.51E-04	0.001007	-0.001619	1.09E-05	7.80E-05	0.002626
38	50uv630	50	630	0.75	28.0	2.6	560	2.95E-04	3.54E-04	2.94E-04	8.31E-04	-1.37E-03	1.00E-06	6.00E-05	0.002201
39	50uv670	50	670	0.75	29.8	2.5	596	3.09E-04	3.72E-04	2.96E-04	0.0008432	-0.001342	1.28E-05	7.55E-05	0.0021852

After defining the number nodes and layers and choosing the necessary function and algorithm in the software, the system automatically selects some portion of the samples as the training set, and the rest as the validation and test sets. One could change the percentage of each set. The selection process is in a random manner to avoid producing the bias.

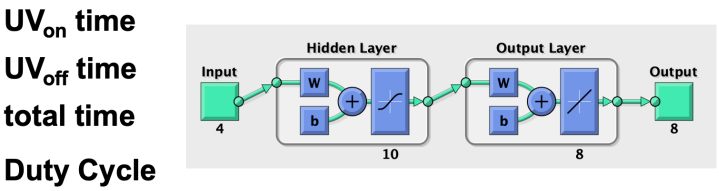

Figure 3.2. The schematic of the MATLAB neural network interface for samples with 4 inputs (the pulse-UV parameters) and 8 outputs (labels) (the CV graph parameters).

3.2.5. Results

Figure 3.3 presents the bias graph for the three categories of the sample features and labels (inputs and outputs). As it can be seen, at least with the current number of the training samples, the predicted amount for the outputs and the real outputs matches well. One of the main ideas in this study was measuring the potential of the current synthesis method in being a prototype of an autonomous materials synthesis method based on semiconductor materials and photocatalytic deposition. This data revealed that by adjusting the precise parameters of pulsed-photocatalytic deposition setup, the final electrochemical properties of the as-synthesized samples (before any chemical modification are predictable. The important factor in this study was choosing the right parameters and normalizing them with respect to each other. For example, studying the synthesis kinetics of different materials which could be produced by photocatalytic methods must be considered while being modelled with machine learning algorithms.

3.3. Density functional theory modelling of H2 adsorption on Pt/graphene Pt/graphene-oxide

3.3.1. Solving the Kohn-Sham equation by matrix-algebra

In following part of this section, we will go through the simulation of the H_2 adsorption on Pt/Graphene and Pt/Graphene-oxide composites. For solving the Kohn-Sham equation

there should be numerical and algebraic procedure to be followed. As a summary of DFT calculations:

It is not possible solve the many-body Schrodinger equation and find the energy of the system because of the complexity. Kohn-Sham equation deals with single-particle equation instead of many-body one. By solving the Kohn-Sham equation, we could find the single particle wave function (ϕ) and then electron density.

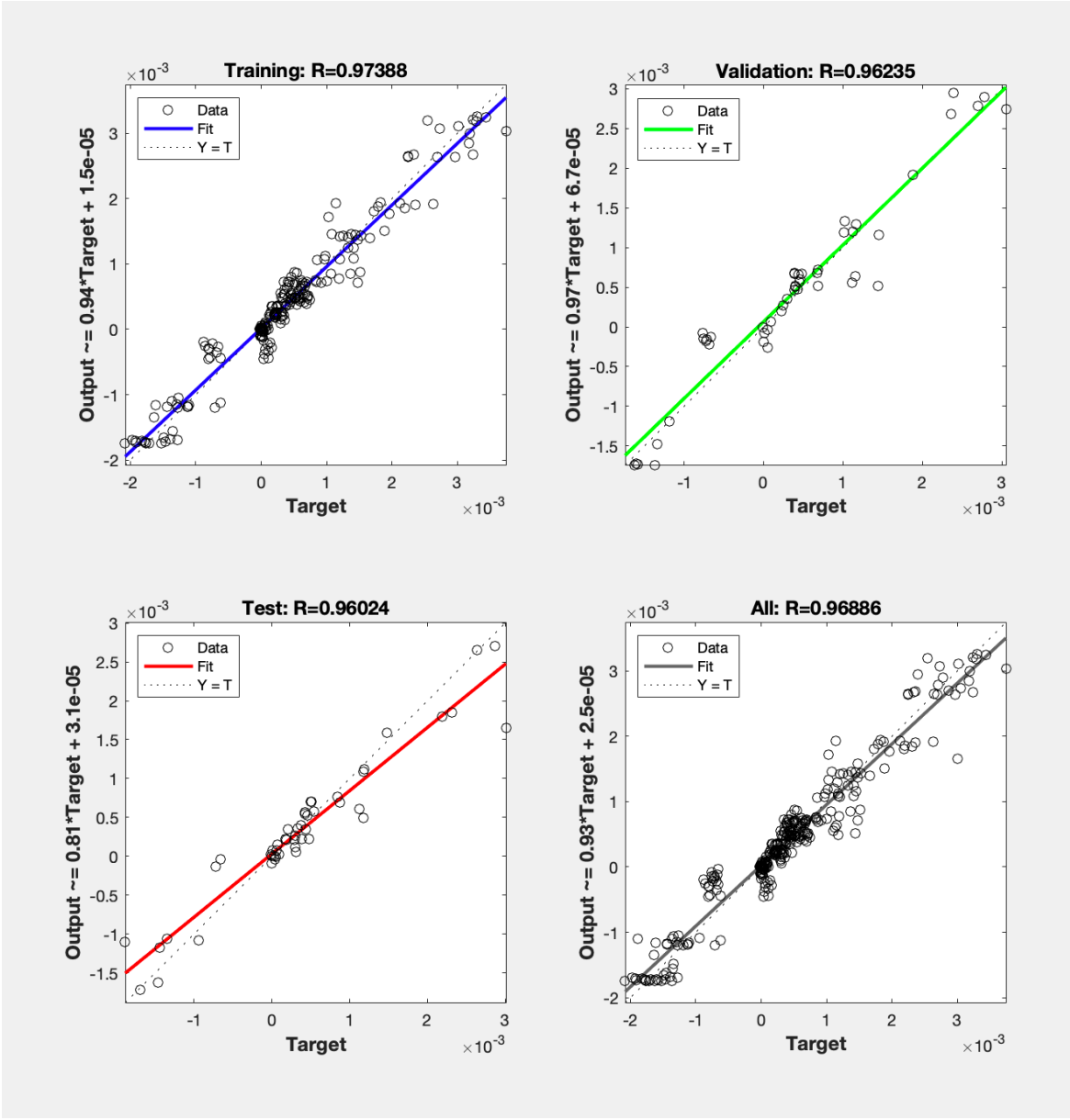

Figure 3.3. The bias graph for three portion of the samples: Training (70% of samples), Validation (15% of samples) and Test (15% percent of samples)

$$\rho(\vec{r}) = \sum_{i}^{N} |\phi(\vec{r})|^2 \qquad 2.3$$

We said that the ground state energy is a functional of ground-state electron density. Summation of all the energy of all individual particles, plus an unknown exchange-correlation energy, could give us the total energy of the system that we were searching for. To solve the Kohn-Sham equation, we could define:

$$\phi_i(\vec{r}) = \sum_{\alpha=i}^{\infty} c_\alpha^i \chi_\alpha^i(\vec{r}) \qquad 2.4$$

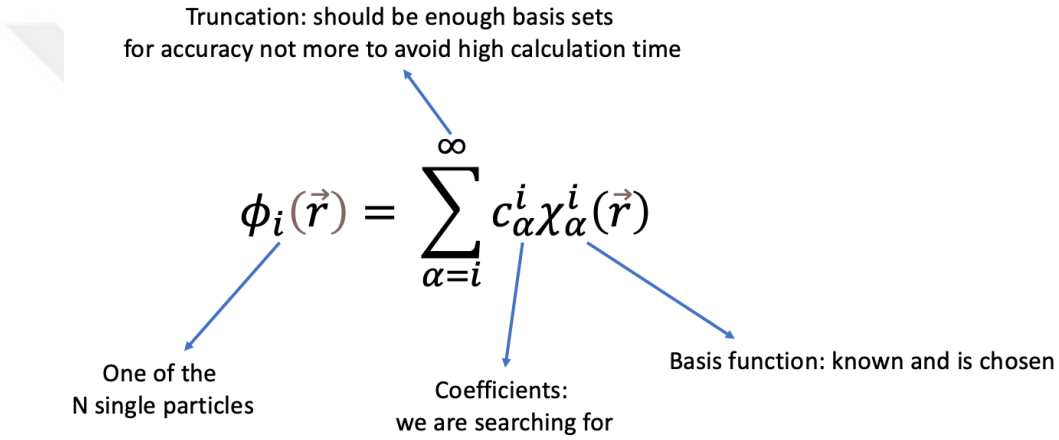

Introducing this basis function and their coefficients transform our KS equation into a matrix-algebra equation:

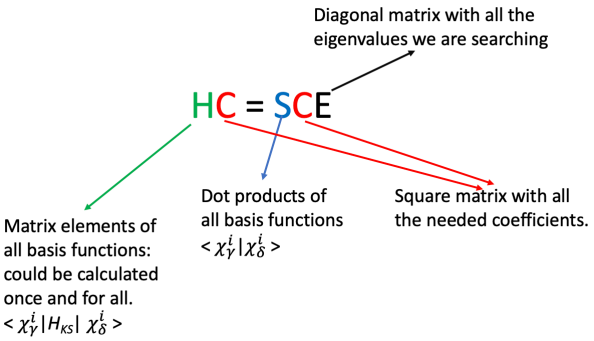

So here we will try to find the C matrix that has the coefficients in it. It means the

unknown part is the C, but to solve this equation we also need H_{KS} that to find it we require the electron density. So here we will remember SCF calculations:

$$\hat{H}_{KS} = \hat{T}_0 + \hat{V}_H + \hat{V}_{ext} + \hat{V}_{XC} \qquad 2.5$$
$$= -\frac{\hbar^2}{2m}\vec{\nabla}_i^2 + \frac{e^2}{4\pi\epsilon_0}\int \frac{\rho(\vec{r}')}{|\vec{r}-\vec{r}'|}d\vec{r}' + \hat{V}_{ext} + \hat{V}_{XC}$$

SCF: In the fellow chart, at the 3rd step to get the ϕ, it uses the matrix equation that we introduced.

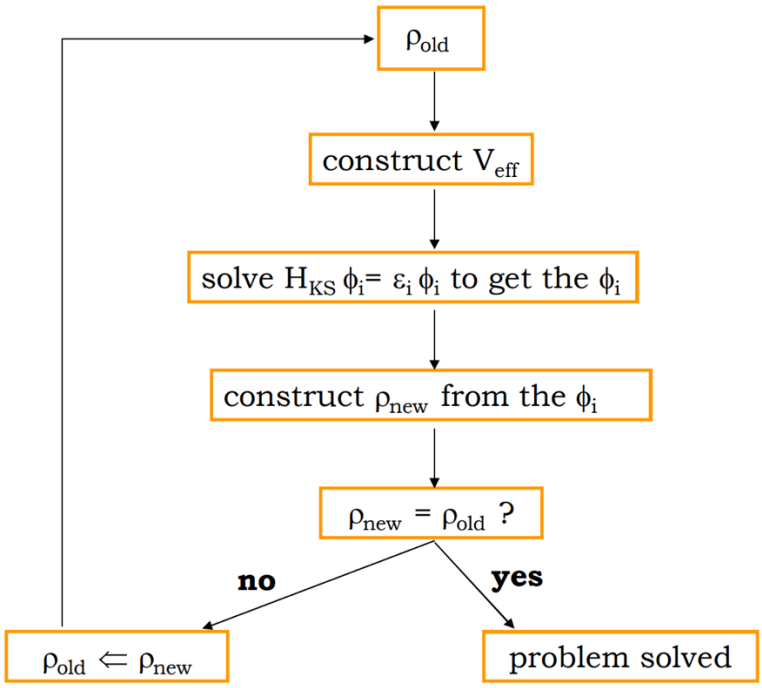

Basis functions (χ) needs to be chosen. By choosing different kinds of basic functions, we will use different computer codes to find the ϕ and after that electron density. Quantum-Espresso uses plane-wave basis function to simulate the ϕ (electron orbital) in companion with pseudopotentials.

3.3.2. Quantum Espresso input files

A detailed explanation for the input file preparation for QE code is provided in the appendix.

3.3.3. Modelling of H_2 adsorption on Pt/graphene Pt/graphene-oxide

3.3.3.1.Preparing the CIF file of Pt/Graphene and Pt/Graphene oxide

As the Pt/Graphene or Pt/Graphene-oxide samples crystal structure are not available in general database, designing it with mixture of the Pt .CIF file and graphene .CIF file is necessary. After downloading the two files, it was decided to rotate the crystal structure of Pt in a direction that the (111) plane faces the H2 molecules. To do so, the VESTA software was utilized for:

- Expansion of the crystal structure of the unit cells to the proper size
- Cutting and rotation of the Pt crustal structure into having the (111) plane perpendicular to Z direction.
- Creating the Pt/graphene structure by mixing the previously created structure of Pt and graphene plane
- Adding oxygen atoms to the graphene plane to have the second sample, (Pt/Graphene-oxide)
- Addition of the H_2 molecules inside the vacuum on top of the structure.
- Finally creating the .CIF file of the created composite to create the QE input file.

3.3.3.2.Samples 3D structure

The final sample has the following structure (figure 3.4) with given position of the atoms, and the cell size.

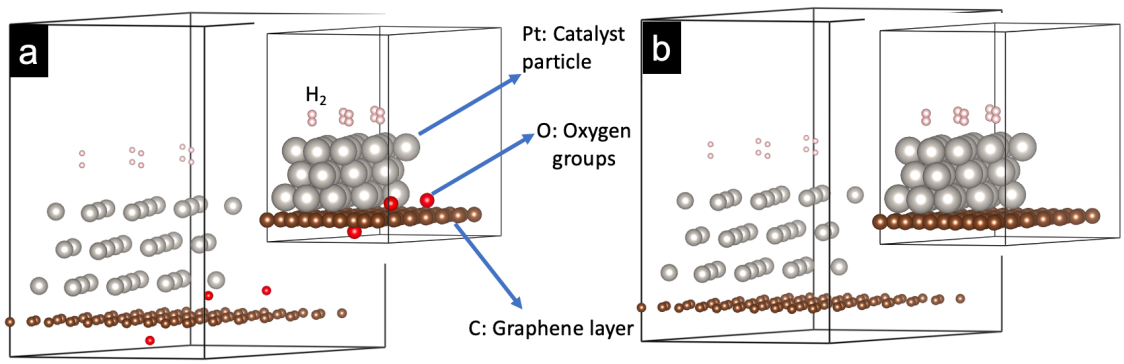

Figure 3.4. The primary designed a) Pt/Graphene oxide and Pt/Graphene samples before DFT calculations and equilibrium coordination.

The input file created with the samples .CIF files are as follows
For the Pt/Graphene:

```
 9  &CONTROL
10    calculation='scf',
11    outdir='/truba/home/nhaghmoradi/DFT_files/Personal/GO_PtH2/outdir333',
12    wfcdir='/truba/home/nhaghmoradi/DFT_files/Personal/GO_PtH2/outdir333',
13    prefix='G_PtH2333',
14    pseudo_dir='/truba/home/nhaghmoradi/DFT_files/Personal/pseudo_dir',
15    verbosity='low',
16    tprnfor=.true.,
17    tstress=.true.,
18    max_seconds= 13800,
19    restart_mode='restart',
20  ! tefield=.FALSE.,
21  ! dipfield=.FALSE.,
22  /
23  &SYSTEM
24    ibrav = 0
25    A =   17.27407
26    nat = 116
27    ntyp = 3
28    tot_charge= 0.0
29    ecutwfc=50,
30    ecutrho=300,
31    input_dft='pbe',
32    occupations='smearing',
33    smearing='mv',
34    degauss=0.005d0,
35  /
36  &ELECTRONS
37    conv_thr=1d-08,
38    mixing_beta=0.7d0,
39    mixing_mode='local-TF',
40  /
41  &IONS !REQUIRED if calculation == 'relax', 'md', 'vc-relax', or 'vc-md' OPTIONAL
42    ion_positions='defult',
43  /
44  CELL_PARAMETERS {alat}
45    1.000000000000000   0.000000000000000   0.000000000000000
46   -0.357142853007840   0.618589566969683   0.000000000000000
47    0.000000000000000   0.000000000000000   1.197461675363034
48  ATOMIC_SPECIES
49    Pt  195.08400   Pt.pbe-n-kjpaw_psl.1.0.0.UPF
50     C   12.01060   C.pbe-n-kjpaw_psl.1.0.0.UPF
51     H    1.00750   H.pbe-kjpaw_psl.1.0.0.UPF
52  ATOMIC_POSITIONS {crystal}
53  Pt   0.838898000000000   0.000000000000000   0.207880000000000
54  Pt   0.932109000000000   0.260990000000000   0.207880000000000
55  Pt   0.279633000000000   0.000000000000000   0.207880000000000
56  Pt   0.372844000000000   0.260990000000000   0.207880000000000
57  Pt   0.559265000000000   0.000000000000000   0.207880000000000
58  Pt   0.652476000000000   0.260990000000000   0.207880000000000
59  Pt   0.093211000000000   0.130495000000000   0.428046000000000
60  Pt   0.186422000000000   0.391486000000000   0.428046000000000
61  Pt   0.372844000000000   0.130495000000000   0.428046000000000
62  Pt   0.466054000000000   0.391486000000000   0.428046000000000
63  Pt   0.652476000000000   0.130495000000000   0.428046000000000
64  Pt   0.745687000000000   0.391486000000000   0.428046000000000
65  Pt   0.186422000000000   0.000000000000000   0.428046000000000
166   H   0.695749000000000   0.392008000000000   0.604302000000000
167   H   0.741288000000000   0.130495000000000   0.568043000000000
168   H   0.741288000000000   0.130495000000000   0.604302000000000
169  K_POINTS {automatic}
170  3 3 3 0 0 0
171
```

For the Pt/Graphene oxide:

```
 9  &CONTROL
10    calculation='scf',
11    outdir='/truba/home/nhaghmoradi/DFT_files/Personal/GO_PtH2/outdir333',
12    wfcdir='/truba/home/nhaghmoradi/DFT_files/Personal/GO_PtH2/outdir333',
13    prefix='GO_PtH2333',
14    pseudo_dir='/truba/home/nhaghmoradi/DFT_files/Personal/pseudo_dir',
15    verbosity='low',
16    tprnfor=.true.,
17    tstress=.true.,
18    max_seconds= 13800,
19    restart_mode='restart',
20  ! tefield=.FALSE.,
21  ! dipfield=.FALSE.,
22  /
23  &SYSTEM
24    ibrav = 0
25    A =   17.27407
26    nat = 119
27    ntyp = 4
28    tot_charge= 0.0
29    ecutwfc=50,
30    ecutrho=300,
31    input_dft='pbe',
32    occupations='smearing',
33    smearing='mv',
34    degauss=0.005d0,
35  /
36  &ELECTRONS
37    conv_thr=1d-08,
38    mixing_beta=0.7d0,
39    mixing_mode='local-TF',
40  /
41  &IONS !REQUIRED if calculation == 'relax', 'md', 'vc-relax', or 'vc-md' OPTIONAL
42    ion_positions='defult',
43  /
44  CELL_PARAMETERS {alat}
45    1.000000000000000   0.000000000000000   0.000000000000000
46   -0.357142853007840   0.618589566969683   0.000000000000000
47    0.000000000000000   0.000000000000000   1.197461675363034
48  ATOMIC_SPECIES
49     O   15.99900   O.pbe-n-kjpaw_psl.1.0.0.UPF
50     H    1.00750   H.pbe-kjpaw_psl.1.0.0.UPF
51    Pt  195.08400   Pt.pbe-n-kjpaw_psl.1.0.0.UPF
52     C   12.01060   C.pbe-n-kjpaw_psl.1.0.0.UPF
53  ATOMIC_POSITIONS {crystal}
54  Pt   0.838898000000000   0.000000000000000   0.207880000000000
55  Pt   0.932109000000000   0.260990000000000   0.207880000000000
56  Pt   0.279633000000000   0.000000000000000   0.207880000000000
57  Pt   0.372844000000000   0.260990000000000   0.207880000000000
58  Pt   0.559265000000000   0.000000000000000   0.207880000000000
170   H   0.695749000000000   0.392008000000000   0.604302000000000
171   H   0.741288000000000   0.130495000000000   0.568043000000000
172   H   0.741288000000000   0.130495000000000   0.604302000000000
173  K_POINTS {automatic}
174  3 3 3 0 0 0
175
176
```

3.3.3.3.Optimizing the K-mesh, ecutwfc and ecutrho

Figure 3.5 shows the variation of hydrostatic pressure value versus the different parameters. At first the K-mesh is being optimized. For its optimization the initial

values for ecutwfc and ecutrho were set to be 47 and 401, respectively, based on the maximum values of ones provided in the C, O, Pt, and H pseudopotentials.

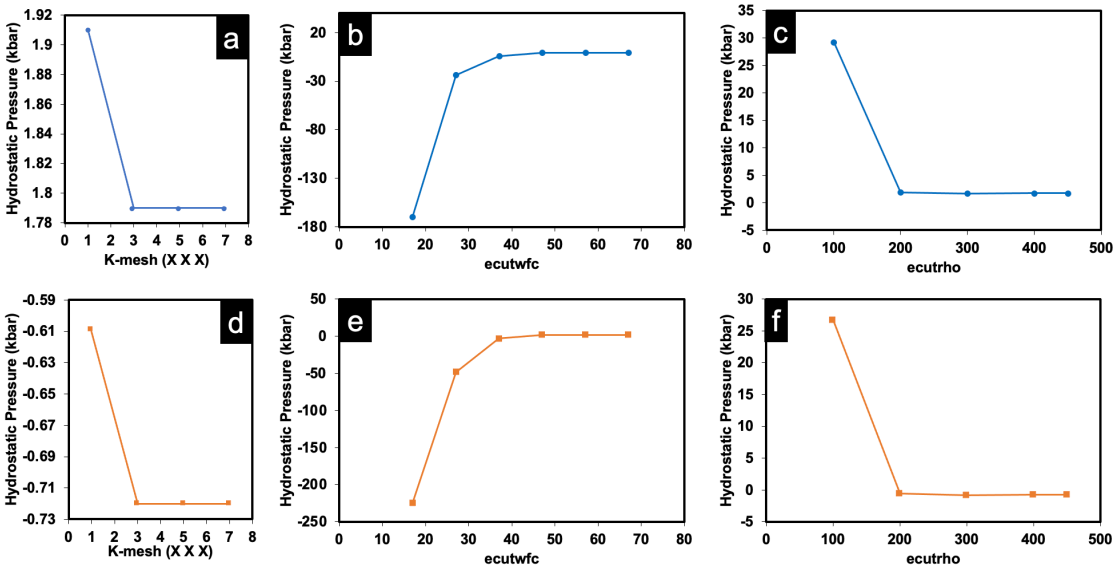

Figure 3.5: optimization of a) K-mesh, b) basis sets, and c) electron density sets for Pt/Graphene oxide, and d)K-mesh, e) basis sets, and f) electron density sets for Pt/Graphene.

As it can be seen form the figure 3.5a and d, the hydrostatic pressure is not being changed much after K sets of 3 3 3 0 0 0. So, this set size were chosen for this system. Besides, choosing higher values for the K sets needed much higher number of computational recourses. To optimize the ecutwfc and ecutrho, the K-mesh of (3 3 3) was chosen. At first, the ecutwfc were optimized with ecutrho = 9*ecutwfc for each of them. As it can be seen from the figure 3.5b and e, at ecutwfc = 50, the hydrostatic pressure value is being stabilized and does not change that much. After choosing the K-mesh of (3 3 3) and the ecutwfc = 50, the ecutrho was optimized. The figure 3.5c and f demonstrates the 6X of ecutwafc (ecutrho = 300) is a suitable value for the ecutrho.

3.3.3.4.“relax”calculation

After optimizing the necessary parameters to make sure our final properties are meaningful, to study the adsorption behavior of H_2 molecules on the proposed systems the “relax” calculation were performed. In this calculation, the system energy is converged at first, similar to the “scf” calculation. Then based on the calculated electron density around each atom, the force being applied on the atoms are calculated. After that,

the atoms (ions) which are free to move, based on those forces change, their position for specific amount and then the charge density with new atomic position will be calculated again by convergence of the energy. These steps continue until the total structure will be in equilibrium based on the equilibrium positions of the atoms. This calculation needs much more amount of time and resources to be performed. There is another type of relax calculation named “vc-relax” which means variable-cell relax calculation. The latter type of the calculation will cause the change in the dimension and shape of the cell structure which it was not needed in this study.

The input file for the “relax” calculation is similar to the SCF calculation with one extra parameter based on which the dynamic of the position of the ions (atoms) should be defied under the &IONS section:

```
&IONS
 ion_positions='defult',
 ion_dynamics='bfgs',
```

3.3.3.5.Result

At the time of writing this thesis, the “relax” calculation is still under iterations to find the final best structure for the Pt/Graphene sample. However, after every four hours the very final structure is being saved in a file that can be checked to see the current structure after relocation the atoms. The figure 3.6 is showing the last structure of the Pt/Graphene and Pt/Graphene-oxide that were saved so far (Pt/ Graphene oxide is showing the equilibrium structure after finalizing the “relax” calculation). These structures reveal some points that are worth mentioning. Note that, addition of oxygen atoms to this structure, figure 3.6b, makes the structure much more complected. It means that for same number of iterations the Pt/Graphene-oxide structure is not as at the same stage as of the Pt/Graphene structure. The following results could be seen in the dynamically changed samples.

- The first point is the wrinkling and wavy chape of the graphene planes. It is shown that the surface tension of the flat surface of graphene cause the wrinkling to decrease the energy. The oxygen functional groups caused even more disturbance of the structure, which could be the indication of the sp^2 change to sp^2 structure.
- The alignment and attachment of some portion of H_2 toward and on the Pt surface. It is even seen that the H_2 molecules which are adsorbed on the electrocatalysts is

dissociated to hydrogen atoms, which is the first step of H_2 oxidation. The final structure of Pt/Graphene-oxide does not show the adsorption of H_2 molecules. This could be the effect of oxygen atoms in the structure which could have an influence on the electronic structure of Pt particles.

- The crystal structure of the Pt particles does not remain as it was designed. It smees to change into spherical shape which might be like the TEM figure mentioned in the second chapter (figure 2.2). It is still soon to tell the final equilibrium shape of the Pt particles, but cubic structure with the plane (111) upward toward the electrolyte is not the equilibrium structure. After the finalizing the "relax" calculation, the Pt crystal might change to another orientation or remains with spherical chape, or a structure with twisted planes, similar to graphene planes.

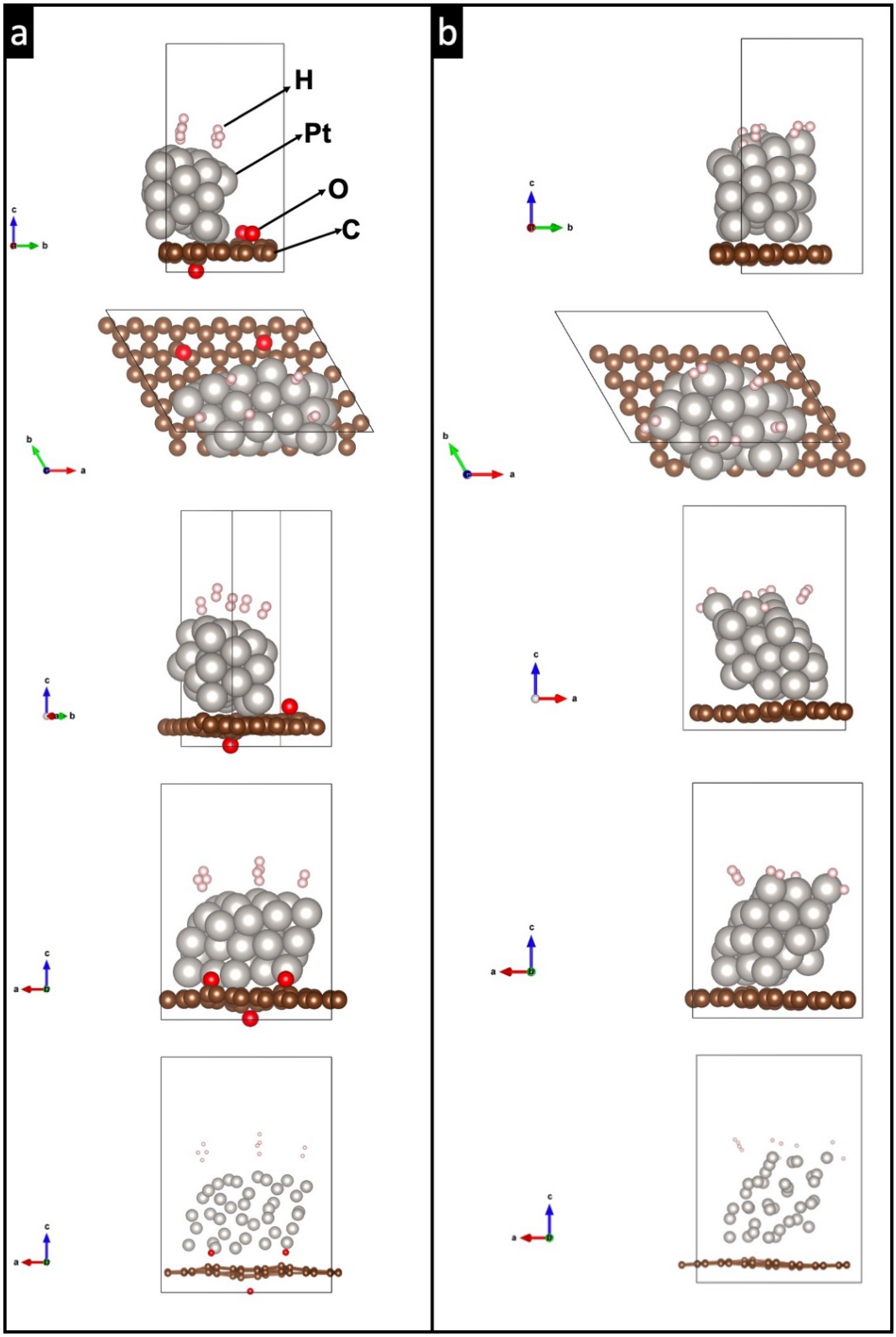

Figure 3.6. “relax”ed configuration of a) Pt/Graphene oxide and Pt/Graphene samples with five H_2 molecules on a vacuumed environment on the top, from different direction.

3.4. Conclusions

This thesis aimed to cover the electrochemical properties of photocatalytically deposited Pt/Graphene-based electrocatalysts from experimental and computational perspectives and highlight the main point to have highly active Pt-based particles in PEM fuel cells reactions. At first, two categories of parameters were studied none of which has been mentioned in the literatures. The first one was the effect of UV pulse shape on controlling the mechanism of Pt deposition on PRGO support. Based on the result, it was not only the illumination that increased the chance of obtaining an active Pt catalyst, but it was also the UV-off time which was necessary for better adsorption of Pt ions and their agglomeration on suitable spots before the reduction. The second categories of parameters in the experimental part emphasized the role of a second metallic ion in deposition of Pt particles. These ions (Co^{2+}, Ni^{2+} or Fe^{2+}) might have two major effects in the photocatalytic deposition of the main electrocatalyst, platinum. For example, Co^{2+} ions could be attracted toward negatively charged oxygen functional group and cause the deposition, stability, and agglomeration of Pt particles on specific spots. It also could change the metallic state of Pt and increase their catalytic activities. In the second part,(the 3rd chapter) included the computational approach in design Pt-based electrocatalyst. By modelling of the current densities resulted from the cyclic voltammetry oaf almost forty different samples, deposited by the pulsed-UV with photocatalytic method, with the pulse parameters as the input features of acritical neural network algorithm, this method showed its potential for precisely controlling the final properties of the electrocatalysts by adjusting the physical properties of the synthesis setup such as UV-on and -off duration. Consequently, in the second part of the computational approach utilized the Quantum-Espresso code package in modelling the H_2 adsorption and Pt stable structure on graphene-plane with and without oxygen functional group. The relaxed structure of the designed hypothetical samples after “SCF” and “relax” calculation proved that the existence of oxygen functional groups could be one of the main disadvantages of the graphene-based electrocatalysts. However, these groups might change the stable structure of deposited Pt on graphene plane. As a general summary, this study revealed different important facts about the electrocatalytic activities of the electrocatalysts deposited on graphene-based supports. Unlike the amorph structure of commercial CB which lacks

specific functional groups, graphene-based supports which are mainly produced by oxidation of graphite powders have oxygen functional groups that could deteriorated the electrocatalytic activities of Pt particles, although these functional groups play an important role in stability of Pt crystal structure. However, if suitable parameters are chosen to decrease the effect of these functional groups on the electrochemical reactions, such as the reactants adsorption of the catalysts surface, by using a second metal ion or manipulating the kinetic of catalyst particles deposition, one could benefit from the superior structural properties of graphene-based materials.

REFRENCES

[1] Tian XL, Xu YY, Zhang W, Wu T, Xia BY, Wang X. Unsupported Platinum-Based Electrocatalysts for Oxygen Reduction Reaction. ACS Energy Lett 2017;2:2035–43. https://doi.org/10.1021/acsenergylett.7b00593.

[2] Yarar Kaplan B, Haghmoradi N, Biçer E, Merino C, Alkan Gürsel S. High performance electrocatalysts supported on graphene based hybrids for polymer electrolyte membrane fuel cells. Int J Hydrogen Energy 2018;43:23221–30. https://doi.org/10.1016/j.ijhydene.2018.10.222.

[3] Marinkas A, Arena F, Mitzel J, Prinz M, Heinzel A, Peinecke V, et al. Graphene as catalyst support : The influences of carbon additives and catalyst preparation methods on the performance of PEM fuel cells 2013;8. https://doi.org/10.1016/j.carbon.2013.02.043.

[4] Işıkel Şanlı L, Bayram V, Ghobadi S, Düzen N, Alkan Gürsel S. Engineered catalyst layer design with graphene-carbon black hybrid supports for enhanced platinum utilization in PEM fuel cell. Int J Hydrogen Energy 2017;42:1085–92. https://doi.org/10.1016/j.ijhydene.2016.08.210.

[5] Wan CH, Zhuang QH. Novel layer wise anode structure with improved CO-tolerance capability for PEM fuel cell. Electrochim Acta 2007;52:4111–23. https://doi.org/10.1016/j.electacta.2006.11.045.

[6] Gasteiger HA, Kocha SS, Sompalli B, Wagner FT. Activity benchmarks and requirements for Pt, Pt-alloy, and non-Pt oxygen reduction catalysts for PEMFCs. Appl Catal B Environ 2005;56:9–35. https://doi.org/10.1016/j.apcatb.2004.06.021.

[7] Tour JM. Rice group shows graphene quantum dots beat Pt catalyst. Fuel Cells Bull 2014;2014:13. https://doi.org/10.1016/S1464-2859(14)70355-4.

[8] Do CL, Pham TS, Nguyen NP, Tran VQ. Properties of Pt/C nanoparticle catalysts synthesized by electroless deposition for proton exchange membrane fuel cell. Adv Nat Sci Nanosci Nanotechnol 2013;4:035011. https://doi.org/10.1088/2043-6262/4/3/035011.

[9] Shao Y, Yin G, Gao Y. Understanding and approaches for the durability issues of Pt-based catalysts for PEM fuel cell. J Power Sources 2007;171:558–66. https://doi.org/10.1016/j.jpowsour.2007.07.004.

[10] Sharma S, Ganguly A, Papakonstantinou P, Miao X, Li M, Hutchison JL, et al. Rapid Microwave Synthesis of CO Tolerant Reduced Graphene Oxide-Supported Platinum Electrocatalysts for Oxidation of Methanol 2010:19459–66.

[11] Wu J, Yuan XZ, Martin JJ, Wang H, Zhang J, Shen J, et al. A review of PEM fuel cell durability: Degradation mechanisms and mitigation strategies. J Power Sources 2008;184:104–19. https://doi.org/10.1016/j.jpowsour.2008.06.006.

[12] Ma J, Habrioux A, Alonso-Vante N. Enhanced HER and ORR behavior on photodeposited Pt nanoparticles onto oxide-carbon composite. J Solid State Electrochem 2013;17:1913–21. https://doi.org/10.1007/s10008-013-2046-y.

[13] Li Y, Li Y, Zhu E, Mclouth T, Chiu C, Huang X, et al. Stabilization of High-Performance Oxygen Reduction Reaction Pt Electrocatalyst Supported on Reduced Graphene Oxide/Carbon Black Composite 2012.

[14] Ma J, Habrioux A, Guignard N, Alonso-Vante N. Functionalizing effect of increasingly graphitic carbon supports on carbon-supported and TiO 2-carbon composite-supported Pt nanoparticles. J Phys Chem C 2012;116:21788–94. https://doi.org/10.1021/jp304947y.

[15] Schmittinger W, Vahidi A. A review of the main parameters influencing long-

term performance and durability of PEM fuel cells. J Power Sources 2008;180:1–14. https://doi.org/10.1016/j.jpowsour.2008.01.070.
[16] Geim AK, Novoselov KS. The rise of graphene. Nat Mater 2007:183–91. https://doi.org/http://dx.doi.org/10.1038/nmat1849.
[17] Quesnel E, Roux F, Emieux F, Faucherand P, Kymakis E, Volonakis G, et al. Graphene-based technologies for energy applications, challenges and perspectives. 2D Mater 2015;2:30204. https://doi.org/10.1088/2053-1583/2/3/030204.
[18] Srivastava SK, Pionteck J. Recent Advances in Preparation, Structure, Properties and Applications of Graphite Oxide. J Nanosci Nanotechnol 2015. https://doi.org/10.1166/jnn.2015.10047.
[19] Velasco-Soto MA, Pérez-García SA, Alvarez-Quintana J, Cao Y, Nyborg L, Licea-Jiménez L. Selective band gap manipulation of graphene oxide by its reduction with mild reagents. Carbon N Y 2015;93:967–73. https://doi.org/10.1016/J.CARBON.2015.06.013.
[20] Choi W, Lahiri I, Seelaboyina R, Kang YS, Choi W, Lahiri I, et al. Synthesis of Graphene and Its Applications : A Review Synthesis of Graphene and Its Applications : A Review 2010;8436. https://doi.org/10.1080/10408430903505036.
[21] Huang L, Huang Y, Liang J, Wan X, Chen Y. Graphene-Based Conducting Inks for Direct Inkjet Printing of Flexible Conductive Patterns and Their Applications in Electric Circuits and Chemical Sensors 2011;4. https://doi.org/10.1007/s12274-011-0123-z.
[22] Xu C, Cui A, Xu Y, Fu X. Graphene oxide – TiO 2 composite filtration membranes and their potential application for water purification. Carbon N Y 2013;62:465–71. https://doi.org/10.1016/j.carbon.2013.06.035.
[23] Hill EW, Vijayaragahvan A, Novoselov K, Exfoliation AM. Graphene Sensors 2011;11:3161–70.
[24] Shen J, Zhu Y, Yang X, Li C. ChemComm Graphene quantum dots : emergent nanolights for bioimaging , sensors , catalysis and photovoltaic devices 2012:3686–99. https://doi.org/10.1039/c2cc00110a.
[25] Chabot V, Higgins D, Yu A, Xiao X. Environmental Science material synthesis and applications to energy and 2014. https://doi.org/10.1039/c3ee43385d.
[26] Hou Y. Materials Chemistry A 2014;2. https://doi.org/10.1039/c3ta13033a.
[27] Eda BG, Chhowalla M. Chemically Derived Graphene Oxide : Towards Large-Area Thin-Film Electronics and Optoelectronics 2010:2392–415. https://doi.org/10.1002/adma.200903689.
[28] Sheath P, Majumder M. a Comparative Review of Graphene Oxide and Titanium Dioxide As Photocatalysts in Photocatalytic Systems 2010.
[29] Preparation of Graphitic Oxide 1957;208:1937. https://doi.org/10.1021/ja01539a017.
[30] Sorokina NE, Khaskov MA, Avdeev V V., Nikol'skaya I V. Reaction of graphite with sulfuric acid in the presence of KMnO4. Russ J Gen Chem 2005;75:162–8. https://doi.org/10.1007/s11176-005-0191-4.
[31] Eda G, Mattevi C, Yamaguchi H, Kim H, Chhowalla M. Insulator to Semimetal Transition in Graphene Oxide 2009;2:15768–71.
[32] Dreyer DR, Park S, Bielawski W, Ruoff RS. The chemistry of graphene oxide 2010. https://doi.org/10.1039/b917103g.
[33] Chua CK, Sofer Z, Pumera M. Graphite oxides: Effects of permanganate and chlorate oxidants on the oxygen composition. Chem - A Eur J 2012;18:13453–9.

https://doi.org/10.1002/chem.201202320.
[34] Search H, Journals C, Contact A, Iopscience M, Address IP. Tailoring the characteristics of graphite 2009;065418. https://doi.org/10.1088/0022-3727/42/6/065418.
[35] Guardia L, Paredes JI, Solı P, Tasco JMD. Vitamin C Is an Ideal Substitute for Hydrazine in the Reduction of Graphene Oxide Suspensions ´ n 2010:6426–32. https://doi.org/10.1021/jp100603h.
[36] Shen Y, Yang S, Zhou P, Sun Q, Wang P, Wan L, et al. Evolution of the band-gap and optical properties of graphene oxide with controllable reduction level. Carbon N Y 2013;62:157–64. https://doi.org/10.1016/j.carbon.2013.06.007.
[37] Shin BH, Kim KK, Benayad A, Yoon S, Park K, Jung I, et al. Efficient Reduction of Graphite Oxide by Sodium Borohydride and Its Effect on Electrical Conductance 2009:1987–92. https://doi.org/10.1002/adfm.200900167.
[38] Zhu C, Guo S, Fang Y, Dong S. Reducing Sugar : New Functional Molecules for the Green Synthesis of Graphene Nanosheets 2010;4:2429–37. https://doi.org/10.1021/nn1002387.
[39] Zhang J, Yang H, Shen G, Cheng P. Reduction of graphene oxide via L -ascorbic acid w 2010:1112–4. https://doi.org/10.1039/b917705a.
[40] Abdolhosseinzadeh S, Sadighikia S, Alkan Gürsel S. Scalable Synthesis of Sub-Nanosized Platinum-Reduced Graphene Oxide Composite by an Ultraprecise Photocatalytic Method. ACS Sustain Chem Eng 2018;6:3773–82. https://doi.org/10.1021/acssuschemeng.7b04148.
[41] Abdolhosseinzadeh S, Mousavi M, Haghmoradi N, Gürsel SA. A continuous-flow photocatalytic reactor for the precisely controlled deposition of metallic nanoparticles. J Vis Exp 2019;2019:1–8. https://doi.org/10.3791/58883.
[42] Yeh BT, Syu J, Cheng C, Chang T. Graphite Oxide as a Photocatalyst for Hydrogen Production from Water 2010:2255–62. https://doi.org/10.1002/adfm.201000274.
[43] Kamat P V. Graphene-based nanoarchitectures. Anchoring semiconductor and metal nanoparticles on a two-dimensional carbon support. J Phys Chem Lett 2010;1:520–7. https://doi.org/10.1021/jz900265j.
[44] Thanh NTK, Maclean N, Mahiddine S. Mechanisms of nucleation and growth of nanoparticles in solution. Chem Rev 2014;114:7610–30. https://doi.org/10.1021/cr400544s.
[45] Kwon SG, Hyeon T. Formation Mechanisms of Uniform Nanocrystals via Hot-Injection and Heat-Up Methods 2011:2685–702. https://doi.org/10.1002/smll.201002022.
[46] Kraeutler B, Bard AJ. Heterogeneous photocatalytic preparation of supported catalysts. Photodeposition of platinum on titanium dioxide powder and other substrates. J Am Chem Soc 1978;100:4317–8. https://doi.org/10.1021/ja00481a059.
[47] Wenderich K, Han K, Mul G. The Effect of Methanol on the Photodeposition of Pt Nanoparticles on Tungsten Oxide. Part Part Syst Charact 2018;35:1–8. https://doi.org/10.1002/ppsc.201700250.
[48] Hinogami R, Nakamura Y, Yae S, Nakato Y. Modification of semiconductor surface with ultrafine metal particles for efficient photoelectrochemical reduction of carbon dioxide. Appl Surf Sci 1997;121–122:301–4. https://doi.org/10.1016/S0169-4332(97)00310-3.
[49] Lim SK, Lee SK, Hwang SH, Kim H. Photocatalytic deposition of silver nanoparticles onto organic/inorganic composite nanofibers. Macromol Mater Eng

2006;291:1265–70. https://doi.org/10.1002/mame.200600264.
[50] Albiter E, Valenzuela MA, Alfaro S, Valverde-Aguilar G, Martínez-Pallares FM. Photocatalytic deposition of Ag nanoparticles on TiO<inf>2</inf>: Metal precursor effect on the structural and photoactivity properties. J Saudi Chem Soc 2015;19:563–73. https://doi.org/10.1016/j.jscs.2015.05.009.
[51] Sun B, Vorontsov A V, Smirniotis PG. Role of Platinum Deposited on TiO in Phenol Photocatalytic Oxidation Role of Platinum Deposited on TiO 2 in Phenol Photocatalytic Oxidation. Society 2003;19:3151–6. https://doi.org/10.1021/la0264670.
[52] Sliem M a, Hikov T, Li Z-A, Spasova M, Farle M, Schmidt D a, et al. Interfacial Cu/ZnO contact by selective photodeposition of copper onto the surface of small ZnO nanoparticles in non-aqueous colloidal solution. Phys Chem Chem Phys 2010;12:9858–66. https://doi.org/10.1039/c003861j.
[53] Wang M, Chen L, Sun L. Recent progress in electrochemical hydrogen production with earth-abundant metal complexes as catalysts. Energy Environ Sci 2012;5:6763–78. https://doi.org/10.1039/c2ee03309g.
[54] Marschall R. Semiconductor composites: Strategies for enhancing charge carrier separation to improve photocatalytic activity. Adv Funct Mater 2014;24:2421–40. https://doi.org/10.1002/adfm.201303214.
[55] Sharma JC, Gandhi J, Sharma A. PHOTOCATALYTIC REDUCTION OF SILVER (I) TO METALLIC SILVER OVER SrWO 4 2008;6:509–18.
[56] Hiera T, Mari MAI, Mammut WA, Shell IC, Ci US. Thai hiera mai mari wa mammut mark 2018;2.
[57] McDonald KJ, Choi KS. Photodeposition of co-based oxygen evolution catalysts on α-Fe 2O3 photoanodes. Chem Mater 2011;23:1686–93. https://doi.org/10.1021/cm1020614.
[58] Sajan CP, Wageh S, Al-Ghamdi AA, Yu J, Cao S. TiO2 nanosheets with exposed {001} facets for photocatalytic applications. Nano Res 2016;9:3–27. https://doi.org/10.1007/s12274-015-0919-3.
[59] Ros C, Andreu T, Morante JR. Photoelectrochemical water splitting: a road from stable metal oxides to protected thin film solar cells. J Mater Chem A 2020;8:10625–69. https://doi.org/10.1039/d0ta02755c.
[60] Tolle HJ, Memming R. On the Origin of the Photocatalytic Deposition of Noble Metals on Ti02 2015.
[61] Foster NS, Lancaster a N, Noble RD, Koval C a. Effect of organics on the photodeposition of copper in titanium dioxide aqueous suspensions. Ind Eng Chem Res 1995;34:3865–71. https://doi.org/10.1021/ie00038a025.
[62] Wenderich K, Mul G. Methods, Mechanism, and Applications of Photodeposition in Photocatalysis: A Review. Chem Rev 2016;116:14587–619. https://doi.org/10.1021/acs.chemrev.6b00327.
[63] Chanjuan Xi, Zhengshi Chen, Qinglin Li, Zhensheng Jin. Effects of H+, Cl- and CH3COOH on the photocatalytic conversion of PtCl62- in aqueous TiO2 dispersion. J Photochem Photobiol A Chem 1995;87:249–55. https://doi.org/10.1016/1010-6030(94)03983-2.
[64] Xiong Z, Zhang L, Ma J, Zhao XS. Photocatalytic degradation of dyes over graphene – gold nanocomposites under visible light irradiation w 2010:6099–101. https://doi.org/10.1039/c0cc01259a.
[65] Oxide G, Xiong Z, Zhang LL, Song X. Visible-Light-Induced Dye Degradation over Copper-Modified Reduced 2011:2428–34. https://doi.org/10.1002/chem.201002906.

[66] Abdolhosseinzadeh S, Sadighikia S, Alkan Gürsel S. Scalable synthesis of sub-nanosized platinum-reduced graphene oxide composite by an ultraprecise photocatalytic method. ACS Sustain Chem Eng 2018;6:3773–82.
[67] Google Developers. Machine Learning Crash Course n.d. https://developers.google.com/machine-learning/crash-course.
[68] Giustino F. Materials Modelling using Density Functional Theory. 1st ed. Oxford University Press; 2014.
[69] Ghosh A, Subrahmanyam KS, Krishna KS, Datta S, Govindaraj A, Pati SK, et al. Uptake of H 2 and CO 2 by Graphene 2008:15704–7. https://doi.org/10.1021/jp805802w.
[70] Kim S, Choi SK, Lim SK, Chang D, Park H. Pt immobilization on TiO2-embedded carbon nanofibers using photodeposition. Cryst Res Technol 2010;45:1079–82. https://doi.org/10.1002/crat.201000271.
[71] The Mathworks. MATLAB_R2021a 2021.
[72] Giannozzi P, Baroni S, Bonini N, Calandra M, Car R, Cavazzoni C, et al. QUANTUM ESPRESSO: a modular and open-source software project for quantum simulations of materials. J Phys Condens Matter 2009;21:395502. https://doi.org/10.1088/0953-8984/21/39/395502.
[73] Giannozzi P, Baseggio O, Bonfà P, Brunato D, Car R, Carnimeo I, et al. Quantum ESPRESSO toward the exascale. J Chem Phys 2020;152:154105. https://doi.org/10.1063/5.0005082.
[74] Mizukoshi Y, Takagi E, Okuno H, Oshima R, Maeda Y, Nagata Y. Preparation of platinum nanoparticles by sonochemical reduction of the Pt(IV) ions: role of surfactants. Ultrason Sonochem 2001;8:1–6. https://doi.org/https://doi.org/10.1016/S1350-4177(00)00027-4.
[75] Ferrari AC, Robertson J. Interpretation of Raman spectra of disordered and amorphous carbon. Phys Rev B 2000;61:14095.
[76] Pourbaix, M. J. N., J. Van Muylder and NDZ. Electrochemical Properties of the Platinum Metals. Platin Met Rev 1959;3:47–53.
[77] Albiter E, Valenzuela MA, Alfaro S, Valverde-Aguilar G, Martínez-Pallares FM. Photocatalytic deposition of Ag nanoparticles on TiO2: Metal precursor effect on the structural and photoactivity properties. J Saudi Chem Soc 2015;19:563–73.
[78] Kim HJ, Ruqia B, Kang MS, Lim S Bin, Choi R, Nam KM, et al. Shape-controlled Pt nanocubes directly grown on carbon supports and their electrocatalytic activity toward methanol oxidation. Sci Bull 2017;62:943–9.
[79] Yarar Kaplan B, Haghmoradi N, Jamil E, Merino C, Alkan Gürsel S. Platinum nanoparticles decorated carbon nanofiber hybrids as highly active electrocatalysts for polymer electrolyte membrane fuel cells. Int J Energy Res 2020;44:10251–61.
[80] Yarar Kaplan B, Haghmoradi N, Biçer E, Merino C, Alkan Gürsel S. High performance electrocatalysts supported on graphene based hybrids for polymer electrolyte membrane fuel cells. Int J Hydrogen Energy 2018;43:23221–30. https://doi.org/https://doi.org/10.1016/j.ijhydene.2018.10.222.
[81] Chandrasekaran S, Ma D, Ge Y, Deng L, Bowen C, Roscow J, et al. Electronic structure engineering on two-dimensional (2D) electrocatalytic materials for oxygen reduction, oxygen evolution, and hydrogen evolution reactions. Nano Energy 2020;77:105080. https://doi.org/https://doi.org/10.1016/j.nanoen.2020.105080.

Appendix

Quantum Espresso input files

For running the Quantum-Espresso (QE) code for any types of DFT calculations (SCF, relax, etc.) the basis set size and the k-mesh should be determined, otherwise the calculation will end up in some meaningless numbers yet without error. The term for basis set size is kinetic energy cutoff and the k-mesh is k-points set.

Three important keywords in QE Input files

QE input file has different sections like the following:

```
#*******************************************************************************
#*                    Generated by cif2cell 2.0.0 2020-11-14 23:40             *
#*  T. Bjorkman, Comp. Phys. Commun. 182, 1183-1186 (2011). Please cite generously. *
#*                                                                             *
#*                                    None   ()                                *
#*                Wyckoff, R. W. G., Crystal Structures 1, 7-83 (1963)         *
#*******************************************************************************
&CONTROL
 calculation='scf',
 outdir='.',
 prefix='basic',
 pseudo_dir='.',
 verbosity='low',
 tprnfor=.true.,
 tstress=.true.,
/
&SYSTEM
  ibrav = 0
  A =    5.43070
  nat = 2
  ntyp = 1
  ecutwfc=50,
  ecutrho=200,
  input_dft='pbe',
  occupations='smearing',
  smearing='mv',
  degauss=0.005d0,
/
&ELECTRONS
 conv_thr=1d-08,
 mixing_beta=0.7d0,
/
CELL_PARAMETERS {alat}
  0.500000000000000   0.500000000000000   0.000000000000000
  0.500000000000000   0.000000000000000   0.500000000000000
  0.000000000000000   0.500000000000000   0.500000000000000
ATOMIC_SPECIES
  Si   28.08500  Si.pbe-n-kjpaw_psl.1.0.0.UPF
ATOMIC_POSITIONS {crystal}
Si   0.000000000000000   0.000000000000000   0.000000000000000
Si   0.250000000000000   0.250000000000000   0.250000000000000
K_POINTS {automatic}
 7 7 7 0 0 0
```

The kind of the XC-functionality is a crucial keyword that should be declared for your input file. in the last box above, under the &SYSTEM section the term: input_dft='LDA', or

input_dft='pba',

is the location where you select the XC-functional. The pseudopotential file should be acquired from the QE website based on the type of XC-functional you desire. The type of XC-functional in the stated line is automatically updated when you choose the pseudopotential file. So, while the line above is not required, the kind of pseudopotential must be determined. For example, the pseudopotential file for Si atoms is selected under the line ATOMIC SPECIES..

The k-mesh is the second significant term (reciprocal lattice mesh). In DFT, we can get a lot of information by integrating across the first Brillouin zone (The lattice cell in reciprocal space). The code employs a numerical summation approach for integration. As a result, the mesh size and sample sites must be determined. In reciprocal space, k-mesh is expressed as a three-dimensional grid. We can find, for example, the following in the input file's &ELECTRON section:

Use the 3x3x3 mesh setting to create a 3x3x3 mesh.:

K_POINTS {automatic}

3 3 3 0 0 0

To use a 5x5x5 mesh, use

K_POINTS {automatic}

5 5 5 0 0 0

The basis set size is the third most essential term in the input file. Basis sets are utilized to model the Kohn-Sham orbitals, as previously stated. (ϕ). It's the equivalent of writing a periodic function in infinite cosine functions. The KS orbitals, however, cannot be expressed using infinite basis sets. We must utilize the maximum number; if we use a number higher than that, we will not gain much more precision and the computation time will be reduced. We may notice, for example, in the input file beneath the &SYSTEM block:

ecutwfc=30.0d0,
This illustrates the wave function's basis set size.

Another basis set size is used to characterize the density, which is: ecutrho

It is 4x of ecutwfc by default, but if we use PAW pseudopotential, it should be greater, or much bigger (8x to 12x) for ultrasoft pseudopotential..

One might execute the input file after introducing the last three keywords that must be defined in the input file. Assume that the input file for a new structure has all of the parameters, atom locations, pseudopotentials, and so on. To ensure that your future data is relevant, you must first do a convergence test. Download the.CIF file, crystallographic data file (for example, 9008678.cif for NaCl crystal) from the crystallographic database and convert the format to one that QE can read after creating an appropriate directory and folders to keep your files. To convert this file to an.in file, use the following command line.:

cif2cell 9008678.cif -p quantum-espresso -o halite.in

(Note: These commands should be written in Terminal and in the created folder)
The file looks like:

```
#*********************************************************************************
#*                    Generated by cif2cell 2.0.0 2020-12-08 19:12               *
#*  T. Bjorkman, Comp. Phys. Commun. 182, 1183-1186 (2011). Please cite generously. *
#*                                                                               *
#*                                 None   (Halite)                               *
#*             Wyckoff, R. W. G., Crystal Structures 1, 85-237 (1963)            *
#*********************************************************************************

&SYSTEM
  ibrav = 0
  A =    5.64056
  nat = 2
  ntyp = 2
/
CELL_PARAMETERS {alat}
  0.500000000000000   0.500000000000000   0.000000000000000
  0.500000000000000   0.000000000000000   0.500000000000000
  0.000000000000000   0.500000000000000   0.500000000000000
ATOMIC_SPECIES
  Cl   35.45150  Cl_PSEUDO
  Na   22.98900  Na_PSEUDO
ATOMIC_POSITIONS {crystal}
Cl   0.500000000000000   0.500000000000000   0.500000000000000
Na   0.000000000000000   0.000000000000000   0.000000000000000
```

Then, from the QE website, get the Cl and Na pseudopotential files (our example here is NaCl salt).

Na.pbe-spn-kjpaw_psl.1.0.0.UPF

Cl.pbe-n-kjpaw_psl.1.0.0.UPF

We will add other parts to the input file to become:

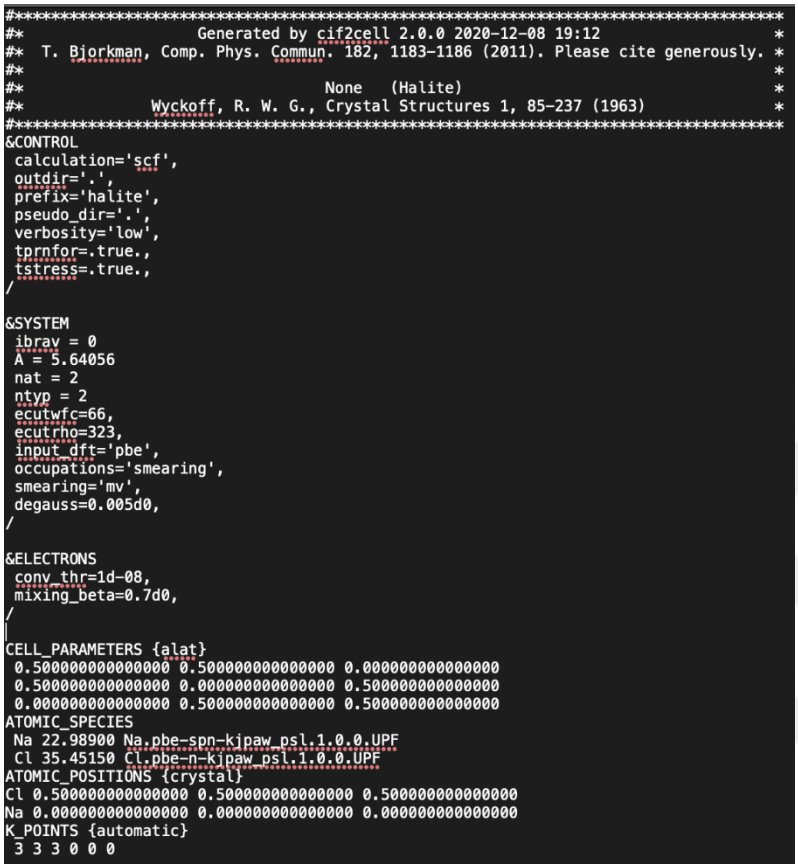

```
#*******************************************************************************
#*                  Generated by cif2cell 2.0.0 2020-12-08 19:12               *
#*  T. Bjorkman, Comp. Phys. Commun. 182, 1183-1186 (2011). Please cite generously. *
#*                                                                             *
#*                                 None   (Halite)                             *
#*             Wyckoff, R. W. G., Crystal Structures 1, 85-237 (1963)          *
#*******************************************************************************
&CONTROL
 calculation='scf',
 outdir='.',
 prefix='halite',
 pseudo_dir='.',
 verbosity='low',
 tprnfor=.true.,
 tstress=.true.,
/

&SYSTEM
 ibrav = 0
 A = 5.64056
 nat = 2
 ntyp = 2
 ecutwfc=66,
 ecutrho=323,
 input_dft='pbe',
 occupations='smearing',
 smearing='mv',
 degauss=0.005d0,
/

&ELECTRONS
 conv_thr=1d-08,
 mixing_beta=0.7d0,
/
CELL_PARAMETERS {alat}
 0.500000000000000 0.500000000000000 0.000000000000000
 0.500000000000000 0.000000000000000 0.500000000000000
 0.000000000000000 0.500000000000000 0.500000000000000
ATOMIC_SPECIES
 Na 22.98900 Na.pbe-spn-kjpaw_psl.1.0.0.UPF
 Cl 35.45150 Cl.pbe-n-kjpaw_psl.1.0.0.UPF
ATOMIC_POSITIONS {crystal}
Cl 0.500000000000000 0.500000000000000 0.500000000000000
Na 0.000000000000000 0.000000000000000 0.000000000000000
K_POINTS {automatic}
 3 3 3 0 0 0
```

As we can see the line:

input_dft='pbe',
indicates the exchange correlation potential's kind. It's also worth noting that pseudopotentials are based on this XC potential. The pseudopotential file is also used to determine the size of the basis set. We may view the lines for Na and Cl atoms in their respective files if we open the pseudopotential files in a text editing program."

Na-file:
Suggested minimum cutoff for wavefunctions: 66. R

Suggested minimum cutoff for charge density: 323. Ry

Cl-file:
Suggested minimum cutoff for wavefunctions: 45.

Ry Suggested minimum cutoff for charge density: 223. Ry

So, if we take 66 and 323 for wavefunction and charge density, respectively, (maximum of numbers) we are probably on the safe side.

Practical example

For k-mesh choose:

- As previously stated, it is a sample number in 3D reciprocal space.
- It is located in the &ELECTRONS block.
- The default mesh size is 1x1x1, however we may modify it..

The characteristics do not change much as the k-mesh is increased after some SCF runs. This K-mesh could be necessary for the computation. We may do this by creating a table or graph and determining the horizontal line for those properties..

If the value for the hydrostatic pressure is found in the output file, it is the best characteristic of the system, as it is more sensitive to the k-mesh and other important parameter values. In other words, assuming hydrostatic pressure remains constant as the number of parameters increases, additional characteristics may be estimated using the key parameter's optimal values.

As described above, the input file should look like this to run and examine the effect of K-mesh on the hydrostatic pressure:

```
&CONTROL
calculation='scf',
outdir='.',
prefix='halite',
pseudo_dir='.',
verbosity='low',
tprnfor=.true.,
tstress=.true.,

/&SYSTEM
ibrav = 0
A = 5.64056
nat = 2
ntyp = 2
ecutwfc=66,
ecutrho=323,
```

```
input_dft='pbe',
occupations='smearing',
smearing='mv',
degauss=0.005d0,
/&ELECTRONS

conv_thr=1d-08,
mixing_beta=0.7d0,
/CELL_PARAMETERS {alat}
0.500000000000000 0.500000000000000 0.000000000000000
0.500000000000000 0.000000000000000 0.500000000000000
0.000000000000000 0.500000000000000 0.500000000000000

ATOMIC_SPECIES
Na 22.98900 Na.pbe-spn-kjpaw_psl.1.0.0.UPF
Cl 35.45150 Cl.pbe-n-kjpaw_psl.1.0.0.UPF

ATOMIC_POSITIONS {crystal}
Cl 0.500000000000000 0.500000000000000 0.500000000000000
Na 0.000000000000000 0.000000000000000 0.000000000000000

K_POINTS {automatic}
1 1 1 0 0 0
```

- Write this command line in the terminal in the folder holding the input file.:
  pw.x -input basic.in > basic.out
- In the output file the:
  total stress (Ry/bohr^3) (kbar) P= 243.68
- K-mesh = 3 3 3 0 0 0:
  total stress (Ry/bohr**3) (kbar) P= 3.15
- K-mesh = 5 5 5 0 0 0:
  total stress (Ry/bohr^3) (kbar) P= 1.24
- K-mesh = 7 7 7 0 0 0:
  total stress (Ry/bohr**3) (kbar) P= 1.10
- K-mesh = 9 9 9 0 0 0:
  total stress (Ry/bohr**3) (kbar) P= 1.11

Around K-mesh of 7 7 7 0 0 0, the hydrostatic pressure remained constant. From now on, we'll stick to it..

2. For choosing the basis-set size:

With ecutwfc=66 and ecutrho=323, and a multiplication factor of 5, we offered ecutwfc=66 and ecutrho=323. We will optimize the ecutwfc first, and then the multiplication factor with the chosen ecutwfc to optimize ecutrho..

- ecutwfc=16, ecutrho=80, total stress (Ry/bohr^3) (kbar) P= -5324.52
- ecutwfc=26, ecutrho=130, total stress (Ry/bohr^3) (kbar) P= -865.62
- ecutwfc=36, ecutrho=180, total stress (Ry/bohr^3) (kbar) P= -268.15
- ecutwfc=46, ecutrho=230, total stress (Ry/bohr^3) (kbar) P= -8.99
- ecutwfc=56, ecutrho=280, total stress (Ry/bohr^3) (kbar) P= 4.34
- ecutwfc=66, ecutrho=330, total stress (Ry/bohr^3) (kbar) P= 0.95
- ecutwfc=76, ecutrho=380, total stress (Ry/bohr^3) (kbar) P= 4.56
- ecutwfc=86, ecutrho=430, total stress (Ry/bohr^3) (kbar) P= 7.11
- ecutwfc=96, ecutrho=480, total stress (Ry/bohr^3) (kbar) P= 7.85
- ...
- ecutwfc=200, ecutrho=1000, total stress (Ry/bohr**3) (kbar) P= 8.3

P values fluctuate until ecutwfc=66, resulting in P = 0.95, which is not far off from P = 8.3. ecutwfc's initial values should be compared. It's now time to improve ecutrho. We've been using the factor of 5 to discover it so far. However, it must be optimized:

- X 2 and ecutrho = 180 and P = 9.13
- X 3 and ecutrho = 270 and P = 7.9
- X 4 and ecutrho = 360 and P = 7.45
- X 5 and ecutrho = 450 and P = 7.59
- X 6 and ecutrho = 540 and P = 7.72
- X 7 and ecutrho = 630 and P = 7.51
- X 8 and ecutrho = 720 and P = ...
- X 9 and ecutrho = 810 and P = ...
- X 10 and ecutrho = 900 and P = 7.63

Numbers fall within a specified range after being multiplied by four. To be safe, a factor of 5 might be used.